QUANTUM COLLECTIVE DYNAMICS FROM THE neV TO THE GeV

by

Steven Kurt Steinke

A Dissertation Submitted to the Faculty of the

DEPARTMENT OF PHYSICS

In Partial Fulfillment of the Requirements
For the Degree of

DOCTOR OF PHILOSOPHY

In the Graduate College

THE UNIVERSITY OF ARIZONA

2011

THE UNIVERSITY OF ARIZONA
GRADUATE COLLEGE

As members of the Dissertation Committee, we certify that we have read the dissertation prepared by Steven Kurt Steinke
entitled Quantum Collective Dynamics From the neV To the GeV
and recommend that it be accepted as fulfilling the dissertation requirement for the Degree of Doctor of Philosophy.

Date: 21 April 2011
Pierre Meystre

Date: 21 April 2011
Johann Rafelski

Date: 21 April 2011
Ubirajara van Kolck

Date: 21 April 2011
Ewan Wright

Final approval and acceptance of this dissertation is contingent upon the candidate's submission of the final copies of the dissertation to the Graduate College.
I hereby certify that I have read this dissertation prepared under my direction and recommend that it be accepted as fulfilling the dissertation requirement.

Date: 21 April 2011
Dissertation Director: Pierre Meystre

STATEMENT BY AUTHOR

This dissertation has been submitted in partial fulfillment of requirements for an advanced degree at the University of Arizona and is deposited in the University Library to be made available to borrowers under rules of the Library.

Brief quotations from this dissertation are allowable without special permission, provided that accurate acknowledgment of source is made. Requests for permission for extended quotation from or reproduction of this manuscript in whole or in part may be granted by the head of the major department or the Dean of the Graduate College when in his or her judgment the proposed use of the material is in the interests of scholarship. In all other instances, however, permission must be obtained from the author.

SIGNED: Steven Kurt Steinke

ACKNOWLEDGEMENTS

There are an infinite (countable, but still infinite) number of people without whose support this document, and hence my degree, would not exist. Therefore, it is mathematically impossible to thank them all, particularly with a one-page limit, but here goes.

Thank you, Pierre Meystre, for the opportunity to work in a great group. Thanks as well to my collaborators past and present, Lukas Buchmann, Wenzhou Chen, Aravind Chiruvelli, Dan Goldbaum, Hui Jing, Rina Kanamoto, Greg Phelps, Keith Schwab, Mehmet Tasgin, Mukund Vengalatorre, and Lin Zhang, for providing a stimulating environment to do physics. And an extra special thank you to my office mates HyoJun Seok and Swati Singh for your support and particularly for not calling the authorities as I gradually went crazy writing this disseratation.

I would also like to thank my past advisor Johann Rafelski for continued guidance and assistance throughout the years. Thanks as well to my old collaborators and friends from my nuclear theory life, Wojciech Broniowski, Mikolaj Chojnacki, Wojciech Florkowski, Inga Kuznetsova, Jean Letessier, and Giorgio Torrieri, for teaching me QCD so well I still dream of parton distribution functions.

Of course, as the hundreds of ridiculous questions archived in my sent email folder, and the thousands of patient responses saved in my inbox prove, I would have never gotten here without the help of great advising and support staff, particularly Mike Eklund, Phil Goisman, Eva Gonzales, Roger Haar, Larry Hoffman, Linda Passarelli, Lisa Shapouri, Soraya Torabi, Koen Visscher, and Patty Zeigler.

In addition, thanks to Bira van Kolck, for being a great teacher who has the very bad habit of seemingly only teaching early in the morning, and thanks to Ewan Wright for being a scientist so prolific the rest of us are measured in millihims. Also thank you both very much for taking the time out of your schedules to be on this committee.

Lastly, I am very grateful to the many groups that have generously provided financial support for my work, in particular the National Science Foundation, the Army Research Office, the Office of Naval Research, the Defense Advanced Research Projects Agency, and the Department of Energy.

DEDICATION

For Maureen Maher Steinke, whose birthday I missed to write this dissertation.

And also for you – thanks for reading.

TABLE OF CONTENTS

TABLE OF CONTENTS – *Continued*

LIST OF FIGURES

LIST OF FIGURES – *Continued*

LIST OF FIGURES – *Continued*

LIST OF FIGURES – *Continued*

ABSTRACT

Three problems are investigated in the context of quantum collective dynamics. First, we examine the optomechanics of a Bose-Einstein condensate trapped in an optical ring cavity and coupled to counter-propagating light fields. Virtual dipole transitions cause the light to recoil elastically from the condensate and to excite its atoms into momentum side modes. These momentum side modes produce collective density oscillations. We contrast the situation to a condensate trapped in a Fabry-Pérot cavity, where only symmetric ("cosine") side modes are excited. In the ring cavity case, antisymmetric ("sine") modes can be excited also. We explore the mean field limit and find that even when the counter-propagating light fields are symmetrically pumped, there are parameter regions where spontaneous symmetry breaking occurs and the sine mode becomes occupied. In addition, quantum fluctuations are taken into account and shown to be particularly significant for parameter values near bifurcations of the mean field dynamics.

The next system studied is a hybrid composed of a high quality micromechanical membrane coupled magnetically to a spinor condensate. This coupling entangles the membrane and the condensate and can produce position superposition states of the membrane. Successive spin measurements of the condensate can put the membrane into an increasingly complicated state. It is possible in principle to produce nonclassical states of the membrane. We also examine a model of weaker, nonprojective measurements of the condensate's spin using phase contrast imaging. We find an upper limit on how quickly such measurements can be made without severely disrupting the unitary dynamics.

The third situation analyzed is the string breaking mechanism in ultrahigh energy collisions. When quark-antiquark pairs are produced in a collision, they are believed to be linked by a tube of chromoelectric field flux, the color string. The

energy of the string grows linearly with quark separation. This energy is converted into real particles by the Schwinger mechanism. Screening of the color fields by new particles breaks the string. By quantizing excitations of the string using the conjugate coordinates of field strength and string cross-section, we recover the observed exponential spectrum of outgoing particles.

CHAPTER 1

INTRODUCTION

Non-relativistic quantum mechanics is traditionally viewed as a theory that describes the behavior of individual fundamental particles [1]. Whether in the Schrödinger [2] or Heisenberg [3] picture, the laws of quantum mechanics determine the unitary evolution of the quantum state or quantum operators, respectively, of a particle such as an electron contained in an external potential. Yet this view has a few shortcomings. For one thing, particles such as atomic nuclei are composed of nucleons, giving them a complicated internal structure space [4]. Even an electron is not absolutely guaranteed, at our present level of understanding, to be a truly fundamental particle [5]. Yet, despite these facts, to understand how a nuclear spin precesses in a magnetic field or how an electron moves in an external field one can write down the Hamiltonian of the system while ignoring the (actual or hypothetical) internal structure of the object(s) being studied and still acheive results of remarkable accuracy [6]. Furthermore, in fields of study such as solid state physics, one often speaks of **collective** excitations of the material and treats these excitations as if they were independent quasiparticles (e.g. phonons, polarons, plasmons, polaritons, excitons, magnons, rotons, etc. [7]). To see how the collective motion of a composite quantum mechanical system may itself be quantized and analyzed independently, and also because such a variety of systems will be studied in this work, we turn first to a simple but very general example.

1.1 Collective motion of center of mass

Consider a system of N distinguishable particles, each with negligible internal dynamics, moving in D spatial dimensions. Let particle n have mass m_n and position and momentum operators $x_{n,i}$ and $p_{n,i}$, respectively, where the first index will indicate the particle number and the second the spatial component. These operators obey commutation relations

$$[x_{l,i}, p_{n,j}] = \mathrm{i}\hbar\delta_{ln}\delta_{ij}, \tag{1.1}$$

where δ is the Kronecker delta. Define new center of mass operators

$$\vec{X} = \frac{1}{M}\sum_{n=1}^{N} m_n \vec{x}_n, \tag{1.2}$$

$$\vec{P} = \sum_{n=1}^{N} \vec{p}_n, \tag{1.3}$$

where

$$M = \sum_{n=1}^{N} m_n \tag{1.4}$$

is the total mass of the system. We note that when dealing with indistinguishable quantum particles, such as (fermions) bosons, the individual position and momentum operators are not even truly well defined, since they will not map an (anti)symmetrized state onto another (anti)symmetrized state. Thus, we have little choice in that case but to speak of the collective motion and to augment the description of the dynamics with other appropriately (anti)symmetrized operators as needed.

Next, we compute the commutator of $\vec{X}$ with $\vec{P}$:

$$\begin{aligned}
[X_i, P_j] &= \frac{1}{M}\sum_{l=1}^{N}\sum_{n=1}^{N} m_l \left[x_{l,i}, p_{n,j}\right] \\
&= \frac{1}{M}\sum_{l=1}^{N}\sum_{n=1}^{N} \mathrm{i}\hbar m_l \delta_{ln}\delta_{ij} \\
&= \mathrm{i}\hbar\delta_{ij}. \qquad (1.5)
\end{aligned}$$

The center of mass operators operators $\vec{X}$ and $\vec{P}$ thus have the same commutator as the position and momentum operators of an elementary particle of mass M. We consider now a Hamiltonian

$$H = \sum_{n=1}^{N}\frac{\vec{p}_n^{\,2}}{2m_n} + \sum_{n=1}^{N} V_{n,\mathrm{ext}}\left(\vec{x}_n\right) + \sum_{n<l} V_{n,l,\mathrm{int}}\left(\vec{x}_n - \vec{x}_l\right), \qquad (1.6)$$

where the the subscripts "ext" and "int" indicate interactions with an external potential and internal interactions between particles (assumed here to be 2-body in nature and dependent only on their relative positions). These need not be the same potentials for all particles. Inspired by the analogous situation in classical mechanics [8], we define difference coordinates,

$$\begin{aligned}
\vec{x}'_n &= \vec{x}_n - \vec{X}, \\
\vec{p}'_n &= \vec{p}_n - \frac{m_n}{M}\vec{P}. \qquad (1.7)
\end{aligned}$$

$\vec{x}'_n$ and $\vec{p}'_n$ all commute with $\vec{X}$ and $\vec{P}$ but, because they are constrained by

$$\sum_{n=1}^{N} m_n \vec{x}'_n = \sum_{n=1}^{N} \vec{p}'_n = 0, \qquad (1.8)$$

they do not exactly commute with each other:

$$\left[x'_{l,i}, p'_{n,j}\right] = \mathrm{i}\hbar\left(\delta_{ln} - \frac{m_n}{M}\right)\delta_{ij}. \qquad (1.9)$$

By Taylor expansion, we now can rewrite the Hamiltonian in terms of center of mass and difference coordinates:

$$\begin{aligned} H &= \frac{\vec{P}^2}{2M} + \sum_{n=1}^{N} V_{n,\text{ext}}\left(\vec{X}\right) \\ &+ \sum_{n=1}^{N}\left(\frac{\vec{p'}_n^{\,2}}{2m_n} + \vec{\nabla}V_{n,\text{ext}}\left(\vec{X}\right)\cdot\vec{x}'_n + \mathcal{O}\left(\vec{x'}_n^{\,2}\right) + \sum_{l=n+1}^{N} V_{n,l,\text{int}}\left(\vec{x}'_n - \vec{x}'_l\right)\right) \end{aligned} \quad (1.10)$$

If the external potential is proportional to mass (or if the particles are identical), the term proportional to $\vec{\nabla}V_{\text{ext}}$ vanishes. In this case, in the Heisenberg picture, the equations of motion for the center of mass coordinates are:

$$\begin{aligned} \dot{\vec{X}} &= \frac{\vec{P}}{M}, \\ \dot{\vec{P}} &= -M\vec{\nabla}U\left(\vec{X}\right) + \mathcal{O}\left(\vec{x'}_n^{\,2}\right), \end{aligned} \quad (1.11)$$

where $U = V_{n,\text{ext}}/m_n$. The second order corrections will be neglible if $\epsilon \ll 1$, where

$$\epsilon = \frac{\left|\left\langle\vec{\nabla}\left(\sum_{n=1}^{N}\sum_{i=1}^{D}\sum_{j=1}^{D} x'_{n,i}x'_{n,j}\partial_i\partial_j V_{n,\text{ext}}\left(\vec{X}\right)\right)\right\rangle\right|}{2\left|\left\langle M\vec{\nabla}U\left(\vec{X}\right)\right\rangle\right|}. \quad (1.12)$$

In essence, this condition requires that the external force not fluctuate much when compared to its mean value at the center of mass on the typical length scales of the $\vec{x}'_n$'s. This is a perfectly reasonable assumption when considering a macroscopic field applied to a microscopic collection of particles, as long as the particles have either sufficiently strong interactions or low enough relative velocities to keep them from drifting apart during the time scale of interest.

Therefore, up to small corrections due to higher moments of the particle distribution, we can treat the center of mass motion as independent from the system's internal dynamics. We note that we can often include the effects of the higher order terms as damping and dissipation effects. This phenomenological treatment is necessary as we usually cannot in practice monitor the detailed internal motion of the constituent particles.

The simple example outlined above will inspire the approach used on three diverse problems. In Appendix A, we explore the nature of optically induced oscillations in a Bose-Einstein condensate contained in a laser ring cavity. In Appendix B, the dynamics of a hybrid system consisting of a magnetized membrane interacting with a spinor BEC are analyzed in detail. The effects of measurement on the state of the system are of particular importance in this section. Lastly, Appendix C applies the ideas of collective dynamics to a much higher energy scenario: excitations in the color (strong) field during relativistic collisions.

In the next few sections, we provide brief introductions to each of these areas of study, beginning with quantum cavity optomechanics.

1.2 Quantum optomechanics

As long ago as the 1870's Maxwell deduced that light would exert a force on the surface onto which it shone [9]. Lebedev made the first experimental demonstration of this phenomenon in 1900 [10]. Because of the extremely feeble nature of these forces – in the best case scenario of normally incident, perfectly reflected light, the recoil force on the surface is the incident power divided by half the speed of light – it at first seems quite unlikely that the effects of a few photons on a mechanical element would ever be significant, and thus a quantum treatment of the phenomenon would be of purely academic value. However, two recent technical developments, spurred on partly by the experimental need for ultraprecise position and force measurements in for example gravitational wave detection and quantum computing [11, 12], have provided a reason to return to this issue. The first is the ultra-high finesse Fabry-Pérot cavity [13, 14], and the second is the ultra-high quality mechanical micro-oscillator [15, 16, 12].

We consider a system as in Fig. 1.1, consisting of a Fabry-Pérot cavity of length L pumped by a laser of frequency ω_l. One end of the cavity is a reflecting oscillator with mass m, stiffness k, and mechanical frequency $\omega_m = \sqrt{k/m}$. We consider only a

single optical cavity mode with annihilation operator a and describe the oscillator by its position x and momentum p. This is necessarily a quantum collective treatment of the mechanical element – we can hardly consider the motion of individual atoms inside the oscillator. Whether it is an actual mechanical mirror oscillating [14], a particular drumhead mode of a membrane interacting with the light field [17], a breathing mode of a microspherical [18] or microtoroidal [16] dielectric cavity, torsion of a micromechanical beam [15], or an LC circuit with a moving capacitor coupled to a microwave cavity [19], the collective motion of the oscillator and its interaction with the light can typically be quantified in terms of the simple operators x and p. The combined system's Hamiltonian is

$$H = \frac{p^2}{2m} + \frac{1}{2}kx^2 + h\frac{nc}{2(L-x)}a^\dagger a \simeq H_{osc} + \hbar\omega_c a^\dagger a + \hbar\frac{\omega_c}{L}a^\dagger a x, \quad (1.13)$$

where n is an integer and $\omega_c = nc/\pi L$ is the unperturbed cavity frequency. Thus, the optical field interacts with the motion of the mirror through a coupling that is linear to leading order. Though this Hamiltonian has been derived for a Fabry-Pérot cavity, many other systems, such as the ones mentioned above, have similar optomechanical interaction terms. In addition, some of these more elaborate setups have been devised to increase the coupling strength [20, 21], generate leading-order quadratic [17] or higher [22] coupling, or to facilitate state transfer between light and mechanical modes [23].

A particularly important feature of such optomechanical systems is that resolved sideband cooling can be used to cool the mechanical element nearly to its quantum ground state [24]. We now sketch how this process occurs. A high finesse Fabry-Pérot cavity (or equivalent) will have an end-mirror with narrow transmission peak at some frequency, say ω_t, and cavity decay constant κ directly proportional to this peak's width. Now, the photons in the cavity generally have frequency ω_c, but they can exchange energy by interacting with the oscillator, resulting in some photons having frequency $\omega_c \pm \omega_m$, a direct consequence of the Doppler effect. Creation of a photon of higher frequency is accompanied by annihilation of a phonon, and vice

versa. If we tune the cavity frequency such that $\omega_t = \omega_c + \omega_m$ then the higher energy photons will escape, and if $\kappa \ll \omega_m$, they will do so much more often than those of lower energy (Fig. 1.2). Thus, there will be a net energy flux out of the mechanical element, reducing its temperature by as much as a few orders of magnitude. In some cases, this will leave the mechanical mode with an expected number of phonons as low as order one [25, 26, 27] or even less than unity [28].

Preparing a mechanical system such that it is nearly in its ground state paves the way not only for the high precision measurements mentioned above but also for tests of quantum effects on macroscopic objects [29]. It is important to keep in mind that it is only a single collective (phononic) mode of the mechanical element that approaches the ground state. Other modes do not typically couple to the light field and thus remain highly excited, i.e., they can be treated by a classical theory. Thus, despite the fact that the various phononic modes of the oscillator arise from the underlying interactions of the exact same constituent particles, one of these may become quantum in nature while the others remain in the classical regime!

Unfortunately, the scheme of cooling outlined above has a technical limit on how low of a phonon occupancy can be reached: it is a fixed fraction of the initial occupancy based on the system's coupling to a thermal reservoir. While there have been recent clever experimental efforts to circumvent these limits [30, 31, 32] it may be easier to consider the optomechanics of a system which begins its existence at a temperature of order μK and which remains extremely weakly coupled to any external environment.

1.3 Bose-Einstein condensation

In 1924, Einstein [33] extended Bose's work on photon statistics [34] to predict a phase transition in which the momentum ground state of a collection of noninteracting bosons would be macroscopically occupied at extremely low temperatures. Despite early excitement over the superfluid properties of liquid ^{4}He in the late

1930's, it turned out that the strong interactions between atoms in that system prevented the zero momentum mode from being dominantly occupied [35]. It was not until 1995 that an almost pure Bose-Einstein condensate phase was produced experimentally out of rubidium and then other alkali atoms [36, 37, 38]. As the present work does not focus in depth on the nuances of BECs, but rather views them in terms of their collective dynamical properties, only a few pertinent points will be summarized.

First of all, Bose-Einstein condensates are typically produced in a very dilute state, with number density $n \approx 10^{18} - 10^{21}\mathrm{m}^{-3}$ as opposed to, say, a gas at STP, which has a density $n \approx 3 \times 10^{25}\mathrm{m}^{-3}$. Yet, at the same time, they need to be cold enough so that there are multiple atoms per de Broglie volume. This ensures that quantum effects, specifically bosonic statistical effects, will be important. Given these constraints, the atoms must be cooled to kinetic energies of order 0.01 - 0.1 neV or equivalently temperatures of order 0.1 - 1 μK before they begin to condense. These ultralow temperatures are achieved through a combination of laser cooling and magnetic trapping which allows evaporative cooling [39]. The resulting condensate, while possessing very weak interparticle interactions, can nevertheless be contained by an extremely loose magnetic or optical trap (trapping frequency of order 10 Hertz, or equivalently, confinement energy of order 100 feV, e.g. [40]). Thus, though there is not a "true" zero momentum mode because of the confinement of the particles, the ground state has an RMS momentum so small as to be effectively zero for most practical purposes.

In addition, the atoms in the condensate are not simply bosonic billiard balls; they typically have a complex internal manifold of electronic states. We wish, however, to avoid exciting electronic states, so we will typically make the atoms interact with light which is far off resonant from any atomic electric dipole transitions. In this case, light will tend to interact weakly with the atoms of the condensate, which will recoil elastically via virtual dipole transitions [41].

Up to this point, we have neglected one important internal degree of freedom of the condensate that can act collectively: namely, its spin. The alkali atoms used to form most BECs will usually have a net non-zero spin. In the case where these spins are not aligned or where spin flips occur, as in a magnetic trap, the condensate will have a shortened lifetime due to hyperfine levels that are not magnetically trapped [37]. On the other hand, if the BEC is transfered to an optical trap, the application of external fields can produce a coherent spin state, that is, a spinor BEC [42]. Because of the extremely slow motion of the atoms in the trap and the cancelation of interparticle magnetic interactions [43], this state can be treated as a coherent spin field, with many interesting applications.

1.3.1 BEC as mechanical element

Now, consider an approximately 1-D BEC confined to a region of length L (and much smaller cross-sectional dimension) in a Fabry-Pérot cavity, as in [44]. The condensate is a bosonic field, so we will initially treat it in terms of its second quantized Schrödinger field operator $\Psi(x,t)$. The optical field in the cavity will be in the form of standing waves of photons of momentum $\hbar k$. As mentioned above, we consider the case where the light is far off resonance from any atomic transitions. The atoms in the condensate can still be excited to states of center-of-mass momenta $2\hbar kn$ (n an integer) by successive elastic scatterings of photons via virtual electric dipole transitions. We quickly derive the effective Hamiltonian leading to these dynamics. Because the wavelength of visible is so much larger than the atomic radius, we may use the electric dipole approximation [45]. A single two level (ground state $|0\rangle$ and excited state $|1\rangle$) atom with transition frequency ω_a interacting with a cavity field $\vec{E}$ will thus have the Hamiltonian

$$H = \vec{E}\cdot\vec{d}|0\rangle\langle 1| + \vec{E}^{\dagger}\cdot d^{*}|1\rangle\langle 0| + \hbar\omega_a|1\rangle\langle 1|, \tag{1.14}$$

where $\vec{d}$ is the atomic dipole transition moment. We do not include here the light field Hamiltonian. Taking the cavity field to be composed of two modes of momentum $\pm\hbar k$ propogating in opposite directions (that is, decomposing the standing wave) and working in a frame rotating at ω_c (to remove explicit time dependence of $\vec{E}$) the electric field operator is

$$\vec{E} = \mathrm{i}\sqrt{\frac{\hbar ck}{2\epsilon_0 V}}\left(a_1\vec{e}_1 e^{\mathrm{i}kx} + a_2\vec{e}_2 e^{-\mathrm{i}kx}\right), \tag{1.15}$$

where V is the cavity volume, a_i are photon annihilation operators, and $\vec{e}_i$ are the polarization vectors. We now take the atom's state to be $|\phi\rangle = m_0|0\rangle + m_1|1\rangle$ and use Schrödinger's equation with (1.15) substituted into the Hamiltonian to find the time derivatives of m_i:

$$\mathrm{i}\hbar\frac{dm_0}{dt} = -\mathrm{i}\sqrt{\frac{\hbar ck}{2\epsilon_0 V}}d^*\left(a_1^\dagger e^{-\mathrm{i}kx} + a_2^\dagger e^{\mathrm{i}kx}\right)m_1, \tag{1.16}$$

$$\mathrm{i}\hbar\frac{dm_1}{dt} = \hbar(\omega_a - \omega_c)m_1 + \mathrm{i}\sqrt{\frac{\hbar ck}{2\epsilon_0 V}}d\left(a_1 e^{\mathrm{i}kx} + a_2 e^{-\mathrm{i}kx}\right)m_0. \tag{1.17}$$

Here the atomic frequency is shifted because we are working in the rotating frame. As the light is far off resonance, we expect that the excited state remains very nearly unoccupied. The adiabatic elimination procedure consists of setting Eq. (1.17) equal to 0, solving for m_1, substituting back into (1.16), and finding the effective Hamiltonian that produces this equation of motion for m_0 without the presence of the excited mode. This is straightforward, and we obtain

$$H_{\text{eff}} = \frac{\hbar g_0^2}{\omega_c - \omega_a}\left(a_1^\dagger a_1 + a_2^\dagger a_2 + a_2^\dagger a_1 e^{2\mathrm{i}kx} + a_1^\dagger a_2 e^{-2\mathrm{i}kx}\right)|0\rangle\langle 0|, \tag{1.18}$$

where $g_0 = \sqrt{\frac{\hbar ck}{2\epsilon_0 V}}|d|$ is the resonant Rabi frequency. The error of the adiabatic elimination procedure can be quantified more precisely [46], but it is generally valid if $g_0 \ll |\omega_c - \omega_a|$, that is, for large detunings. To account for many atoms in the cavity, we second quantize the atomic field using its field operator $\Psi(x,t)$ and the interaction Hamiltonian is just

$$H_{\text{int}} = \int \Psi^\dagger(x,t)\frac{\hbar g_0^2}{\omega_c - \omega_a}\left(a_1^\dagger a_1 + a_2^\dagger a_2 + a_2^\dagger a_1 e^{2\mathrm{i}kx} + a_1^\dagger a_2 e^{-2\mathrm{i}kx}\right)\Psi(x,t)dx. \tag{1.19}$$

Now, although we expanded the two light modes independently, the symmetry of the optical standing wave will tend to excite atoms into symmetrical superpositions of momenta $2k$ and $-2k$, i.e. the matter wavefunction will be (co)sinusoidal. Considering only the zero momentum and first excited center-of-mass mode of the BEC (when the incident light is feeble, these will be by far the dominantly occupied modes), we expand its field operator, including only the terms containing the single mode annihilation operators c_0 and c_1,

$$\Psi(x,t) = \frac{c_0(t)}{\sqrt{L}} + \sqrt{\frac{2}{L}} c_1(t)\cos(2kx). \tag{1.20}$$

Next, we evaluate the mean particle density,

$$\begin{aligned}\langle \Psi^\dagger(x,t)\Psi(x,t)\rangle &= \frac{1}{L}\Big(\langle N_0(t)+N_1(t)\rangle + \sqrt{2}\langle c_0^\dagger(t)c_1(t)+c_1^\dagger(t)c_0(t)\rangle\cos(2kx) \\ &+ \langle N_1(t)\rangle\cos(4kx)\Big), \end{aligned}\tag{1.21}$$

where $N_i = c_i^\dagger c_i$. Therefore, the collective mode excited by the interaction between the light and the atoms is a spatially sinusoidal, time-dependent density fluctuation in the condensate. By substituting x and p operators for the c's, this problem can be cast in an optomechanical form. A specific example of this type of "bottom-up" optomechanical system is investigated in detail in Appendix A, which will in particular highlight the difference in dynamics between atoms trapped in a Fabry-Pérot cavity and those trapped in a ring cavity.

1.3.2 BEC magnetometry

We now discuss the application of spinor BECs to ultraprecise magnetometry. Observation of the Larmor precession of a spinor BEC via phase contrast imaging is a powerful tool to measure magnetic fields, competing with and potentially exceeding SQUIDs in terms of both magnetic field sensitivity and spatial resolution [47]. To illustrate how this works more concretely, we present a brief discussion of the phase contrast measurement scheme.

Due to a difference in Clebsch-Gordon coefficients for different polarizations of incident light that drive virtual transitions between hyperfine levels of the condensate atoms, the spinor condensate will exhibit birefringence. By passing a circularly polarized beam of light (taken to be travelling in the y-direction) through the condensate and measuring the accumulated phase shift, we can gain information about the BEC's spin wavefunction. For light far detuned from an electrical transition of narrow linewidth, absorption will be negligble. Thus, we need only worry about the real part of the index of refraction to calculate the phase shift of the probe light relative to light traveling through empty space. From elementary optics this shift will be

$$\phi = \frac{\omega}{c}\int (n(y)-1)dy. \tag{1.22}$$

Consider at first only the transition from the $F = 1$ to $F' = 2$ hyperfine manifolds of ^{87}Rb. Take this transition to have frequency ω_0 (wavelength λ_0) and natural linewidth γ. Use probe light with frequency ω such that $\omega_0 > \omega \gg \Delta_2 = \omega_0 - \omega \gg \gamma$. Under these restrictions, we can arrive at an approximate expression for the index of refraction [48],

$$n \simeq 1 - \sum_j \frac{\rho A_{j,i} c^3}{8\pi\omega_0^3 \Delta_2}, \tag{1.23}$$

where ρ is the number density of the condensate and $A_{j,i}$ is the Einstein coefficient of the dipole transition from state j in $F' = 2$ to state i in $F = 1$. We can then use the Wigner-Eckart theorem and the Clebsch-Gordon coefficients for σ_+ polarized light and the various y spin components to compute the Einstein A's. Putting this together with (1.22) and replacing the prefactor $\omega \to \omega_0$, we attain the phase shift,

$$\phi = \frac{1}{4}\bar{n}\sigma_0 \frac{\gamma}{2\Delta_2}\left(1 + \frac{5}{6}\langle F_y\rangle + \frac{1}{6}\langle F_y^2\rangle\right). \tag{1.24}$$

Here $\bar{n}$ is the column number density of atoms in the condensate and $\sigma_0 = 3\lambda_0^2/2\pi$ is the resonant cross section of optical absorption. We have also taken the spin state

of the atoms in the condensate to be specified by a single wavefunction

$$|\Psi\rangle \;=\; m_+|+_y\rangle + m_0|0_y\rangle + m_-|-_y\rangle, \tag{1.25}$$

and we define the spin expectation values in the usual way,

$$\begin{aligned} \langle F_y\rangle &= |m_+|^2 - |m_-|^2, \\ \langle F_y^2\rangle &= |m_+|^2 + |m_-|^2. \end{aligned} \tag{1.26}$$

When we look at the actual levels of ^{87}Rb, probe light which is fairly red-detuned from the $F = 1 \rightarrow F' = 2$ transition will be comparably blue-detuned from the $F = 1 \rightarrow F' = 1$ transition [49]. Let the probe light's detuning from the latter be Δ_1 and define the ratio $\delta = \Delta_2/\Delta_1$. Accounting for the contributions from both virtual transitions gives the final observed phase shift,

$$\phi \;=\; \frac{1}{4}\bar{n}\sigma_0\frac{\gamma}{2\Delta_2}\left[\left(1-\frac{1}{3}\delta\right) + \frac{1}{6}\langle F_y\rangle\,(5+\delta) + \frac{1}{6}\langle F_y^2\rangle\,(1+\delta)\right]. \tag{1.27}$$

We look into the effects of making such a dispersive measurement in the next section in order to expand on and make precise the comments on measurement operators in Appendix B.

1.4 Quantum back-action of weak measurements

Under von Neumann's measurement postulate [50], the effect on a system of measuring some physical quantity (an observable) is to collapse (or project) the system's wavefunction into the eigenstate of the observable corresponding to the measured value. However, for many experiments it is undesirable to perform such a "destructive" measurement – the system could have initially been in a superposition of numerous (or even infinitely many) initial states, and the measurement reduces it to only one of these. The trade off for not doing a measurement that projects the system into a particular state is that one cannot in general be completely certain of

the final quantum state of the system after measurement. Consider an ensemble of experimental systems described by a density matrix ρ, on which we measure some observable O with outcomes o_i described by measurement operators W_i (this can easily be extended to continuously valued observables). The probability of measuring a particular o_i is

$$P(o_i) \quad = \quad \mathrm{tr}(W_i \rho), \tag{1.28}$$

and, after the measurement, the system's density matrix is

$$\rho_{\mathrm{after}} \quad = \quad \frac{M_i \rho M_i^\dagger}{P(o_i)}, \tag{1.29}$$

where

$$M_i^\dagger M_i \quad = \quad W_i. \tag{1.30}$$

The operators M_i are known as the Kraus representation of the measurement process.

We pause to make a few comments before proceeding. First, if the M_i (or, equivalently, in this case, the W_i) are replaced by projectors, the usual von Neumann measurement formalism is reproduced. Second, one could define $M_i' = U_i M_i$ for arbitrary unitary operators U_i without altering immediately the probabilities of the various outcomes. The full details of the measurement and its effect on the system are taken into account by examining an expanded interaction Hamiltonian incorporating the measuring device, whose state is later traced over, thereby arriving at the physically correct U_i's. Also, the probabilities of all possible outcomes will add up to 1 if we require

$$\sum_i W_i = I, \tag{1.31}$$

with I the identity operator. Lastly, there is a technical requirement that the operators W_i be completely positive; that is, roughly speaking, that they yield a valid

probability between 0 and 1 not just when acting on the experimental system but also on any composite system containing the experiment as a subsystem (their action on the other part of the composite is taken to be the identity). This final requirement will in particular allow us to consider not only the effects of measurement on the system in isolation but also when it is coupled to another system or the environment.

If a particular measurement outcome is consistent with several possible quantum states, we hypothesize that the operator W_i is a sum over projectors onto the states with which the measurement is consistent. If these states are not linearly independent, the operator will have to be normalized to adhere to (1.31).

1.4.1 Application to phase contrast imaging

We now apply these ideas to the specific situation of phase contrast imaging. We already saw that for a BEC with spin wavefunction (1.25), the phase contrast signal will be related only to the values $|m_i|^2$ (for this short discussion, $i = +1, 0, -1$) by (1.27); that is, measuring a particular ϕ does not uniquely specify the quantum state but only specifies a certain relationship amongst the coefficients of the wavefunction. In particular, define a rescaled phase Φ in terms of the experimentally measured phase ϕ and the above constants,

$$\Phi = 6 - \frac{24\Delta_2}{\bar{n}\sigma_0\gamma}\phi;\ 0 \leq \Phi \leq 5 + \delta. \tag{1.32}$$

Then, post-measurement, we have constraints on the m_i's:

$$\begin{aligned} \Phi &= (3+\delta)|m_0|^2 + (5+\delta)|m_-|^2, \\ 1 &= |m_+|^2 + |m_0|^2 + |m_-|^2. \end{aligned} \tag{1.33}$$

For a given value Φ, these constraints specify an allowed curve of values for $|m_i|$, plotted in Fig. 1.3. To find the measurement operator W_Φ corresponding to a

particular Φ, we add (integrate) all projectors onto allowed states,

$$\begin{aligned} W_\Phi &= \int |\Psi\rangle\langle\Psi| d^3 m_i \\ &= \int |m_+|^2 |+_y\rangle\langle+_y| + |m_0|^2 |0_y\rangle\langle 0_y| + |m_-|^2 |-_y\rangle\langle -_y| ds \\ &= \bar{w}_+^\Phi |+_y\rangle\langle+_y| + \bar{w}_0^\Phi |0_y\rangle\langle 0_y| + \bar{w}_-^\Phi |-_y\rangle\langle -_y|, \end{aligned} \tag{1.34}$$

where we understand the integrand in the first line of (1.34) to be multiplied by delta functions corresponding to the constraints (1.33). Note that the off-diagonal terms vanish when integrating over all possible phases of the m_i. Also, we are summing over an overcomplete set – an infinite number of states overdetermines a space of dimension 3 (despite situations where the contrary assumption seems to work [51], here we have $3 \ll \infty$) – so the W_Φ need to be multiplied by a normalization $6/\pi$, as determined by (1.31). The values of the $\bar{w}_i^\Phi$ are plotted as functions of Φ in Fig. 1.4. Assuming for now that the phase contrast measurement has the minimum possible effect on the BEC, we take the M_Φ operators of the previous section just to be the real, diagonal matrix square roots of the W_Φ's, with no additional unitary effect on the system.

What remains is to see if these operators can reproduce the observations of Larmor precession in BECs seen in experiments such as [47]. A few simulations of a condensate initially prepared in the $F_x = +1$ state, allowed to Larmor precess in a uniform magnetic field in the z direction, and subjected to phase contrast measurements by light along the y axis at a frequency of 8 per Larmor period, are shown in Fig. 1.5. Clearly, something is missing from the treatment above.

What we have failed to consider is that, while the BEC can be accurately described by a single spin wavefunction, it is not a single atom. Fig. 1.5 shows what would happen if one tried to observe the Larmor precession of a single atom – it would produce almost a random signal. One can monitor discrete spin flips of a single atom, but not its phase. Therefore, we use the following procedure to describe weak measurements on a bosonic system of N atoms. Consider N separate

measurements on the N atoms in the condensate. Each can give a different value Φ_n. But the overall signal measured would be the mean value of these; call it $\bar{\Phi}$. Because of bosonic enhancement, the spins in the condensate, if initially aligned, will tend to remain so after the measurement procedure (more precisely, there is a significantly higher statistical weight in the full N-particle density matrix for aligned spins). Therefore, rather than applying to each atom its own W_{Φ_n}, we instead apply to the collective spin density matrix the averaged operator

$$\bar{W} \;=\; \frac{1}{N}\sum_{n=1}^{N} W_{\Phi_n}. \tag{1.35}$$

Then, to find the post-measurement density matrix, we use (1.29), substituting the $\bar{M}$ such that $\bar{M}^2 = \bar{W}$. The signal obtained by applying this procedure to various numbers of atoms N and at various measurement frequencies is shown in Fig. 1.6. In addition, the evolution of the expectation values of $\langle F_x \rangle$ and $\langle F_y \rangle$ are plotted for a few combinations of N and measurement frequencies in Figs. 1.7. This theoretical treatment thus preserves the Larmor precession as expected for frequencies up to about 16 measurements per Larmor period. However, the model makes an additional interesting prediction: without any extra feedback, which is present in [52], measuring the phase too frequently causes the spin dynamics to become dominated by the measurement procedure, rather than the applied magnetic field. This prediction is robust not only as a function of N but also as a function of the phase measurement uncertainty (all plots shown are for $\Delta\Phi = 0.01$, but, aside from granularity in the case of small N, the exact same effect is observed for $\Delta\Phi = 0.1$ and 0.001). This phenomenon may be related to the quantum anti-Zeno effect [53]. It should be quite feasible, using current technology or even current experimental apparatus already in place, to make a test of this prediction. We now leave the realm of ultracold atoms and turn to a quite different application of collective dynamics.

1.5 The strong force and color fields

The first successful model of nuclear binding was in terms of a nuclear force mediated by a massive, and hence short-range, scalar Yukawa meson [54]. Yet this force between nucleons is not fundamental. Rather, it is much like the van der Waals interaction between molecules, which arises from the Coulomb interaction between their underlying charge distributions. Similarly, the nuclear force is a residual effect of a more fundamental strong force acting on the underlying distribution of constituents in the nucleons.

Because of the huge number of hadrons that had been observed by the 1960's, Gell-Mann proposed the "eightfold way" to categorize them in terms of an SU(3)-flavor symmetry [55, 56]. This quickly led to the idea of three (at the time) flavors of fermionic quarks out of which all the hadrons were composed [57, 58]. However, this theory had a slight defect: certain particles, like the Ω^-, appeared to contain quarks that disobeyed the Pauli exclusion principle (two of the Ω^-'s quarks appear to have identical spin, flavor, and spatial wavefunctions) [59]. This issue was resolved by attaching an additional degree of freedom to quarks that became known as color charge. The force between these charges is known as the color or strong force. To gain a better understanding of color charge, we compare it to the more familiar electric charge.

Quantum electrodynamics is a theory of the electromagnetic interaction in terms of a local U(1) gauge symmetry. U(1) is a one dimensional group with, consequently, one generator. It thus has one type of electric charge (with two possible signs), one conserved current, and one force-mediating gauge boson, the photon. Quantum chromodynamics, on the other hand, is a theory of the strong interaction which obeys a local SU(3)-color gauge symmetry. This symmetry group has eight generators typically represented in QCD by the Gell-Mann matrices [60], and it is non-Abelian (the generators do not generally commute). There are thus three color charges,

three anticolor charges, eight conserved color currents, and eight bosons, the gluons, associated with the eight generators of the group.

It is this richer, non-Abelian structure of QCD's symmetry group that gives rise to its most interesting phenomena. We contrast the QED and QCD Lagrangians (focusing on the field-only terms, where the biggest discrepancies are) [61]:

$$\begin{aligned} \mathcal{L}_{\mathrm{QED}} &= -\frac{1}{4}F^{\mu\nu}F_{\mu\nu}, \\ F_{\mu\nu} &= \partial_\mu A_\nu^{\mathrm{photon}} - \partial_\nu A_\mu^{\mathrm{photon}}, \end{aligned} \tag{1.36}$$

$$\begin{aligned} \mathcal{L}_{\mathrm{QCD}} &= -\frac{1}{4}G_a^{\mu\nu}G_{\mu\nu}^a, \\ G_{\mu\nu}^a &= \partial_\mu A_{a\nu}^{\mathrm{gluon}} - \partial_\nu A_{a\mu}^{\mathrm{gluon}} - g f^{abc} A_{b\mu}^{\mathrm{gluon}} A_{c\nu}^{\mathrm{gluon}}. \end{aligned} \tag{1.37}$$

Here F and G are the electromagnetic and color field tensors, respectively, the A's are the photon and gluon fields, g is the color charge, a, b, c are color indices from 1 to 8 (which can be raised or lowered freely) and the f's are the structure constants of the SU(3) group,

$$[\lambda_a, \lambda_b] = 2\mathrm{i} f^{abc}\lambda_c, \tag{1.38}$$

with λ_a the Gell-Mann matrices (note that Einstein summation is followed for the color indices as well as the space-time ones). The f's are antisymmetric (it is obvious for the first 2 indices, but it also turns out to be the case for the third index). This is why there is no third term in (1.36) which is quadratic in A^{photon}: there is only one photon field and so the only such term that could be constructed would have a coefficient of 0. A more physical way of saying this is that photons do not carry the electromagnetic charge to which they couple, but gluons do carry color charges and hence the color fields they mediate are inherently nonlinear. When we consider the Feynman rules for QED, the F^2 term generates only terms quadratic in A, so in a matter-free universe, the only rule for photons is the propagator. On the other hand, in the QCD Lagrangian, G^2 produces terms proportional to A^2, A^3, and even A^4. This means the Feynman rules for gluons include not just the propagator but also

three and four gluon vertices. While the inclusion of matter in the QED Lagrangian allows light to scatter from light, these processes must be mediated by matter loops and hence are suppressed by powers of both the coupling strength α_{EM} and inverse powers of the electron mass m_e.

The inherent nonlinearity of QCD would not be such a problem if a perturbative approach were valid. However, in contrast to QED, where $\alpha_{\mathrm{EM}} \approx 1/137$, in QCD α_{S} (and g) is of order 1 at low energies, and, though it decreases somewhat in high energy collisions, it is still significantly larger than α_{EM}. Therefore, perturbative expansions in terms of gluon and quark loops fail in many circumstances.

The consequences of this fact are striking. We have essentially no chance of talking about the effects or even the existence of a single gluon in anything but the highest energy situations. They are too sticky to be singled out. Therefore many strong force phenomena are intrinsically non-perturbative (in terms of the fundamental gluon and quark fields – however one can often find some small ratio and perform an effective expansion in powers of that ratio) effects due to the collective action of color fields and charges. This fact has long been recognized, and many phenomenological models of strong physics are collective in nature (though not always quantized). Some early examples include the bag model [62], the string breaking model [63], and the NJL model [64]. Also, the use of quasiparticles in the study of strong phenomena is nearly as prevalent as it is in solid state physics. Prominent among these are constituent (vs. current) quarks [65] and instantons [66]. It is thus apparent that the work in Appendix C follows a long tradition of collective dynamical treatment of color fields.

1.6 Dissertation format

The preceding sections have outlined the basic ideas needed for the rest of this work. In particular, quantum collective dynamics will be applied to three different problems. Appendix A includes work on BECs as optomechanical systems. I performed

the calculations in and wrote this section under the supervision of Pierre Meystre. Appendix B deals with a hybrid BEC-membrane system and focuses on the effects of measurements. Many authors have collaborated on this work; besides me, these are Swati Singh, Mehmet Tasgin, Pierre Meystre, Mukund Vengalattore, and Keith Schwab. My contribution to the work was a significant fraction of the computations and writing. In particular, I did some of the calculations in section 3 and all of the calculations and writing in sections 4 and 5 and subsections 7.2 and 7.3. I developed the formalism to compute the weak back-action effects of phase contrast imaging. Also, I wrote the Mathematica code to plot the Wigner distributions used in several figures. Appendix C deals with collective oscillations of the color field between two quarks. This research was performed and written up under the supervision of my quondam advisor, Johann Rafelski. In Chapter 2, a summary of the major results from each of these projects is presented.

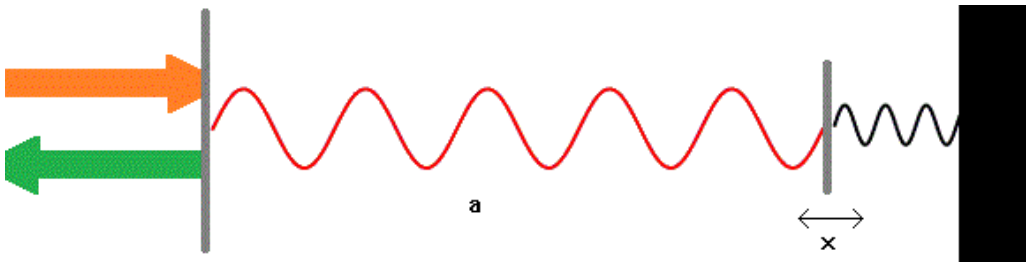

Figure 1.1: The canonical optomechanical setup. Light is pumped into a cavity where it exerts radiation pressure on a mechanical oscillator. Measurement of the output light can give information about or induce quantum back-action on the oscillator.

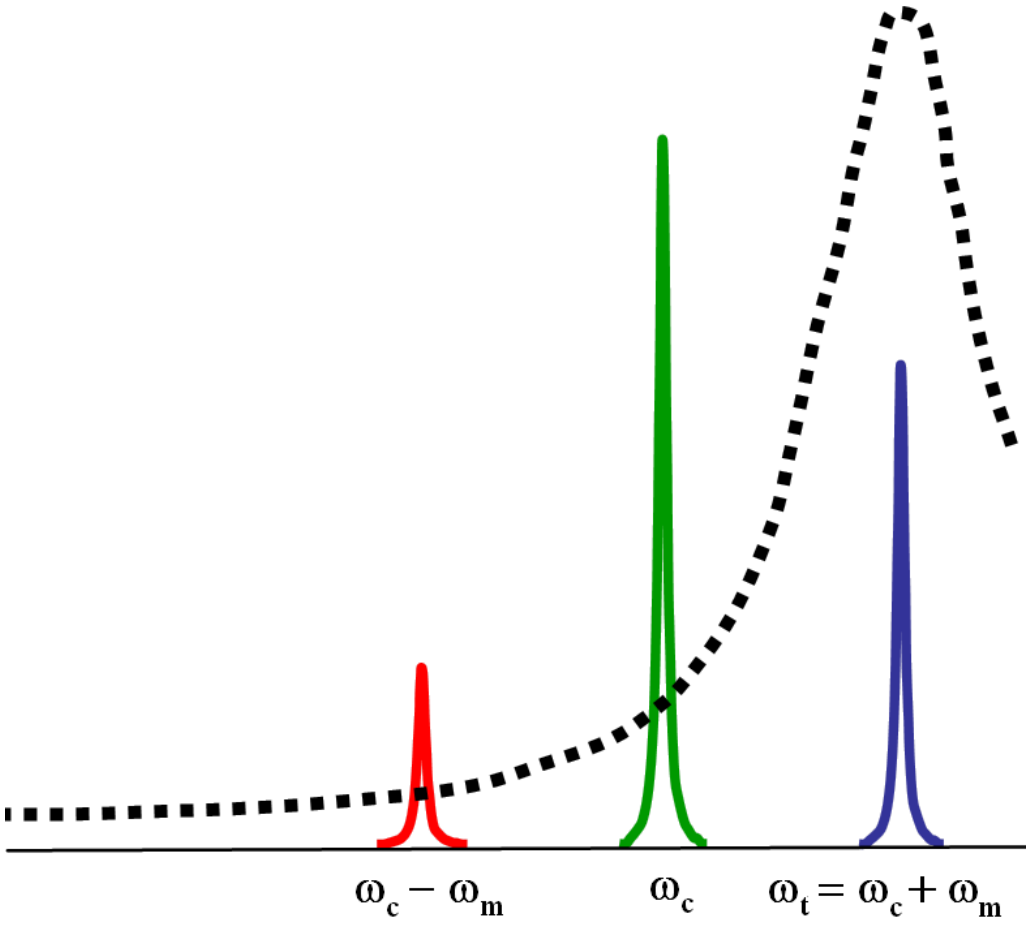

Figure 1.2: An illustration of the frequency relationships used in resolved sideband cooling. The dashed line is the Fabry-Pèrot cavity's transmission as a function of frequency. The central colored peak is the cavity light frequency, and the others are the sidebands. In this setup, light which has absorbed energy from the oscillator is more likely to escape.

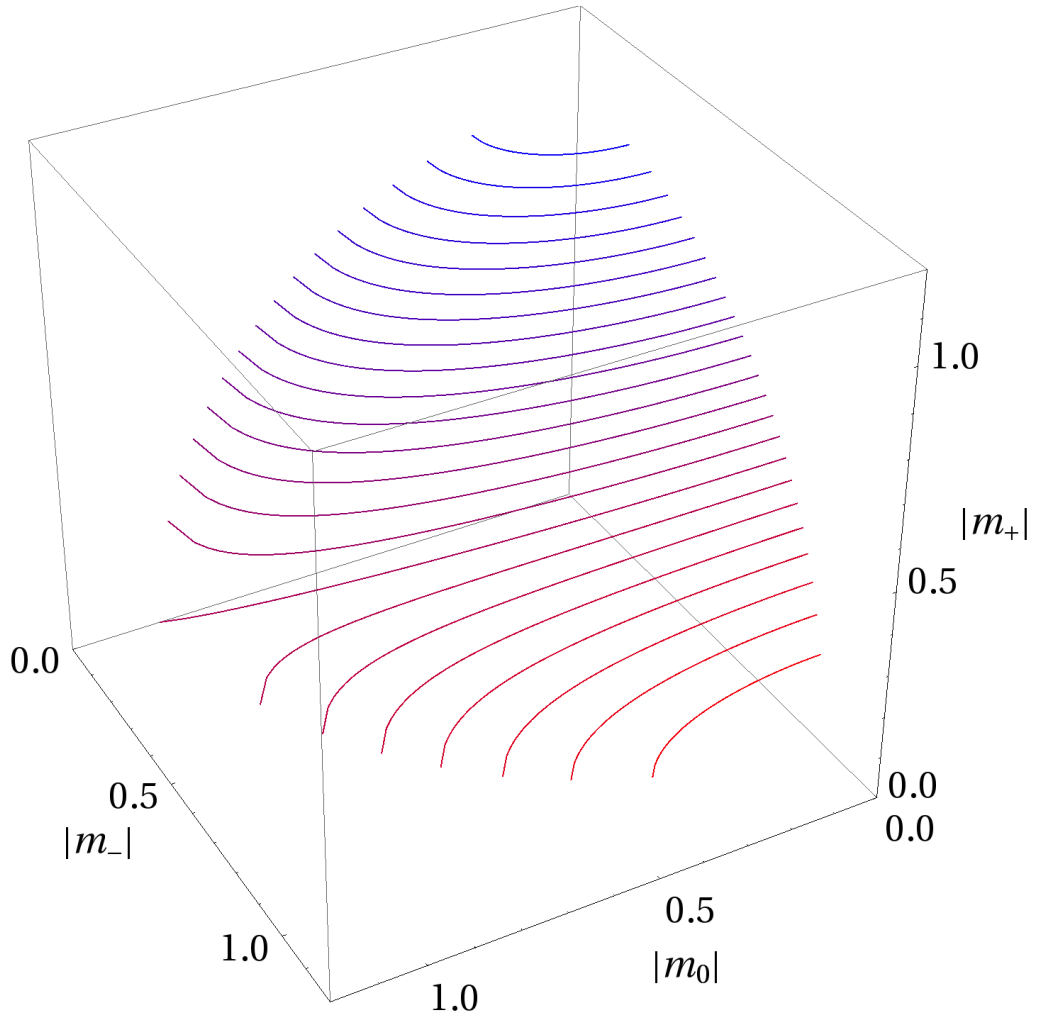

Figure 1.3: The constraints imposed on the coefficients of the spin wavefunction by a particular measurement, (1.33), plotted for various measurement outcomes Φ. Smaller values of Φ are in blue and occur higher along the vertical axis.

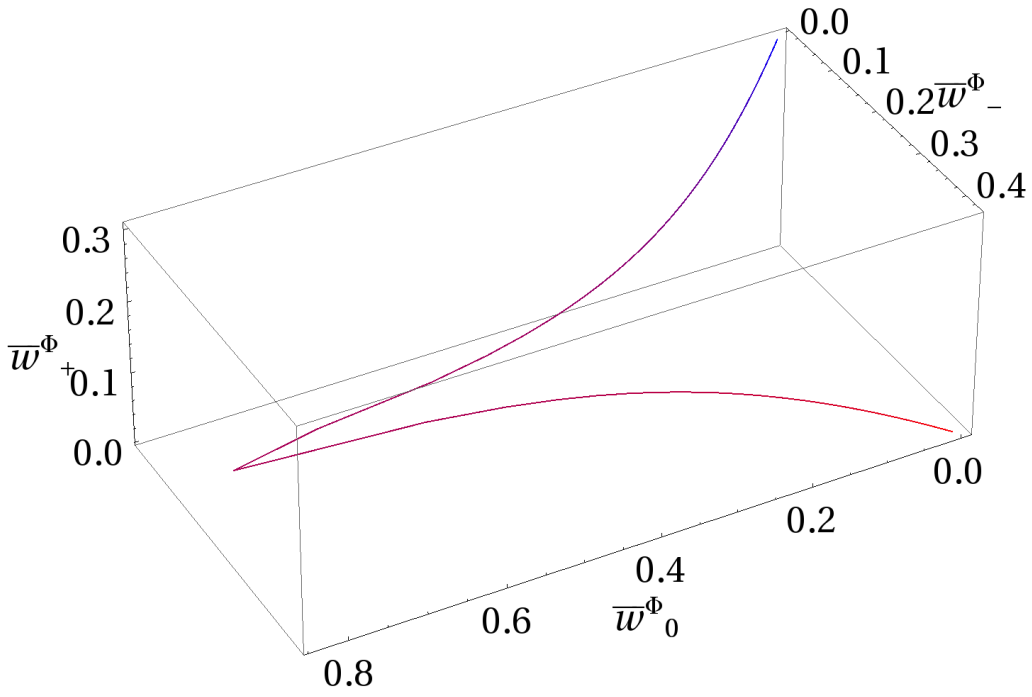

Figure 1.4: The coefficients of the operators W^{Φ} as a function of Φ. Lower values, in blue, predominantly project onto $|+\rangle\langle+|$, medium project onto $|0\rangle\langle 0|$, and large values, in red, onto $|-\rangle\langle-|$

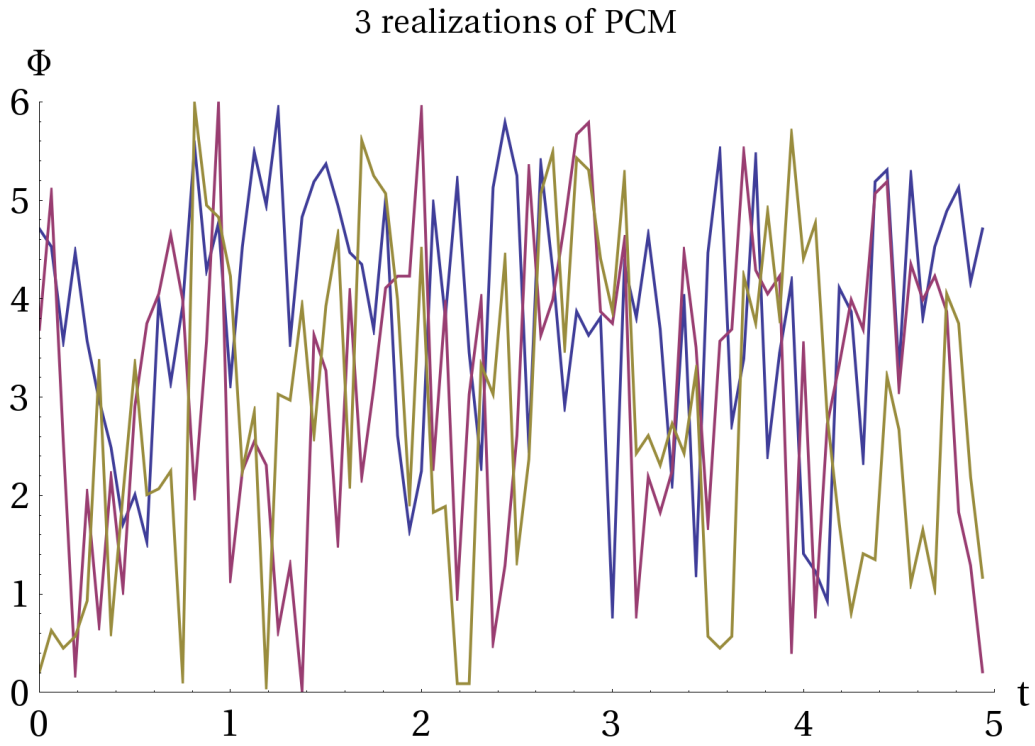

Figure 1.5: Three realizations of a sequence of phase contrast measurements occuring 16 times per Larmor period. Time is on the x axis and the signal is on the y axis. Nothing like a periodic signal is apparent.

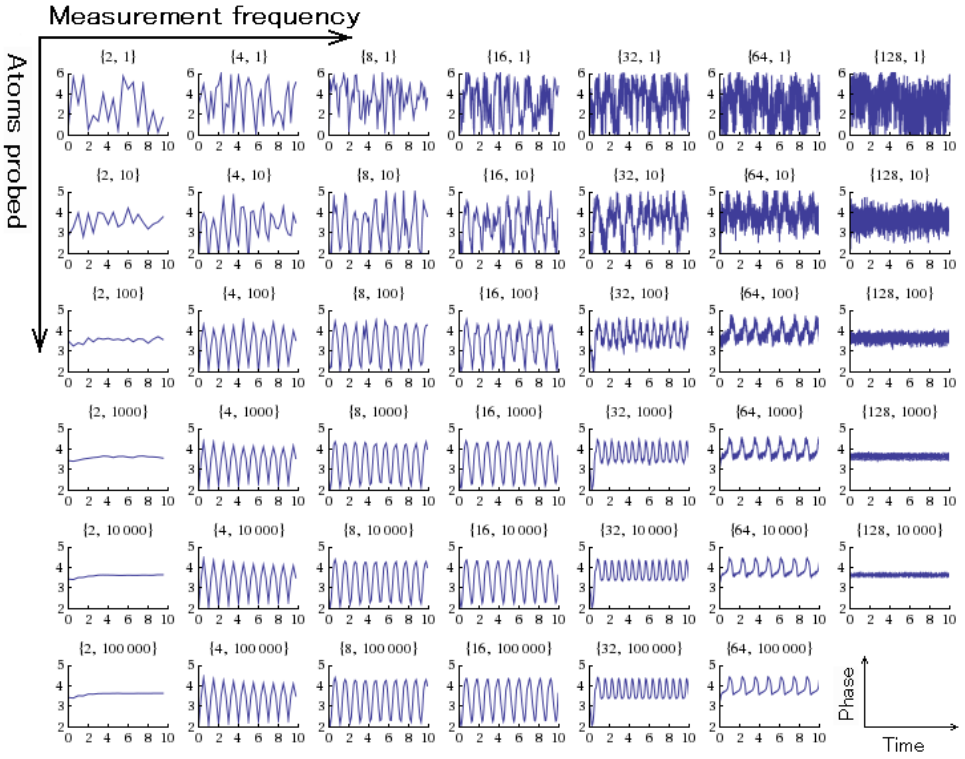

Figure 1.6: Illustration of realizations of the measurement operator scheme outlined above as N and the measurement frequency are varied. In each figure, time is on the x axis and signal is on the y axis. Overall, each column has double the number of measurements per Larmor period of the column before, starting with 2 at the left and reaching 128/period at the right. Each row has 10 times the number of atoms being averaged over as the one above, starting with 1 at the top and reaching 100000 at the bottom. The lower right corner is missing due to the exponential growth in computation time required. We note that the measurement process seems to perturb and then completely disrupt the normal evolution if it occurs too frequently, regardless of N.

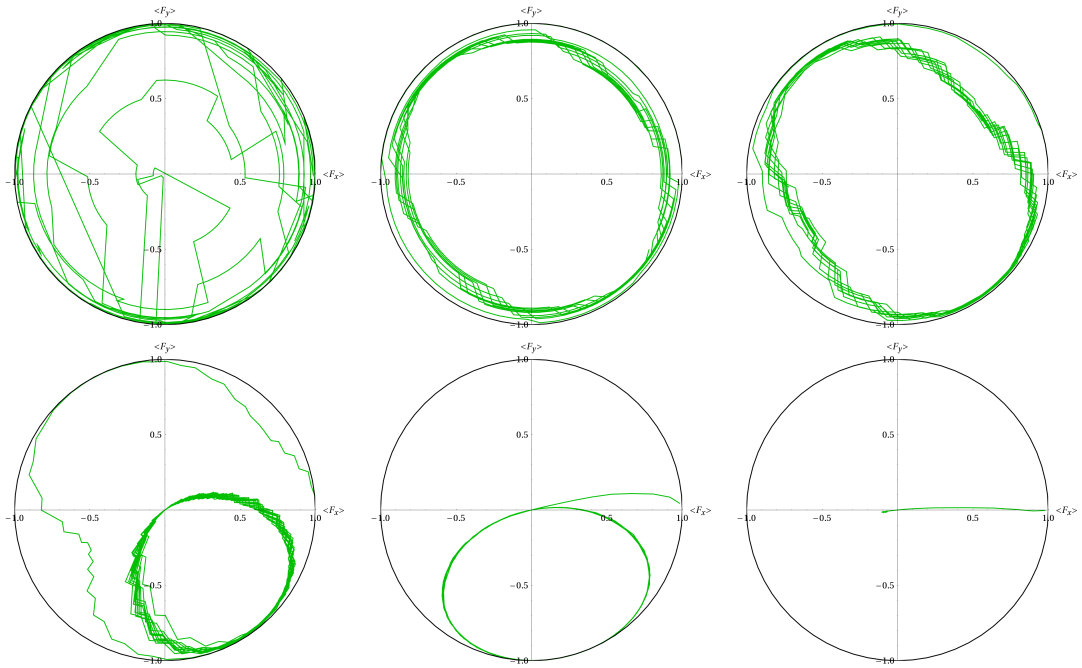

Figure 1.7: Plots of Larmor precession subject to periodic measurements. The axes are $\langle F_x \rangle$ and $\langle F_y \rangle$. In the top left, N=1 and the frequency of measurements f_m = 8 per Larmor period. In all others N=1000, and, reading left to right from the top center, f_m = 8, 16, 32, 64, 128. The unperturbed evolution is the black circle in each figure. Averaging the measurement effect over many atoms clearly disturbs the Larmor precession much less than not doing so. As the phase contrast measurements are made more frequently, they disturb the dynamics more strongly, ultimately causing a complete decoherence of the condensate's spin.

CHAPTER 2

Present Study

The three appendices of this document contain the theory, results, and conclusions of this study. The following is a brief presentation of the key results of these papers.

2.1 Quantized dynamics of a BEC in an optical ring cavity

As mentioned above, density fluctuations in a Bose-Einstein condensate can be treated by the quantum collective action of the field creation and annihilation operators. When excited by off-resonant interactions with feeble light in a ring cavity, a slightly more complex situation than the one explained in Section 1.3.1 arises. This is because, contrary to those in a standing wave, the photons in a ring cavity still contain directional information. In other words, the photon modes of momenta $\pm\hbar k$ are independent and do not have to be combined symmetrically to form cavity modes. This allows the photons to couple not only to the symmetric matter mode of momentum $2\hbar k$, but also to the antisymmetric mode of the same momentum. This latter matter mode's spatial wavefunction will be a sine function rather than a cosine, so we distinguish the two modes by calling them "cosine" and "sine" modes. In addition, we include the evolution of the zero momentum mode (in contrast to the approach used in other studies [44, 67]), and that of the two counter-propagating optical fields, for a total of five interacting fields. The cosine mode is excited from the zero momentum mode by interaction with a symmetric (under interchange of the two light fields) light operator, and similarly the sine mode is excited by interaction with an antisymmetric light operator.

To narrow the study, we work on the case where the light fields are pumped by

sources of the same intensity and phase so that, naïvely, the intracavity fields should be the same and thus the sine mode, at a classical (ignoring quantum fluctuations and treating operators as c-numbers) level, should be unoccupied or "dark." Yet we find that this is not always the case; for certain parameter ranges, the system exhibits spontaneous symmetry breaking and the sine mode acquires a finite occupancy. On top of this, there is optical bi– or even multistability: two distinct steady states (or two different stable cycles) of the system can be reached, depending on the initial state of the light and matter fields. One additional result is that the zero momentum mode shows appreciable depletion and gains a complex phase. Specifically, the usual ansatz for this mode's creation and annihilation operators $c_0, c_0^\dagger \to \sqrt{N}$, where N is the number of atoms in the condensate, differs appreciably from the observed behavior $c_0 \to \sqrt{N-n}e^{\mathrm{i}\phi}$.

We next restrict our inquiry to the parameter region where the dark sine mode is stable and then linearize the Heisenberg-Langevin equations of motion about the steady state values. Under these restrictions, we find that quantum fluctuations become quite large near the classical bifurcation points of the system. That is, the number of atoms in the cosine mode differs from the previous steady state prediction, and the number in the sine mode is on average many, rather than none. These fluctuations will cause the bifurcation points to shift and may even facilitate quantum tunneling between macroscopically distinct behaviors of the condensate.

2.2 Hybrid membrane - condensate system with measurement back-action

The system considered in Appendix B consists of a spinor BEC trapped a few microns from a high quality micromechanical membrane. The membrane is coupled to the condensate via a high-gradient magnet attached to its surface. Taylor expanding the dipole-dipole interaction between the two gives a linear coupling between the membrane's position and the condensate's spin. By using phase contrast imaging to measure changes in the local magnetic field, the goal is to obtain detailed

information about the oscillator's motion.

However, any measurement on the condensate will necessarily induce some back-action on it. Because of the coupling between them, the membrane and the condensate are entangled, so back-action on the condensate also perturbs the membrane. If we take the magnetic field gradient to point along the z axis, then the interaction that entangles the two can be expressed as

$$V_{\text{osc}} = \frac{1}{2} m\omega^2 \left(x - AF_z\right)^2 , \tag{2.1}$$

where A is a length scale we have termed the "back-action" parameter which is related to the strength of the coupling. For realistic experimental parameters, A can be of the same order as the oscillator zero-point motion distance. The operator F_z commutes with the Hamiltonian, and specifically with both x and p. Thus, from the perspective of the membrane's dynamics alone, it might as well be a c-number. However, in the combined system density matrix, it is possible that the condensate's spin will be a superposition of multiple F_z states. Each of these spin components will shift the equilibrium position of the oscillator differently, effectively creating multiple potential wells simultaneously. In particular, putting the condensate intially in a spin state $F_x = 1$ the membrane to three spatially separated potential wells of equal strength. This interaction puts the membrane into a superposition state. A measurement of the spin of the condensate in the y (or x for that matter) direction does not resolve which well the oscillator was interacting with and therefore leaves it in a superposition of states distinct in position and momentum. We compute the density matrix of the system after an arbitrary number of measurements interspersed with periods of free evolution. This is done for both a membrane initially in thermal equilibrium with its surroundings and one which has been prepared in a coherent state. Each of n measurements will typically increase the number of possible interactions the oscillator may have had by a factor of three, creating up to 3^{2n} distinct terms in the density matrix. The interference between these terms is a purely quantum effect. Specifically, by making successive strong (projective) measurements of the

condensate's y component of spin, à la the Stern-Gerlach experiment, the membrane can be put into non-classical (having negatively valued Wigner function) states that resemble displaced Fock states and even Schrödinger cat states. It remains to be seen what the effects of repeated weaker measurements, as in Section 1.4, are on the state on of the membrane.

2.3 Collective dynamics of a color string and impact on particle production

The Schwinger mechanism for particle production is a tunneling process that occurs in intense fields [68]. In this process, a virtual particle tunnels out of the Dirac sea, creating a real charged particle-antiparticle pair. The charges on these new particles in turn screen the fields, reducing the fields' energy content enough to compensate for the mass-energy of the pair. This is a non-perturbative mechanism, because it can occur even in constant fields, which are composed of photons (or other massless gauge bosons) of zero energy (consider the infinite wavelength limit of a plane wave), hence requiring an infinite number of photons to contribute to the process. It predicts a Gaussian distribution of transverse momenta of produced particles.

In high energy collisions that produce strongly interacting particles, quark-antiquark pairs will be produced. As the members of such a pair move away from each other, their color-electric dipole field forms a tube of flux lines between them known as a color string. The experimental evidence for such a flux tube has been accumulating for some time. One signature is the Regge trajectory observed in mesonic states of high angular momentum. The mass of these states grows proportional to the square root of their angular momenta [69]. This is consistent with a tube of constant energy density rotating relativistically between two low-mass endpoints (quarks) [70]. The field pattern differs from the usual electric dipole case because of the vacuum's confinement of the color fields, compressing the butterfly pattern down into a tube, by extension of the MIT bag model to quarks with large

separation [62, 63]. Much theoretical effort has been made to rigorously derive the string model directly from the QCD Lagrangian, but constraints or other features typically must be added by hand, e.g. [71]. A further limitation is that below quark separations of about 1 fm, the string picture is invalid [72]. The Schwinger mechanism is a likely candidate for the method by which new particles are produced from such strings, because the color fields contain a tremendous amount of energy and a newly minted quark-antiquark pair can completely screen the field. Yet, there is a discrepancy observed experimentally – the typical transverse momentum spectrum of final particles in such a collision is thermal (exponential), rather than Gaussian [73]. This does not make sense in relativistic e^+e^- or $p\bar{p}$ collisions where the final state only contains a few hadrons, for there are so few particles with so little interaction time that they should not thermalize.

A proposed solution to this issue is stochastic fluctuation of the strength of the color field [74]. The work in Appendix C finds such a fluctuation by assuming that the color string undergoes quantized, collective motion in only the radial direction. This should be a fairly good first approximation, as curvature in the classical string has been shown to introduce only small corrections [75]. In this work, the coordinates x and p are basically the diameter of and the field strength inside the string. If the string breaks while in the ground state of this collective oscillation, the spectrum of quarks emitted will indeed be exponential (up to a linear prefactor $1+m_\perp/T_0$, where $m_\perp$ is the transverse mass and $T_0 \approx 165$ MeV. The resulting spectrum still appears almost perfectly exponential). If the string breaks while it is in the nth excited state, on the other hand, this spectrum acquires additional polynomial prefactors of order $2n$ in $m_\perp$. As n increases from 0 the resulting spectrum quickly deviates from exponential. We take a moment here to answer a question the Appendix does not fully address: in a highly relativistic collision, why would any quantum degree of freedom be in or near its ground state?

We take the Hamiltonian per unit length of the string (C.8) and multiply it by

the length of the string (which is quickly increasing) to find the full Hamiltonian. Using this result and the commutator (C.11) it is elementary to derive the energy levels of the Hamiltonian:

$$\begin{aligned} E_n &= gL\sqrt{2B}\left(n+\frac{1}{2}\right) \\ &\simeq 300\frac{\text{MeV}}{\text{fm}}L\left(n+\frac{1}{2}\right), \end{aligned} \tag{2.2}$$

where g is the color charge (taken to be 1 here, a very conservative low estimate) and B is the color confinement pressure of the vacuum, known as the bag constant (in units where $\hbar c = 1$ it is roughly $(200\text{MeV})^4$ [62]). Even if the string is initially in a highly excited state, as the $q\bar{q}$ pair move away from each other, the length grows and the energy cost of the color field phonons ("chromonons", perhaps?) becomes quite large (at a separation of just 3 fm it is already nearly a GeV per phonon). Even though no relaxation method is included explicitly in the Hamiltonian, the string will be coupled to hadronic matter modes, and should cool rapidly to its ground state, perhaps by radiating pions, before it ultimately breaks. At the same time, the spectrum of particles produced is independent of the length of the string at the moment it breaks. Therefore, quantization of the dynamics of the color string, when combined with the Schwinger mechanism, can account for the observed spectrum in few-particle high energy collisions.

REFERENCES

[1] J. Sakurai, *Modern Quantum Mechanics* (Addison-Wesley, 1994).

[2] E. Schrödinger, Phys. Rev. **28**, 1049 (1926).

[3] W. Heisenberg, Zeitschrift fr Physik A Hadrons and Nuclei **33**, 879 (1925).

[4] A. Bohr and V. F. Weisskopf, Phys. Rev. **77**, 94 (1950).

[5] J. C. Pati and A. Salam, Phys. Rev. D **10**, 275 (1974).

[6] W. E. Lamb and R. C. Retherford, Phys. Rev. **72**, 241 (1947).

[7] P. L. Taylor and O. Heinonen, *A Quantum Approach to Condensed Matter Physics* (2002).

[8] H. Goldstein, *Classical mechanics* (1950).

[9] J. C. Maxwell, *A Treatise on Electricity and Magnetism* (1873).

[10] P. Lebedev, Ann. Phys. **6**, 433 (1901).

[11] A. Abramovici, W. E. Althouse, R. W. P. Drever, Y. Grsel, S. Kawamura, F. J. Raab, D. Shoemaker, L. Sievers, R. E. Spero, K. S. Thorne, et al., Science **256**, 325 (1992).

[12] D. Rugar, R. Budakian, H. J. Mamin, and B. W. Chui, Nature **430**, 329 (2004).

[13] G. Rempe, R. J. Thompson, H. J. Kimble, and R. Lalezari, Optics Letters **17**, 363 (1992).

[14] S. Gigan, H. R. Böhm, M. Paternostro, F. Blaser, G. Langer, J. B. Hertzberg, K. C. Schwab, D. Bäuerle, M. Aspelmeyer, and A. Zeilinger, Nature **444**, 67 (2006).

[15] M. D. LaHaye, O. Buu, B. Camarota, and K. C. Schwab, Science **304**, 74 (2004).

[16] M. Cai, O. Painter, and K. J. Vahala, Phys. Rev. Lett. **85**, 74 (2000).

[17] J. D. Thompson, B. M. Zwickl, A. M. Jayich, F. Marquardt, S. M. Girvin, and J. G. E. Harris, Nature **452**, 72 (2008).

[18] S. Lacey, H. Wang, D. H. Foster, and J. U. Nöckel, Phys. Rev. Lett. **91**, 033902 (2003).

[19] J. D. Teufel, J. W. Harlow, C. A. Regal, and K. W. Lehnert, Phys. Rev. Lett. **101**, 197203 (2008).

[20] M. Eichenfield, R. Camacho, J. Chan, K. J. Vahala, and O. Painter, Nature **459**, 550 (2009).

[21] J. D. Teufel, D. Li, M. S. Allman, K. Cicak, A. J. Sirois, J. D. Whittaker, and R. W. Simmonds, Nature **471**, 204 (2011).

[22] J. C. Sankey, C. Yang, B. M. Zwickl, A. M. Jayich, and J. G. E. Harris, Nature Physics **6**, 707 (2010).

[23] F. Khalili, S. Danilishin, H. Miao, H. Müller-Ebhardt, H. Yang, and Y. Chen, Phys. Rev. Lett. **105**, 070403 (2010).

[24] A. Schliesser, R. Rivière, G. Anetsberger, O. Arcizet, and T. J. Kippenberg, Nature Physics **4**, 415 (2008).

[25] T. Rocheleau, T. Ndukum, C. Macklin, J. B. Hertzberg, A. A. Clerk, and K. C. Schwab, Nature **463**, 72 (2010).

[26] T. J. Kippenberg and K. J. Vahala, Science **321**, 1172 (2008).

[27] F. Marquardt and S. M. Girvin, Physics **2**, 40 (2009).

[28] A. D. O'Connell, M. Hofheinz, M. Ansmann, R. C. Bialczak, M. Lenander, E. Lucero, M. Neeley, D. Sank, H. Wang, M. Weides, et al., Nature **464**, 697 (2010).

[29] W. Marshall, C. Simon, R. Penrose, and D. Bouwmeester, Phys. Rev. Lett. **91**, 130401 (2003).

[30] D. E. Chang, C. A. Regal, S. B. Papp, D. J. Wilson, J. Ye, O. Painter, H. J. Kimble, and P. Zoller, Proceedings of the National Academy of Sciences **107**, 1005 (2010).

[31] O. Romero-Isart, M. L. Juan, R. Quidant, and J. I. Cirac, New Journal of Physics **12**, 033015 (2010).

[32] S. Singh, G. A. Phelps, D. S. Goldbaum, E. M. Wright, and P. Meystre, Phys. Rev. Lett. **105**, 213602 (2010).

[33] A. Einstein, *Quantentheorie des einatomigen idealen Gases* (Wiley-VCH Verlag GmbH & Co. KGaA, 2006), pp. 237–244.

[34] S. Bose, Zeitschrift fr Physik A Hadrons and Nuclei **26**, 178 (1924).

[35] L. Landau, Physical Review **60**, 356 (1941).

[36] M. H. Anderson, J. R. Ensher, M. R. Matthews, C. E. Wieman, and E. A. Cornell, Science **269**, 198 (1995).

[37] K. B. Davis, M. O. Mewes, M. R. Andrews, N. J. van Druten, D. S. Durfee, D. M. Kurn, and W. Ketterle, Phys. Rev. Lett. **75**, 3969 (1995).

[38] C. C. Bradley, C. A. Sackett, J. J. Tollett, and R. G. Hulet, Phys. Rev. Lett. **75**, 1687 (1995).

[39] C. J. Pethick and H. Smith, *Bose-Einstein Condensation in Dilute Gases* (2001).

[40] R. Grimm, M. Weidemüller, and Y. B. Ovchinnikov, ArXiv Physics e-prints (1999), `arXiv:physics/9902072`.

[41] S. Inouye, A. P. Chikkatur, D. M. Stamper-Kurn, J. Stenger, D. E. Pritchard, and W. Ketterle, Science **285**, 571 (1999).

[42] J. Stenger, S. Inouye, D. M. Stamper-Kurn, H. Miesner, A. P. Chikkatur, and W. Ketterle, Nature **396**, 345 (1998).

[43] M. Chang, Q. Qin, W. Zhang, L. You, and M. S. Chapman, Nature Physics **1**, 111 (2005).

[44] F. Brennecke, S. Ritter, T. Donner, and T. Esslinger, Science **322**, 235 (2008).

[45] J. Garrison and R. Chiao, *Quantum Optics* (Oxford University Press, 2008).

[46] E. Brion, L. H. Pedersen, and K. Mølmer, Journal of Physics A Mathematical General **40**, 1033 (2007).

[47] J. M. Higbie, L. E. Sadler, S. Inouye, A. P. Chikkatur, S. R. Leslie, K. L. Moore, V. Savalli, and D. M. Stamper-Kurn, Phys. Rev. Lett. **95**, 050401 (2005).

[48] P. Milonni and J. Eberly, *Lasers* (Wiley, 1988).

[49] D. Steck, *Rubidium 87 d line data*, `http://steck.us/alkalidata`, (revision 2.1.4, 23 December 2010).

[50] J. von Neumann, *Mathematische Grundlagen der Quantenmechanik* (Springer, 1932).

[51] G. 't Hooft, Nuclear Physics B **72**, 461 (1974).

[52] J. Geremia, J. K. Stockton, and H. Mabuchi, Science **304**, 270 (2004).

[53] B. Kaulakys and V. Gontis, Phys. Rev. A **56**, 1131 (1997).

[54] H. Yukawa, Proc. Phys. Math. Soc. Jap. **17**, 48 (1935).

[55] M. Gell-Mann, Il Nuovo Cimento (1955-1965) **4**, 848 (1956).

[56] M. Gell-Mann, USAEC Technical Report (1961).

[57] M. Gell-Mann, Physics Letters **8**, 214 (1964).

[58] G. Zweig, CERN-TH-412 p. 80 (1964).

[59] J. Franklin, Phys. Rev. **172**, 1807 (1968).

[60] M. Gell-Mann, Phys. Rev. **125**, 1067 (1962).

[61] M. E. Peskin and D. V. Schroeder, *An Introduction to Quantum Field Theory* (Westview Press, 1995).

[62] A. Chodos, R. L. Jaffe, K. Johnson, C. B. Thorn, and V. F. Weisskopf, Phys. Rev. D **9**, 3471 (1974).

[63] K. Johnson and C. B. Thorn, Phys. Rev. D **13**, 1934 (1976).

[64] Y. Nambu and G. Jona-Lasinio, Phys. Rev. **122**, 345 (1961).

[65] A. De Rújula, H. Georgi, and S. L. Glashow, Phys. Rev. D **12**, 147 (1975).

[66] T. Schäfer and E. V. Shuryak, Rev. Mod. Phys. **70**, 323 (1998).

[67] W. Chen, D. S. Goldbaum, M. Bhattacharya, and P. Meystre, Phys. Rev. A **81**, 053833 (2010).

[68] J. Schwinger, Phys. Rev. **82**, 664 (1951).

[69] R. J. Eden, Reports on Progress in Physics **34**, 995 (1971).

[70] G. 't Hooft, Nuclear Physics B **75**, 461 (1974).

[71] Y. Nambu, Physics Letters B **80**, 372 (1979).

[72] N. Isgur and J. Paton, Physics Letters B **124**, 247 (1983), ISSN 0370-2693.

[73] M. Banner, J. L. Hamel, J. P. Pansart, A. V. Stirling, J. Teiger, H. Zaccone, J. Zsembery, G. Bassompierre, M. Croissiaux, J. Gresser, et al., Physics Letters B **41**, 547 (1972).

[74] A. Bialas, Physics Letters B **466**, 301 (1999).

[75] T. J. Allen, M. G. Olsson, and S. Veseli, Phys. Rev. D **60**, 074026 (1999).

APPENDIX A

THE ROLE OF QUANTUM FLUCTUATIONS IN THE OPTOMECHANICAL PROPERTIES OF A BOSE-EINSTEIN CONDENSATE OF A BOSE-EINSTEIN CONDENSATE IN A RING CAVITY

S. K. Steinke and P. Meystre

Submitted to Physical Review A

ABSTRACT

We analyze a detailed model of a Bose-Einstein condensate trapped in a ring optical resonator and contrast its classical and quantum properties to those of a Fabry-Pérot geometry. The inclusion of two counter-propagating light fields and three matter field modes leads to important differences between the two situations. Specifically, we identify an experimentally realizable region where the system's behavior differs strongly from that of a BEC in a Fabry-Pérot cavity, and also where quantum corrections become significant. The classical dynamics are rich, and near bifurcation points in the mean-field classical system, the quantum fluctuations have a major impact on the system's dynamics.

A.1 Introduction

In recent years, there has been an explosion of interest in optomechanical systems in which at least one degree of freedom is cooled nearly to its quantum ground state. In the top-down approach, the mechanical element (often one end-mirror of

a Fabry-Pérot cavity that is allowed to oscillate) is initially in thermal equilibrium with its surroundings and then is cooled via radiation pressure. On the other hand, in the bottom-up approach, the mechanical portion of the system typically consists of ultracold atoms trapped inside a high-Q optical resonator. The ultracold atomic system can be a thermal sample [1], a quantum-degenerate Bose-Einstein condensate (BEC) [2, 3], or even a quantum-degenerate gas of fermions [4]. In the bottom-up situation the mechanical oscillator(s) are comprised of *collective* momentum modes of the trapped gas, excited via photon recoil [5, 6, 7, 8, 9].

In the case of a high-Q Fabry-Pérot cavity the intracavity standing-wave field couples the macroscopically occupied zero-momentum component of the BEC to a symmetric superposition of the states with center-of-mass momentum $\pm 2\hbar k$ via virtual electric dipole transitions. As discussed in a previous paper [10], there are situations where a ring cavity can lead to atomic dynamics different from the standing-wave situation. This is because in contrast to a standing wave, running waves permit one in principle to extract "which way" information about the matter-wave diffraction process. As a first step toward discussing that question, the earlier work considered the difference between *classical* standing wave and counterpropagating light fields, that is, the difference in optomechanical properties of condensates trapped in, say, a Fabry-Pérot and a ring cavity. One main consequence of the presence of two counterpropagating running waves was that in addition to a symmetric "cosine" momentum side mode, it becomes possible to excite an out-of-phase "sine" mode as well. In the optomechanics analogy, this indicates that two coupled "condensate mirrors" of equal oscillation frequencies but in general different masses are driven by the intracavity field. We showed that this can result in complex multistable behaviors, including the appearance of isolated branches of solutions for appropriate choice of parameters.

The present paper builds on these results and includes two new features. At a classical (operators replaced by c-numbers) level, the evolution of the zero-

momentum mode of the condensate is now also included. Furthermore, this work also discusses the role of small quantum fluctuations in the system, particularly on the occupancy of the sine and cosine side modes. As previously discussed, together with the original condensate they form a V-system, with the upper levels – the sine and cosine modes – driven by a two-photon process involving both counterpropagating light fields. At the classical level one or the other of these modes can become a dark state, but quantum fluctuations will normally prevent these modes from becoming perfectly dark. It follows that measuring correlation functions of the optical field provides a direct means to probe the quantum properties of the matter-wave side modes. These and other aspects of the role of quantum fluctuations are examined in the following sections, which consider the situation where these fluctuations are feeble and their effect can be treated in the framework of a linearized theory.

This paper is organized as follows: Section II introduces our model of a quantum-degenerate atomic system interacting with two quantized counter-propagating field modes in a high-Q ring resonator, and casts it in a form that emphasizes the optomechanical nature of the problem. Section III derives the resulting Heisenberg-Langevin equations of motion for the system. It solves them first in steady state for the case of classical fields, recovering in a slightly different form some key results of Ref. [10], and then treats the quantum fluctuations in a linearized regime. Section IV starts by giving a formal outline of a general treatment of quantum correlations applicable in cases where many separate noise sources are present and then uses this result to analyze the different behaviors produced by the classical and quantum equations of motion for selected system parameters. Finally, Section V is a summary and conclusion.

A.2 Model

We consider a Bose-Einstein condensate of N two-state atoms with transition frequency ω_a and mass m, assumed to be at zero temperature, confined along the path

of two counterpropagating optical beams in a ring cavity of natural frequency ω_c and wave number $k_c = \omega_c/c$. These fields are driven by external lasers of intensity η_i and frequency ω_p. We assume that the atomic transition is far off-resonance from the field frequency, so that the upper electronic level can be eliminated adiabatically. Neglecting two-body collisions and in a frame rotating at the pump frequency ω_c the Hamiltonian for this system is then

$$\hat{H} = \hat{H}_{\rm opt} + \hat{H}_{\rm pump} + \hat{H}_{\rm BEC} + \hat{H}_{\rm int}, \tag{A.1}$$

where

$$\begin{aligned}
\hat{H}_{\rm opt} &= -\hbar \sum_{i=1}^{2} \Delta \hat{a}_i^\dagger \hat{a}_i, \\
\hat{H}_{\rm pump} &= i\hbar \sum_{i=1}^{2} \eta_i \hat{a}_i^\dagger - \eta_i^* \hat{a}_i, \\
\hat{H}_{\rm BEC} &= \int dx \hat{\psi}^\dagger(x) \left(-\frac{\hbar^2}{2m} \frac{d^2}{dx^2} \right) \hat{\psi}(x), \\
\hat{H}_{\rm int} &= \hbar\Omega_0 \int dx \hat{\psi}^\dagger(x) (\hat{a}_1^\dagger \hat{a}_1 + \hat{a}_2^\dagger \hat{a}_2 \\
&+ \hat{a}_2^\dagger \hat{a}_1 e^{2ikx} + \hat{a}_1^\dagger \hat{a}_2 e^{-2ikx}) \hat{\psi}(x).
\end{aligned} \tag{A.2}$$

Here $\Delta = \omega_p - \omega_c$ is the pump-cavity detuning, and

$$\Omega_0 = g_0^2/(\omega_p - \omega_a) \tag{A.3}$$

is the off-resonant vacuum Rabi frequency and g_0 is the usual (resonant) vacuum Rabi frequency.

The photon recoil associated with the virtual transitions between the lower and upper atomic electronic states results in the population of atomic center-of-mass states of momenta $2p\hbar k$, where p is an integer. For feeble intracavity fields and large detunings it is sufficient to consider the first two momentum side modes, $p = \pm 1$. It is then convenient to decompose the atomic Schrödinger field in terms of its

momentum ground state and two nearest momentum side modes in terms of the parity (rather than momentum) eigenstates

$$\hat{\psi}(x) = \sqrt{\frac{2}{L}}\left[\frac{\hat{c}_0}{\sqrt{2}} + \hat{c}_c\cos(2kx) + \hat{c}_s\sin(2kx)\right], \tag{A.4}$$

where $\hat{c}_0$, $\hat{c}_c$ and $\hat{c}_c$ are bosonic annihilation operators for the zero-momentum component and for the sine and cosine side modes of the quantum-degenerate atomic system, respectively.

To couch the problem in a more transparently optomechanical form, we further make the substitutions [1]

$$\hat{c}_0 = \sqrt{N} + \frac{\hat{X}_0 + i\hat{P}_0}{\sqrt{2}}, \tag{A.5}$$

$$\hat{a}_{1,2} = \frac{\hat{X}_{1,2} + i\hat{P}_{1,2}}{\sqrt{2}},$$

$$\hat{c}_{c,s} = \frac{\hat{X}_{c,s} + i\hat{P}_{c,s}}{\sqrt{2}}. \tag{A.6}$$

The first of these equations is indicative of the fact that we assume that the zero-momentum component of the atomic sample comprises a macroscopically populated component that we treat in mean-field theory via a classical amplitude $\sqrt{N}$, to which are superimposed quantum fluctuations resulting from the coupling to the sine and cosine side modes.

The approximate expansion (A.4) and the definitions (A.5)-(A.6) result in the alternate form of the Hamiltonian

$$\hat{H}' = \hat{H}'_{\rm opt} + \hat{H}_{\rm pump} + \hat{H}'_{\rm BEC} + \hat{H}'_{\rm int} \tag{A.7}$$

[1] Recasting the light field operators in terms of "position" and "momentum" operators has been done primarily for later analytical ease rather than as a straightforward analogy to other optomechanical problems.

where

$$\begin{aligned}
\hat{H}'_{\rm opt} &= -\hbar \sum_i \frac{\tilde{\Delta}}{2}(\hat{X}_i^2 + \hat{P}_i^2), \\
\hat{H}_{\rm pump} &= \hbar\sqrt{2}\sum_i {\rm Re}(\eta)\hat{P}_i - {\rm Im}(\eta)\hat{X}_i, \\
\hat{H}'_{\rm BEC} &= \hbar\frac{\omega_r}{2}(\hat{X}_c^2 + \hat{X}_s^2 + \hat{P}_c^2 + \hat{P}_s^2), \\
\hat{H}'_{\rm int} &= \hbar\frac{\Omega_0}{\sqrt{2}}(\hat{L}_e\hat{M}_c + \hat{L}_o\hat{M}_s),
\end{aligned} \tag{A.8}$$

and

$$\begin{aligned}
\hat{L}_e &= \hat{X}_1\hat{X}_2 + \hat{P}_1\hat{P}_2, \\
\hat{L}_o &= \hat{X}_1\hat{P}_2 - \hat{X}_2\hat{P}_1, \\
\hat{M}_I &= \sqrt{2N}\hat{X}_I + \hat{X}_0\hat{X}_I + \hat{P}_0\hat{P}_I,
\end{aligned} \tag{A.9}$$

where $I = \{c, s\}$. In Eq. (A.7) a constant term has been ignored and the energy shift of the atom-light interaction has been absorbed into the optical part of the Hamiltonian (hence the primed terms).

The operators $\hat{L}$ and $\hat{M}$ are quadratic light and matter operators, respectively, while the e and o subscripts in the light operators indicate their parity under interchange of the left- and right-moving light fields. Finally,

$$\tilde{\Delta} = \Delta - \Omega_0 N \tag{A.10}$$

is an effective detuning that accounts for the mean-field Stark shift of the condensate and

$$\omega_r = 2\hbar k^2/m \tag{A.11}$$

is the recoil frequency associated with the virtual transition.

As already discussed in Ref. [10] the presence of two counter-propagating fields in a ring resonator results in a situation that is significantly more complex than is the case for a high-Q Fabry-Pérot cavity. In particular, the optomechanical properties

of the condensate are now formally analogous to those of a system of two coupled moving mirrors. This can be seen by exploiting the fact that due to the large value of N, we can for now neglect the nonlinear terms in $\hat{M}_c$ and $\hat{M}_s$, so that

$$\hat{M}_i \simeq \sqrt{2N}\hat{X}_i, \tag{A.12}$$

and hence

$$\hat{H}'_{\rm int} \simeq \Omega_0\sqrt{N}(\hat{L}_e\hat{X}_c + \hat{L}_o\hat{X}_s). \tag{A.13}$$

Thus, rather than having a light-matter interaction proportional to the light field intensity times the position of an effective mirror we now have an interaction with two "mirrors" [11] of equal mass and effective oscillation frequency, but each of which is driven differently due to interference effects between the two counterpropagating light fields.

A.3 Equations of motion

The Heisenberg-Langevin equations of motion of the system are easily derived from the Hamiltonian (A.7), complemented by appropriate quantum noise and damping

terms. One finds readily

$$\begin{aligned}
\dot{\hat{X}}_i &= -\kappa\hat{X}_i - \tilde{\Delta}\hat{P}_i + \mathrm{Re}(\eta)\sqrt{2} \\
&+ \frac{\Omega_0}{\sqrt{2}}(\hat{M}_c\hat{P}_j + (-1)^i\hat{M}_s\hat{X}_j) + \hat{\xi}_{xi}, \\
\dot{\hat{P}}_i &= -\kappa\hat{P}_i + \tilde{\Delta}\hat{X}_i + \mathrm{Im}(\eta)\sqrt{2} \\
&- \frac{\Omega_0}{\sqrt{2}}(\hat{M}_c\hat{X}_j + (-1)^i\hat{M}_s\hat{P}_j) + \hat{\xi}_{pi}, \\
\dot{\hat{X}}_0 &= -\gamma\hat{X}_0 + \frac{\Omega_0}{\sqrt{2}}(\hat{L}_e\hat{P}_c + \hat{L}_o\hat{P}_s) + \hat{\xi}_{x0}, \\
\dot{\hat{P}}_0 &= -\gamma\hat{P}_0 - \frac{\Omega_0}{\sqrt{2}}(\hat{L}_e\hat{X}_c + \hat{L}_o\hat{X}_s) + \hat{\xi}_{p0}, \\
\dot{\hat{X}}_c &= -\gamma\hat{X}_c + \omega_r\hat{P}_c + \frac{\Omega_0}{\sqrt{2}}\hat{L}_e\hat{P}_0 + \hat{\xi}_{xc}, \\
\dot{\hat{P}}_c &= -\gamma\hat{P}_c - \omega_r\hat{X}_c - \frac{\Omega_0}{\sqrt{2}}\hat{L}_e(\sqrt{2N} + \hat{X}_0) + \hat{\xi}_{pc}, \\
\dot{\hat{X}}_s &= -\gamma\hat{X}_s + \omega_r\hat{P}_s + \frac{\Omega_0}{\sqrt{2}}\hat{L}_o\hat{P}_0 + \hat{\xi}_{xs}, \\
\dot{\hat{P}}_s &= -\gamma\hat{P}_s - \omega_r\hat{X}_s - \frac{\Omega_0}{\sqrt{2}}\hat{L}_o(\sqrt{2N} + \hat{X}_0) + \hat{\xi}_{ps}, \qquad \text{(A.14)}
\end{aligned}$$

where $i = \{1, 2\}$ and $j = 3 - i$.

The noise sources are assumed uncorrelated for the different modes of both the matter and light fields. Because the damping originates in the $\hat{a}$ and $\hat{c}$ operators, it appears in both the $\hat{X}$ and $\hat{P}$ equations of motion. In the case of the light fields, the noise and damping originate from cavity loss, vacuum noise, and laser fluctuations, while for the matter fields the primary source of noise and damping is 3-body collisions with additional nearby non-condensed atoms. In addition, the customary factors of $\sqrt{2\kappa}$ and $\sqrt{2\gamma}$ multiplying the $\hat{\xi}$'s have been absorbed into their definitions. This simplifies later results somewhat.

A.3.1 Comparison to previous results

Before further analysis is undertaken, we investigate briefly the effects of including the zero-momentum mode itself as a dynamical component of the system. We neglect noise and simply look at the existence and stability of the fixed points of Eqs. (A.14) as the various parameters are varied. The results of one such calculation are shown in Fig. A.1, revealing the dependence of the intracavity photon number $|\alpha_i|^2 = \frac{1}{2}(X_i^2 + P_i^2)$ on the detuning $\tilde{\Delta}$. When compared to Fig. 2 of Ref. [10], which uses identical parameters, we note that a quite similar bistable behavior is observed, with two degenerate stable branches the photon number can reach, as before. Which branch is reached is dependent on initial conditions and quantum fluctuations, and, when one field's intensity is given by the lower branch, the other's is given by the upper. There is one particularly interesting discrepancy when the evolution of the zero-momentum mode's occupancy is included, however. For a small range of negative detunings – around $\tilde{\Delta}/\kappa \approx -0.5$ for the present example – the bistable branches become unstable, due to a previously unseen Hopf bifurcation. Bistable periodic cycles are present, and as before, which is reached depends primarily on the initial state of the system. The amplitudes of oscillations observed in these stable cycles are quite small for the zero-momentum mode when compared to its mean value (which is of the order $\sqrt{N}$), but for the lightly occupied side modes, the amplitudes can be comparable to the mean values. This is a case where simply making the ansatz $\hat{c}_0 \to \sqrt{N}$ suppresses certain dynamical features.

In order to do a meaningful linearized quantum treatment, we attempt in this paper to avoid parameter regions where complicated multistable behavior is evident. The results of the next section will assist us in this effort. Furthermore, a broader search of the parameter space has hinted that there are also experimentally realizable regimes in which the classical dynamics goes beyond multistability and becomes chaotic. We hope to return to this topic in a later work.

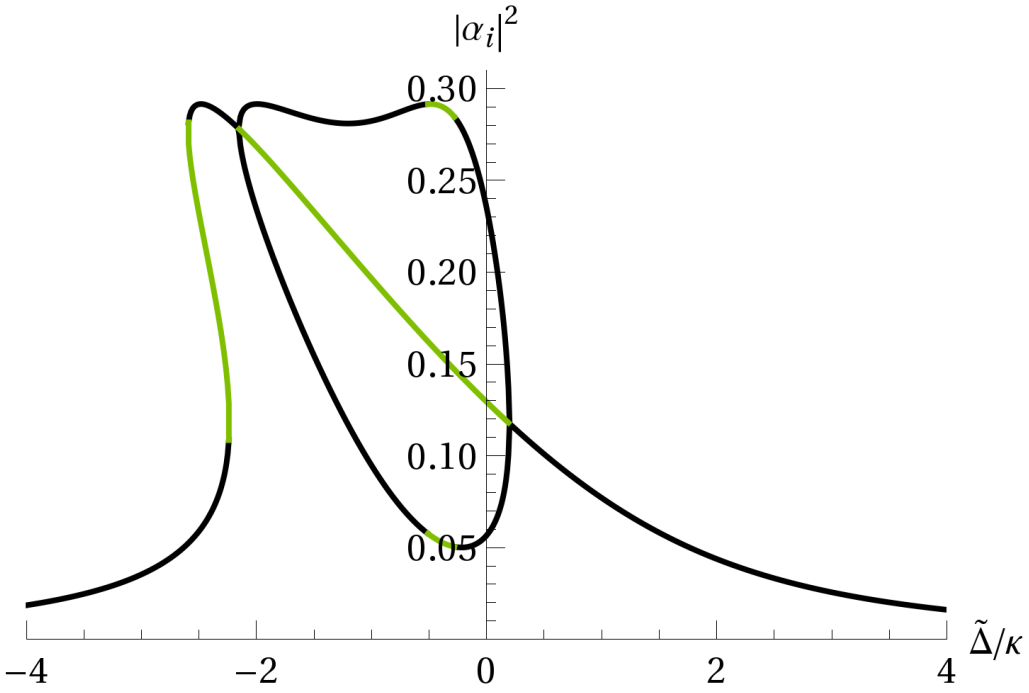

Figure A.1: Mean intracavity photon number of both modes as a function of the effective detuning $\tilde{\Delta}$. Here $\kappa = 2\pi \times 1.3$ MHz, $\gamma = 2\pi \times 1.3$ kHz, $\Omega_0 = 2\pi \times 3.1$ kHz, $\omega_r = 2\pi \times 15.2$ kHz, $N = 9000$, and $\eta_1 = \eta_2 = 0.54\kappa$. Stable solutions are indicated in black and unstable solutions are in green.

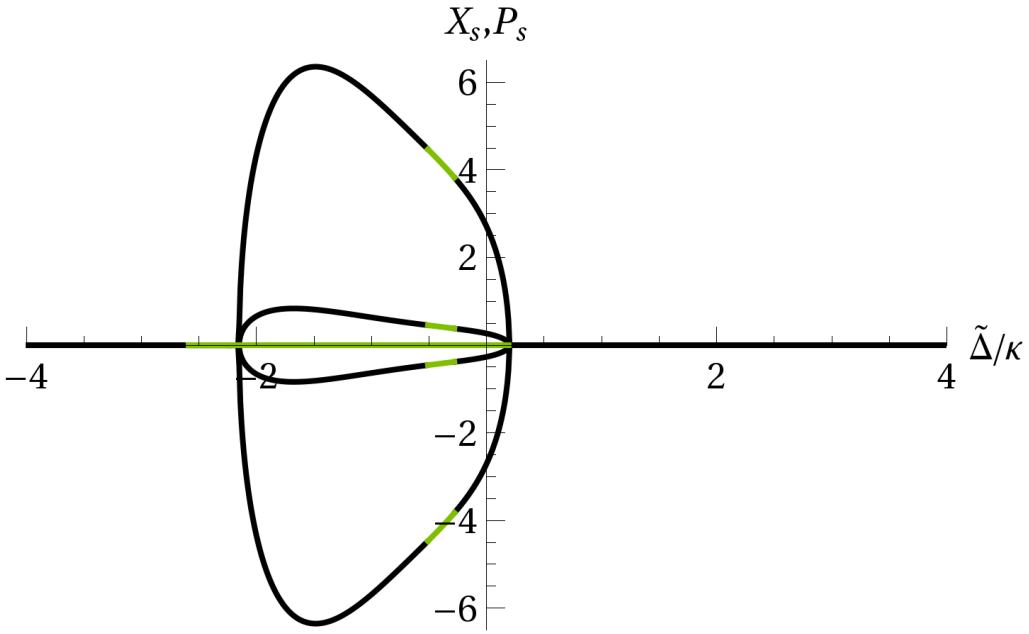

Figure A.2: Mean sine mode "position" and "momentum" as a function of $\tilde{\Delta}$. Other parameters as above. The outer magnitude branches are the position solutions and the inner the momentum. The maximum sine mode occupancy N_s reached is roughly 20.

A.3.2 Classical dark state

We now turn to a concrete example in which quantum and classical predictions differ qualitatively. Specifically, we consider the case of symmetric pumping $\eta_1 = \eta_2 = \eta$ of the counterpropagating cavity modes. We have shown previously in Ref. [10] and also below that within a classical (for the light field) and mean-field (for the atoms) theory the sine mode is a dark state, for all but relatively narrow parameter regions in which bistability and spontaneous symmetry breaking occurs (Fig. A.2). This can be seen easily by replacing all optical and matter-wave operators by classical expectation values, for instance

$$\hat{X}_0 \to \bar{X}_0, \tag{A.15}$$

where the overbar indicates the mean. Similar definitions are used for the rest of the linear operators. When a quadratic operator is written with an overbar, we refer to the products of the classical means of its constituents ($\bar{L}_e = \bar{X}_1\bar{X}_2 + \bar{P}_1\bar{P}_2$, $\bar{N}_c = (\bar{X}_c^2 + \bar{P}_c^2)/2$, etc.).

The steady-state solution in this limit is easily obtained by setting all time derivatives equal to zero. Simplifying the equations of motion for the matter field operators yields for the even and odd light field mean values the constraints

$$\begin{aligned} \bar{X}_1\bar{X}_2 + \bar{P}_1\bar{P}_2 &= 2|\alpha|^2, \\ \bar{X}_1\bar{P}_2 - \bar{X}_2\bar{P}_1 &= 0, \end{aligned} \tag{A.16}$$

where $|\alpha|^2$ is the mean number of intracavity photons in either mode. Next, we find that

$$\bar{X}_s = \bar{P}_s = 0, \tag{A.17}$$

showing that the sine side mode is indeed a dark state, as advertised. Other solutions are possible, as we see below, but we want to focus our quantum treatment on the dark sine mode. Fortunately, for many regions of parameter space, the dark sine mode is indeed the stable classical behavior of the system. A primary point of

interest for the remainder of this work is to identify conditions such that quantum corrections lead to a finite occupancy of this mode.

For completeness and to make more direct contact with Ref. [10], we also solve for the other classical steady state values.

$$\begin{aligned}
\bar{X}_0 &= -\Omega^2(\gamma^2+\Omega^2)Z, \\
\bar{P}_0 &= \gamma^2\Omega^2 Z, \\
\bar{X}_c &= -\gamma^2\omega_r\Omega Z, \\
\bar{P}_c &= -\gamma\Omega(\gamma^2+\Omega^2)Z,
\end{aligned} \tag{A.18}$$

where

$$\Omega = \Omega_0|\alpha|^2\sqrt{2} \tag{A.19}$$

is the off-resonant Rabi frequency for the intracavity photon number $|\alpha|^2$ and

$$Z = \frac{\sqrt{2N}}{(\gamma^2+\Omega^2)^2+\gamma^2\omega_r^2}. \tag{A.20}$$

We note that if we calculate $\bar{M}_c$ and $\bar{M}_s$, the quantities governing light-cosine mode and light-sine mode interaction strengths, we retrieve $\bar{X}_c\sqrt{2N}$ and 0, which are exactly the results obtained when occupancy changes in the zero-momentum mode are neglected. This shows that allowing for the evolution of the zero-momentum mode as in Eq. (A.5) versus fixing $\hat{c}_0 \to \sqrt{N}$ will only yield different behaviors for the light and side-mode fields in the spontaneously broken symmetry region of parameter space.

The remaining four equations are easily solved to give

$$\begin{aligned}
\bar{X}_{1,2} &= \frac{\kappa\mathrm{Re}(\eta)\sqrt{2}-(\tilde{\Delta}-\Omega_0\bar{X}_c\sqrt{N})\mathrm{Im}(\eta)\sqrt{2}}{\kappa^2+(\tilde{\Delta}-\Omega_0\bar{X}_c\sqrt{N})^2}, \\
\bar{P}_{1,2} &= \frac{\kappa\mathrm{Im}(\eta)\sqrt{2}+(\tilde{\Delta}-\Omega_0\bar{X}_c\sqrt{N})\mathrm{Re}(\eta)\sqrt{2}}{\kappa^2+(\tilde{\Delta}-\Omega_0\bar{X}_c\sqrt{N})^2}.
\end{aligned} \tag{A.21}$$

We may therefore eliminate $P_{1,2}$ without loss of generality (thereby requiring $\alpha = \bar{a}_{1,2}$ to be real) by appropriate selection of the real and imaginary parts (equivalently,

the phase and strength) of the pumping η, namely

$$\begin{aligned} \mathrm{Re}(\eta) &= \kappa\alpha, \\ \mathrm{Im}(\eta) &= -(\tilde{\Delta} - \Omega_0 \bar{X}_c \sqrt{N})\alpha. \end{aligned} \tag{A.22}$$

Recall from Eqs. (A.18)-(A.20) that $\bar{X}_c$ has a nontrivial implicit dependence on α (proportional to α^2 for small α and proportional to α^{-6} for large α). Once we begin the discussion of the quantum fluctuations, we will treat α as the free parameter rather than η, because it allows the quantum equations of motion to be put forth in closed form. That such a substitution is possible without requiring an inordinately large pump intensity η is shown in Fig. A.3, a plot of the relationship between the desired intracavity field α and the imaginary part of the required η.

Under the restrictions (A.22), a bifurcation diagram of the steady state solutions of the mean intracavity photon number $|\alpha_i|^2$ as a function of α are shown in Fig. A.4. In general, the system has up to six steady-state solutions, with up to two being stable. For small α, we have $\alpha_1 = \alpha_2 = \alpha$, but as α is increased the system undergoes a bifurcation, with $\alpha_1 \neq \alpha_2$. This occurs at $\alpha \approx .4$ for our parameters. This is followed by a small window with no stable solution (between about $\alpha = .45$ and .6), at which point, there is again a stable symmetric solution where the α_i are larger than might be expected. Presumably, the symmetry breaking creates something of a positive feedback loop: a few atoms are excited into the sine mode, which shifts the phase of the counterpropagating light fields, causing them to interfere with each other less effectively, thereby increasing the net number of photons in the cavity, causing more atoms to be excited. Lastly, for much larger light fields, the pumping dominates the atoms' symmetry breaking ability and the dark sine mode becomes stable again.

In addition, the character of the bifurcation diagrams as functions of $\tilde{\Delta}$ will change because of (A.22), that is, because we use a complex (rather than purely real as in Fig. A.1) η whose imaginary part is itself a linear function of $\tilde{\Delta}$. These

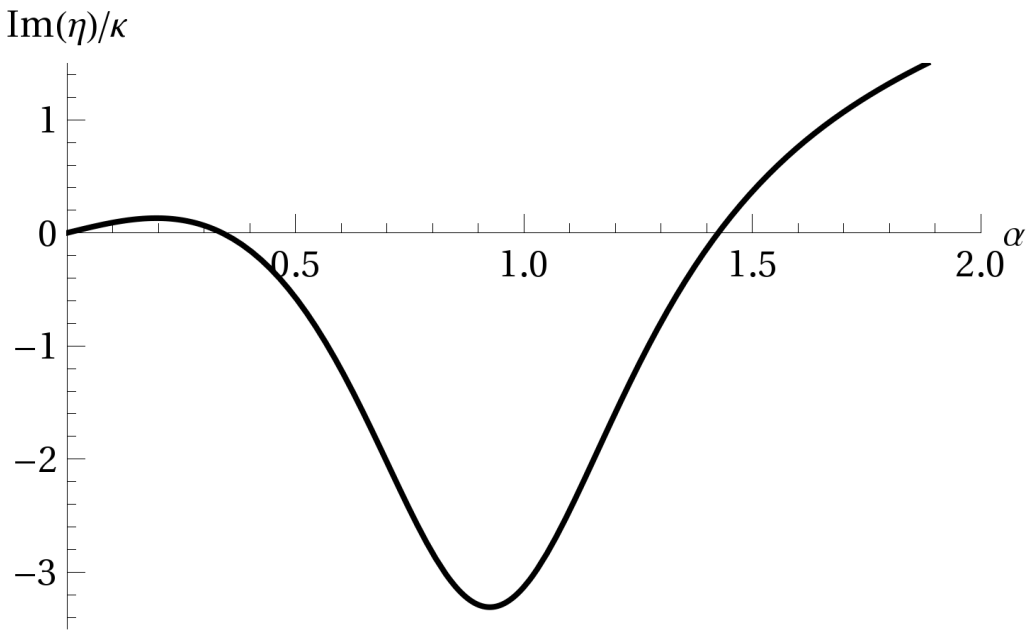

Figure A.3: Imaginary part of the pump intensity η required to produce mean intracavity field α. All parameters are as in Fig. A.1, except η itself and $\tilde{\Delta} = -1.0 \times \kappa$. Note that because $\mathrm{Re}(\eta)$ is linear in α ($\mathrm{Re}(\eta) = \kappa\alpha$), η itself is determined uniquely as a function of α.

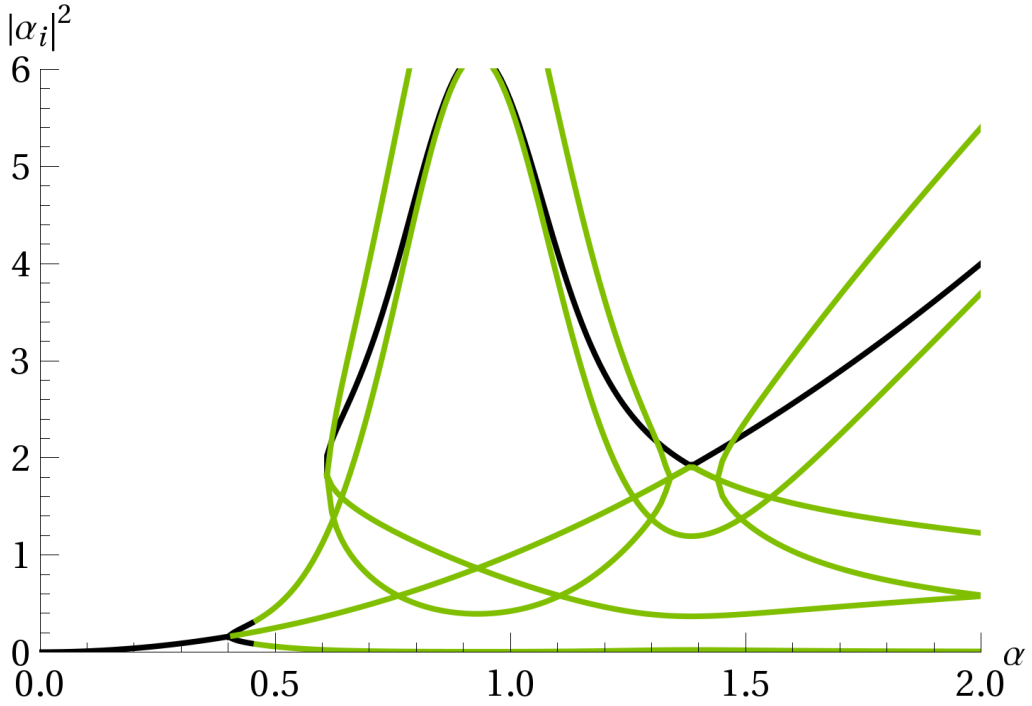

Figure A.4: Mean intracavity photon number $|\alpha_i|^2$ as a function of α. All parameters are as in Fig. A.3. The solution is not unique for sufficiently high α, (i.e. larger pumping), and also the dark sine mode solution becomes temporarily unstable (indicated in green, while stable solutions are in black).

diagrams are shown in Figs. A.5–A.7. The multistable behaviors in particular are richer than before. The dark sine mode remains stable over the entire range of $\tilde{\Delta}$ (straight black line $\alpha^2 = .0625 = .25^2$ at the bottom of Fig. A.5), yet it is augmented by an isola consisting of additional steady-state solutions with macroscopic side mode occupancies. In particular, $\bar{N}_s$ can reach approximately 250, almost 3% of the total number of atoms (see Fig. A.6). These solutions can be stable or not, and symmetric or not, depending on the detuning. We will see later that quantum fluctuations may affect tunneling between these stable solution branches. We remark that for the range of detunings where the isola has a single stable solution (between $\tilde{\Delta} \approx -2.2\kappa$ and $\tilde{\Delta} \approx -2.7\kappa$) the light mode has an additional symmetric stable solution, but the side mode still remains dark. It becomes macroscopically occupied once the symmetry of the optical isola is broken. Lastly, the imaginary part, $\bar{P}_0$, of the zero-momentum mode's creation operator can be quite large – up to half the real part (not shown; however, as $\bar{P}_0$ increases, it decreases sufficiently so the total number of atoms is always less than 9000). This result strongly suggests that the replacement of $\hat{c}_0$ by $\sqrt{N}$ is not always a safe ansatz to make; $\hat{c}_0 \to \sqrt{N}e^{i\phi}$ seems to be necessary in this case.

A.3.3 Quantum fluctuations

With these detailed results about the mean-field behavior in hand, we now include quantum fluctuations in the original equations of motion, assuming that these fluctuations remain sufficiently small that their effects may adequately be described by linearized equations of motion. We introduce the fluctuations via

$$\hat{X}_0 \to \bar{X}_0 + \hat{x}_0, \tag{A.23}$$

and so forth, and linearize the Heisenberg-Langevin equations of motion in these fluctuations. This process is justified as long as the quantum fluctuations are small compared to the classical means (or in the case of the sine mode, with its zero mean,

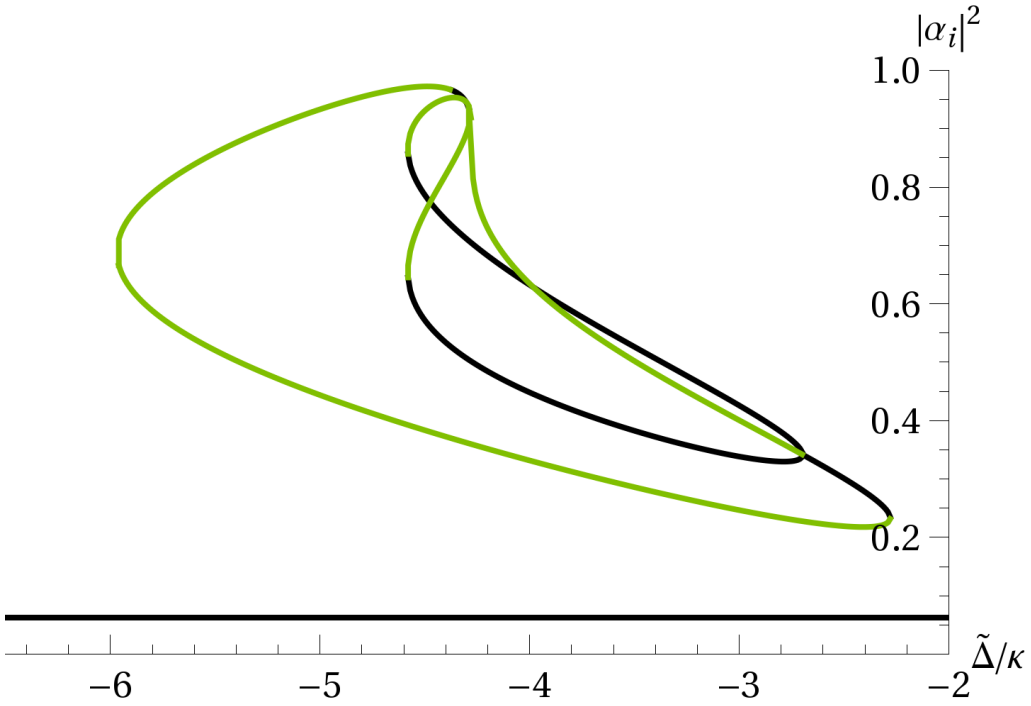

Figure A.5: Mean intracavity photon number $|\alpha_i|^2$ as a function of $\tilde{\Delta}$. All parameters are as in Fig. A.1, except rather than a fixed η, we take $\alpha = 0.25$. Stable solutions are indicated in black and unstable in green.

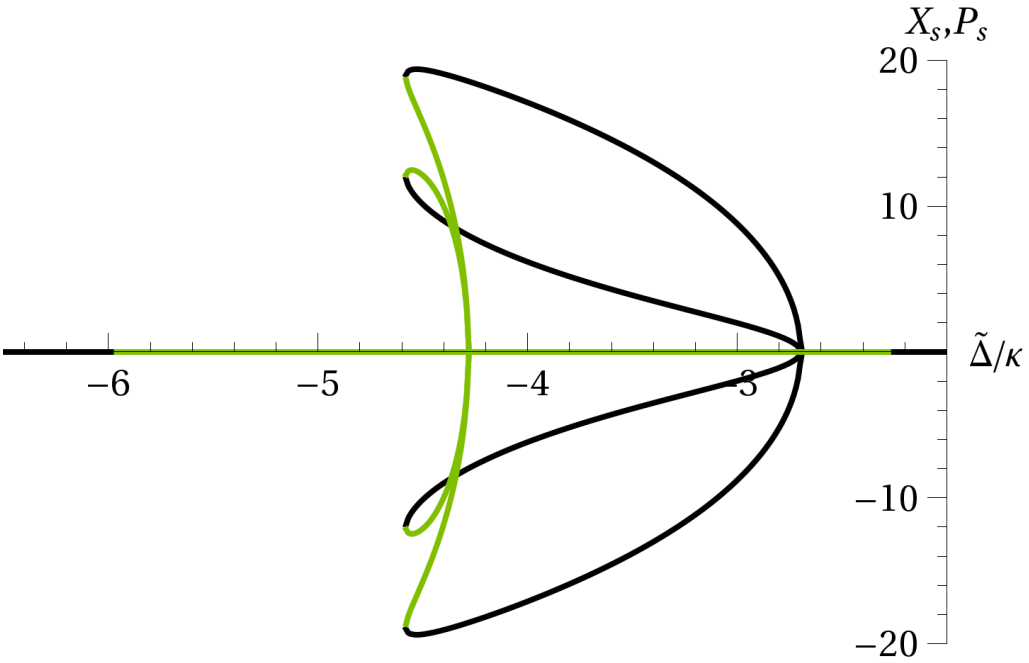

Figure A.6: Mean sine mode position and momentum as a function of $\tilde{\Delta}$. All parameters as in Fig. A.5. The outer branches are position solutions and the inner are momentum.

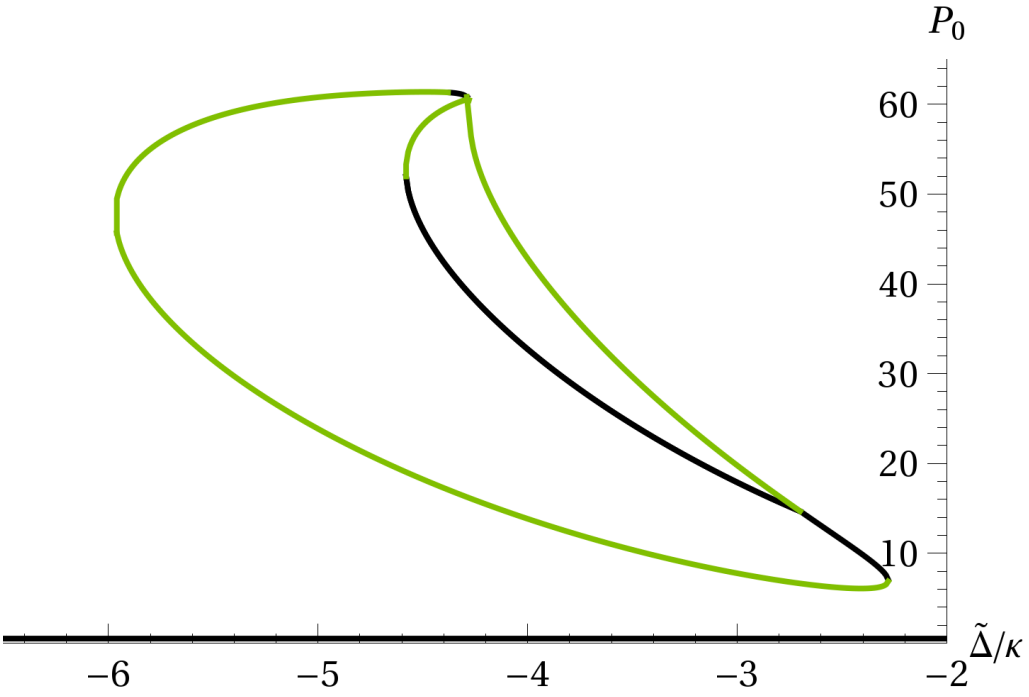

Figure A.7: Mean $\bar{P}_0$ as a function of $\tilde{\Delta}$. All parameters are as in Fig. A.5.

as long as the quadratic terms are smaller than the linear ones). But we remark again that because of the instabilities demonstrated here and in Ref. [10] this will not always be the case, so some care must be taken when selecting values for the parameters.

This linearization procedure yields the ten coupled operator equations of motion

$$\begin{aligned}
\dot{\hat{x}}_i &= -\kappa\hat{x}_i - \tilde{\Delta}\hat{p}_i + \Omega_B\hat{p}_j \\
&+ (-1)^i(\chi_0\hat{x}_s + \wp_0\hat{p}_s) + \hat{\xi}_{xi}, \\
\dot{\hat{p}}_i &= -\kappa\hat{p}_i + \tilde{\Delta}\hat{x}_i - \Omega_B\hat{x}_j - \chi_c\hat{x}_0 \\
&- \chi_0\hat{x}_c - \wp_c\hat{p}_0 - \wp_0\hat{p}_c + \hat{\xi}_{pi}, \\
\dot{\hat{x}}_0 &= -\gamma\hat{x}_0 + \Omega\hat{p}_c + \wp_c(\hat{x}_1 + \hat{x}_2) + \hat{\xi}_{x0}, \\
\dot{\hat{p}}_0 &= -\gamma\hat{p}_0 - \Omega\hat{x}_c - \chi_c(\hat{x}_1 + \hat{x}_2)) + \hat{\xi}_{p0}, \\
\dot{\hat{x}}_c &= -\gamma\hat{x}_c + \omega_r\hat{p}_c + \Omega\hat{p}_0 + \wp_0(\hat{x}_1 + \hat{x}_2) + \hat{\xi}_{xc}, \\
\dot{\hat{p}}_c &= -\gamma\hat{p}_c - \omega_r\hat{x}_c - \Omega\hat{x}_0 - \chi_0(\hat{x}_1 + \hat{x}_2)) + \hat{\xi}_{pc}, \\
\dot{\hat{x}}_s &= -\gamma\hat{x}_s + \omega_r\hat{p}_s + \wp_0(\hat{p}_2 - \hat{p}_1) + \hat{\xi}_{xs}, \\
\dot{\hat{p}}_s &= -\gamma\hat{p}_s - \omega_r\hat{x}_s - \chi_0(\hat{p}_2 - \hat{p}_1)) + \hat{\xi}_{ps},
\end{aligned} \tag{A.24}$$

where $i = \{1, 2\}$ and

$$\begin{aligned}
\Omega_B &= \frac{\Omega_0}{\sqrt{2}}\left[(\sqrt{2N} + \bar{X}_0)\bar{X}_c + \bar{P}_0\bar{P}_c\right], \\
\chi_0 &= \Omega_0\alpha(\sqrt{2N} + \bar{X}_0), \\
\chi_c &= \Omega_0\alpha\bar{X}_c, \\
\wp_0 &= \Omega_0\alpha\bar{P}_0, \\
\wp_c &= \Omega_0\alpha\bar{P}_c.
\end{aligned} \tag{A.25}$$

The first two of Eqs. (A.24) describe the fluctuations of the light field, and the last six the matter-wave fluctuations in the zero-momentum component and in the sine and cosine side modes. The terms proportional to Ω_B describe Bragg scattering between

the two counter-propagating optical fields due to the material grating formed by the zero-momentum matter wave and the cosine mode. The coupling between the light and matter operators is determined by the constants $\chi_0, \chi_c, \wp_0$ and $\wp_c$, which act as small perturbations that couple the evolution of the four light and six matter operators. Note that there is no coupling dependent on the occupancy of the sine side mode at the level of these equations of motion. The coupling coefficients involve only the classical, mean optical and matter wave fields. Thus, the coupling to the sine side mode only occurs indirectly via quantum fluctuations in the symmetric driving situation considered here.

While the exact eigenvalues and eigenvectors of the 10×10 matrix defined by these equations cannot be found explicitly in closed form, standard perturbation theory states that the eigenvalues associated to the *uncoupled* optical and matter blocks of equations, e.g. for $\chi_{0,c} = \wp_{0,c} = 0$, match those of the coupled system up to second order in the perturbation. Numerical testing confirms that the values indeed remain close. These eigenvalues are

$$\begin{aligned}
\lambda_{Lc} &= -\kappa \pm i(\tilde{\Delta} + \Omega_B), \\
\lambda_{Ls} &= -\kappa \pm i(\tilde{\Delta} - \Omega_B), \\
\lambda_{Mc} &= -\gamma \pm i\sqrt{\Omega^2 + \frac{\omega_r}{2}\left(\omega_r \pm \sqrt{4\Omega^2 + \omega_r^2}\right)}, \\
\lambda_{Ms} &= -\gamma \pm i\omega_r.
\end{aligned} \tag{A.26}$$

The reason for this nomenclature is clear when one considers the corresponding eigenvectors (normal modes of evolution). While their explicit expressions are not possible to write in closed form and are exceedingly unwieldy even when only expanded to first order in the perturbation, a qualitative inspection yields some useful information. The two pairs of eigenvalues λ_{Lc} and λ_{Ls} correspond to light-dominated evolution with a small mixture of cosine and zero-momentum state matter modes, in the first case, and of the sine matter mode, in the second case. The four λ_{Mc} eigenvalues correspond to normal modes dominated by the cosine mode and zero-

momentum mode (in unequal proportion) and coupled to the light fields. The λ_{Ms} values correspond to sine-dominated normal modes coupled to the light fields. The sine-dominated normal modes only contain a tiny contribution from the cosine mode and zero-momentum modes and vice-versa, a direct consequence of the dark-state nature of the sine mode at the classical, mean-field level. Since γ is typically the smallest parameter, as one varies the other parameters, changes in the eigenvalues that are relatively small compared to the magnitudes $|\lambda|$ can still drive the real parts of the λ_M's to be positive and thereby cause the solutions to become unstable. Because $\kappa \gg \gamma$ the optical transients die rapidly and the light fields follow adiabatically the matter wave fields, with noise- and interaction-dominated fluctuations.

The next section turns to a discussion of the correlations of various orders of the matter-wave and light modes, as well as the cross-correlations between the matter and light fields.

A.4 Quantum correlations

A.4.1 Formal development

We proceed by first presenting briefly a somewhat formal result that will prove useful in the analysis of the problem at hand, and that extends much of the machinery familiar from systems with a single damped operator to deal with multiple noise sources with distinct characteristics.

Consider a quantum system describes by a linear (or linearizable) system of coupled Heisenberg-Langevin for a vector of d operators $\hat{\vec{O}}$,

$$\frac{d}{dt}\hat{\vec{O}}(t) \;=\; \mathbf{W}\hat{\vec{O}}(t) + \hat{\vec{\xi}}(t), \tag{A.27}$$

where $\mathbf{W}$ is a $d \times d$ matrix with c-number coefficients and $\hat{\vec{\xi}}$ are purely noise operators. (We assume that any net input to the system has already been absorbed into the equations of motion.) For convenience we have merged the usual factors of $\sqrt{2\kappa}$

needed to preserve commutation relations into $\hat{\vec{\xi}}$, since they may vary for each operator.

These equations can be integrated in a straightforward fashion, yielding

$$\hat{\vec{O}}(t) = e^{\mathbf{W}t}\hat{\vec{O}}(0) + \int_0^t e^{\mathbf{W}(t-u)}\hat{\vec{\xi}}(u)du. \tag{A.28}$$

For each $i, j \leq d$, and at all times $s, t > 0$ we have

$$\langle \hat{O}_i(0)\hat{\xi}_j(t)\rangle = 0, \tag{A.29}$$

$$\langle \hat{\xi}_i(s)\hat{\xi}_j(t)\rangle = \mathbf{N}_{ij}\delta(s-t), \tag{A.30}$$

where the first condition is satisfied axiomatically, and the second one holds for white noise sources, an approximation that should be adequate for the system under study. The expectation values of the operators alone are just

$$\langle \hat{\vec{O}}(t)\rangle = e^{\mathbf{W}t}\langle \hat{\vec{O}}(0)\rangle, \tag{A.31}$$

since $\langle \hat{\vec{\xi}}(t)\rangle = 0$.

Under these conditions we can obtain the correlation matrix

$$\begin{aligned}\langle \hat{\vec{O}}(s) \otimes \hat{\vec{O}}(t)\rangle &= e^{\mathbf{W}s}\langle \hat{\vec{O}}(0) \otimes \hat{\vec{O}}(0)\rangle e^{\mathbf{W}^T t} \\ &+ \int_0^{\min(s,t)} e^{\mathbf{W}(s-u)}\mathbf{N}e^{\mathbf{W}^T(t-u)}du,\end{aligned} \tag{A.32}$$

which lets us compute all quadratic correlations at all times, e.g. $\langle \hat{x}_1(s)\hat{p}_c(t)\rangle$.

For the rest of the paper, we shall work in the long-time limit, in which the transient behavior of the operators has decayed to 0. In physical terms, for the model in question, this corresponds to times $t \gg 1/\gamma$, which are experimentally accessible for long-lived BECs. In this limit, the initial values have decayed to irrelevance, and the correlations are simply

$$\langle \hat{\vec{O}}(s) \otimes \hat{\vec{O}}(t)\rangle = \int_0^{\min(s,t)} e^{\mathbf{W}(s-u)}\mathbf{N}e^{\mathbf{W}^T(t-u)}du. \tag{A.33}$$

This is the central result of this section. For a Gaussian process we can easily determine higher order correlations as well: all three-operator correlators are 0, and the four operator correlators are given by

$$\begin{aligned}\langle\hat{\vec{O}}(s)\otimes\hat{\vec{O}}(t)\otimes\hat{\vec{O}}(u)\otimes\hat{\vec{O}}(v)\rangle = & \\ & \langle\hat{\vec{O}}(s)\otimes\hat{\vec{O}}(t)\rangle\otimes\langle\hat{\vec{O}}(u)\otimes\hat{\vec{O}}(v)\rangle \\ + & \langle\hat{\vec{O}}(s)\otimes\hat{\vec{O}}(u)\rangle\otimes\langle\hat{\vec{O}}(t)\otimes\hat{\vec{O}}(v)\rangle \\ + & \langle\hat{\vec{O}}(s)\otimes\hat{\vec{O}}(v)\rangle\otimes\langle\hat{\vec{O}}(t)\otimes\hat{\vec{O}}(u)\rangle. \end{aligned} \tag{A.34}$$

Now, we apply this technique to our model. The operators $\hat{\vec{O}}$ are the $\hat{x}$'s and $\hat{p}$'s, with the coefficients $\mathbf{W}$ given by (A.24). Lastly, we determine the $\xi_{x,p}$, and hence, $\mathbf{N}$ from the following relations:

$$\langle\hat{\xi}_{ai}(s)\hat{\xi}^{\dagger}_{ai}(t)\rangle = 2\kappa\delta(s-t)(N^{th}_i+1), \tag{A.35}$$

$$\langle\hat{\xi}^{\dagger}_{ai}(s)\hat{\xi}_{ai}(t)\rangle = 2\kappa\delta(s-t)N^{th}_i, \tag{A.36}$$

$$\langle\hat{\xi}_{cI}(s)\hat{\xi}^{\dagger}_{cI}(t)\rangle = 2\gamma\delta(s-t)(N^{th}_I+1), \tag{A.37}$$

$$\langle\hat{\xi}^{\dagger}_{cI}(s)\hat{\xi}_{cI}(t)\rangle = 2\gamma\delta(s-t)N^{th}_I, \tag{A.38}$$

where $i = \{1,2\}$, $I = \{0,c,s\}$, the N^{th}'s are thermal noise occupancies of the baths near the characteristic frequencies of the system as given by Bose-Einstein statistics, and all other quadratic noise correlations are 0. The noise matrix $\mathbf{N}$ for the position and momentum operators thus has the form of 5 2×2 block matrices, each with $2N^{th}+1$ for the on-diagonal entries and $\pm i$ for the off-diagonal entries with all 4 entries multiplied by γ or κ as appropriate. Because we are dealing with optical photons and a BEC at a temperature of at most a few μK, going forward we take all $N_{th}\to 0$, or, equivalently, we take the bath temperatures to be 0. We find that typically increasing the N_{th}'s just adds directly to the occupancy of the corresponding fields.

A.4.2 Second-order correlations and quantum occupancies

Working with a set of parameters that are a combination of those in Figs. A.4 – A.7 and with $\tilde{\Delta} = -1. \times \kappa$, $\alpha = 0.25$, we explore a few results of the cross operator correlations before looking at the quantum-fluctuation-augmented occupancy of the side modes. Further calculations not presented here have shown that the results attained at these particular parameter values are fairly typical of the monostable regime in which we are interested.

As expected, the fluctuations in the zero-momentum and cosine modes are virtually uncorrelated with those of the sine mode, $\langle(\hat{x},\hat{p})_{0,c}(\hat{x},\hat{p})_s\rangle \approx 0$, but are slightly correlated with each other (e.g. $\langle\hat{x}_0\hat{x}_c\rangle \approx 0.022$ – for comparison, $\bar{X}_0\bar{X}_c \approx 0.11$, so the classical mean-field correlation is a more significant contribution). By far the largest correlation between distinct matter and/or light fields, however, is the one that confirms our intuition, namely, the sine mode's fluctuations are very strongly correlated to those of the light field (e.g. $\langle\hat{x}_i\hat{x}_s\rangle \approx (-1)^i 0.32, i = 1, 2$). This shows that, indeed, the occupation of the sine side mode is driven by the fluctuations in the light fields.

We also consider the occupancy of the side modes as functions of the most easily tunable parameters $\tilde{\Delta}$ and α. Keeping in mind that all single operator expectation values such as $\langle\hat{x}_i\rangle$ decay to 0, we have

$$\langle\hat{X}_i^2\rangle \;=\; \bar{X}_i^2 + \langle\hat{x}_i^2\rangle, \tag{A.39}$$

etc. When evaluating these quantities we must be careful to avoid those regions in parameter space where the dark sine mode steady state solution is unstable, in particular, we need $\alpha < 0.4$. The results are shown in Figs. A.8 and A.9. In the former, we see a noticeable occupation of the sine mode before the classical bifurcation. This may be sufficient to shift the bifurcation point to a lower value of α. This possibility is corroborated by the observed shift to the left in the plot of $\langle N_c\rangle$ versus $\bar{N}_c$; that is, when quantum fluctuations are included, the cosine mode behaves

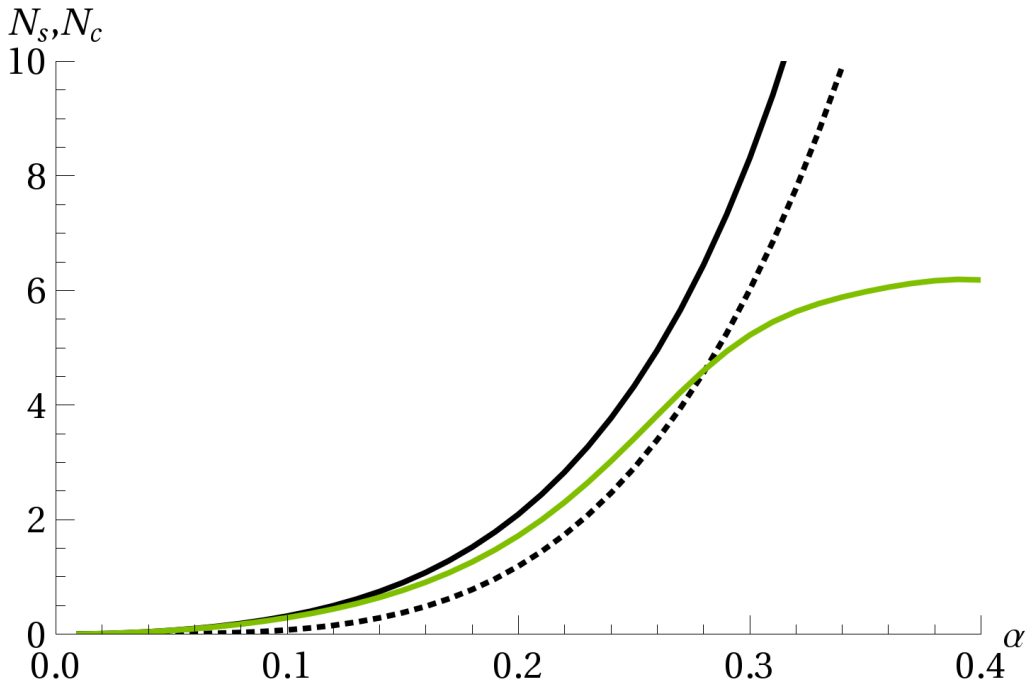

Figure A.8: Side mode occupancies $\langle N_c \rangle, \langle N_s \rangle$ as functions of α. Parameters as in Fig. A.3. The cosine mode has a larger occupancy and is in black; the sine mode is in green. For reference, the classical mean $\bar{N}_c$ is plotted (dashed line) as well.

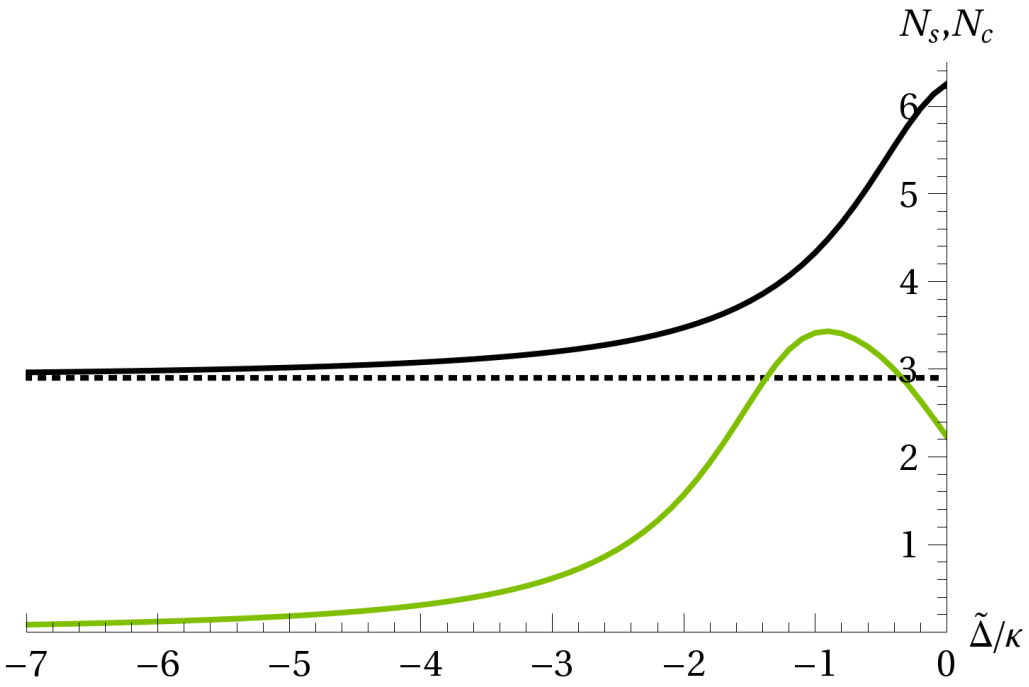

Figure A.9: Side mode occupancies $\langle N_c \rangle, \langle N_s \rangle$ as functions of $\tilde{\Delta}$. Parameters as in Fig. A.5, but the range of $\tilde{\Delta}$ has been extended slightly. The cosine mode has a larger occupancy and is in black; the sine mode is in green. For reference, the classical mean $\bar{N}_c$ is plotted (dashed line) as well. $\bar{X}_c$ and $\bar{P}_c$ do not depend on $\tilde{\Delta}$ so it is constant.

as if α were slightly larger. On the other hand, a somewhat different behavior is seen in the latter plot. As $\tilde{\Delta}$ decreases from 0 and approaches the bifurcation seen above in Figs. A.5–A.7, the sine mode initially starts to increase in occupancy, but then its (and the cosine mode's) quantum fluctuations are suppressed as $|\tilde{\Delta}|$ increases further. Nevertheless, as we see below, the variance in the sine mode's occupation is so large that the quantum fluctuations may still influence the character of the system's behavior in the case $-2.5\kappa \lesssim \tilde{\Delta} \lesssim -1.0\kappa$.

A.4.3 Variance in side mode occupancy

Because the system is coupled to a zero temperature bath, we compare the variance

$$\sigma_I^2 \;=\; \langle \hat{N}_I^2 \rangle - \langle \hat{N}_I \rangle^2 \tag{A.40}$$

to that of a bosonic system in thermal equilibrium, in which case

$$\sigma_{I,\mathrm{TH}}^2 \;=\; \langle \hat{N}_I \rangle^2 + \langle \hat{N}_I \rangle, \tag{A.41}$$

specifically taking the ratio of (A.40) to (A.41). A value less than one indicates sub-thermal statistics, as would be the case when there is a significant classical mean and/or quantum fluctuations are suppressed. On the other hand, a ratio greater than one indicates significant fluctuations and a matter or light field driven out of thermal equilibrium. These ratios are computed and plotted in Figs. A.10 and A.11. In the former, for weak mean intracavity light field α, both modes' statistics are thermal in nature. As the applied field is increased, the sine mode is perturbed to slightly higher variance, whereas the cosine mode at first exhibits less than thermal variance, as the classical mean field contribution grows. However, the quantum fluctuations then take over and its variance grows quickly as α approaches the bifurcation at a value of roughly 0.4. We should however take this result with a grain of salt since it is at this point that the quantum fluctuation contribution to $\langle \hat{N}_c \rangle$ exceeds the mean contribution $\bar{N}_c$, thus endangering the validity of the linearized treatment.

Still, it should of course be expected that increased fluctuations in the cosine mode significantly alter the existence and stability of steady state solutions in this critical region.

In the second of these figures we plot the variances as a function of the effective detuning $\tilde{\Delta}$. In this case, except for detunings very near 0, the cosine mode is almost completely classical, as is the sine mode for sufficiently negative values of $\tilde{\Delta}$. This implies that, if a zero-momentum condensate is formed and allowed to evolve for the parameters given and a $\tilde{\Delta}$ of less than -2.5κ or so, and if it reaches the dark sine mode steady state, it is quite likely to remain there indefinitely, as quantum fluctuations are strongly suppressed. But for less negative values of $\tilde{\Delta}$, the sine mode fluctuations are significant. It may be possible that these fluctuations "anticipate" the classical bifurcation nearby in parameter space, or even that they allow the new stable solutions to appear for larger values of the detuning than they would otherwise. To test this would likely require simulation of the full nonlinear quantum evolution of the system.

A.5 Discussion and Conclusions

By analyzing a detailed model including two counter-propagating light fields and three matter fields, we are able to find a region in parameter space, with experimentally accessible values, where the system's behavior differs significantly from that of a BEC in a Fabry-Pérot cavity, and also where quantum corrections become significant. The classical dynamics are rich, and near bifurcation points in the mean-field classical system, the quantum fluctuations also have intriguing properties. They appear strong enough to shift or perturb the dynamical bifurcation points.

This system's dynamics are richer than the typical optomechanical system, and they may be exploited in the future to investigate numerous non-classical effects. For instance, because of the strong cross-correlation between the light's and the sine mode's fluctuations, it should be possible, by measuring the output light fields, to

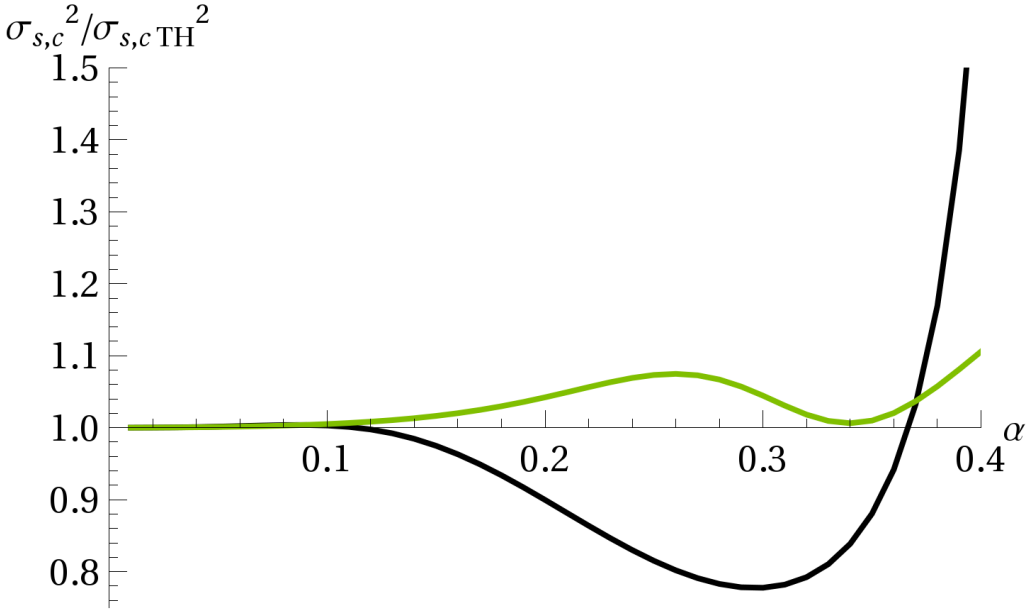

Figure A.10: Variance of side mode occupancy compared to thermal variance as functions of α. Parameters as Fig. A.8. Cosine mode is in black and sine mode in green.

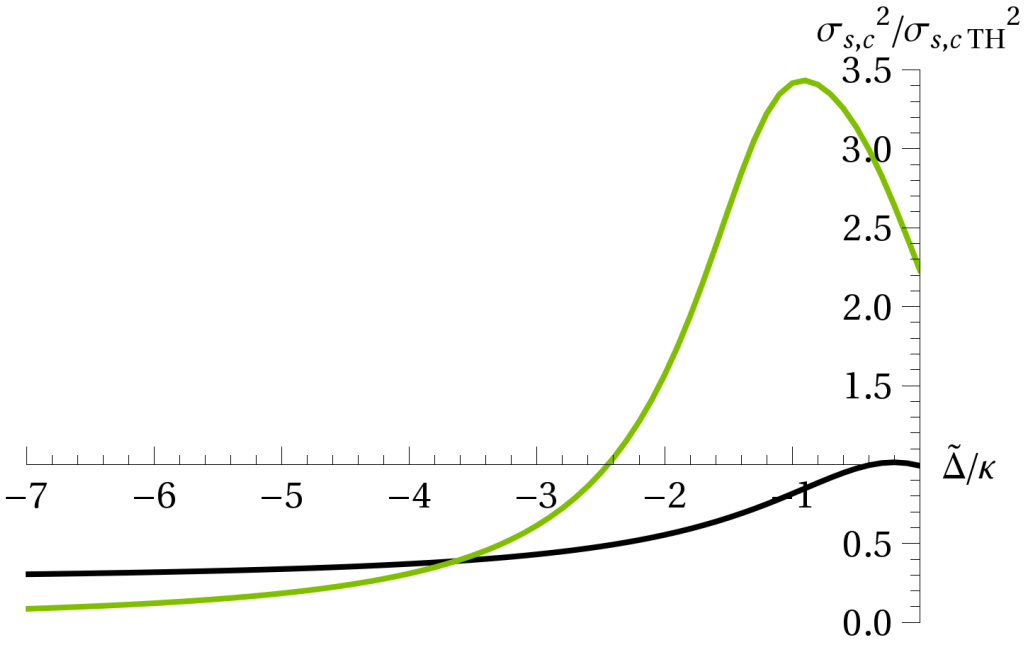

Figure A.11: Variance of side mode occupancy compared to thermal variance as functions of $\tilde{\Delta}$. Parameters as Fig. A.9. Cosine mode is in black and sine mode in green.

monitor the sine mode as it tunnels between different possible steady state branches. This would contrast with the tunneling suppression seen in, e.g., Ref. [12], and it relies on the optically driven fluctuations in the matter fields. Also, for significantly larger condensates, with $N \approx 10^6$, apparently chaotic classical dynamics are observed. It may be that this behavior persists even with the minimal ($N^{th} = 0$) kicks given by the noise operators $\hat{\xi}$. To explore these possibilities, further work will be needed in the form of a full nonlinear quantum treatment.

Acknowledgements – This work is supported by the US National Science Foundation, the DARPA ORCHID program through a grant from AFOSR, and the US Army Research Office, US Office of Naval Research.

REFERENCES

[1] K. W. Murch, K. L. Moore, S. Gupta, and D. M. Stamper-Kurn, Nat. Phys. **4**, 561 (2008).

[2] F. Brennecke, S. Ritter, T. Donner, and T. Esslinger, Science **322**, 235 (2008).

[3] S. Ritter, F. Brennecke, K. Baumann, T. Donner, C. Guerlin, and T. Esslinger, Appl. Phys. B **95**, 213 (2009).

[4] R. Kanamoto and P. Meystre, Phys. Rev. Let. **104**, 063601 (2010).

[5] D. Nagy, P. Domokos, A. Vukics, and H. Ritsch, Euro. Phys. J. D **55**, 695 (2009).

[6] J. M. Zhang, F. C. Cui, D. L. Zhou, and W. M. Liu, Phys. Rev. A **79**, 033401 (2009).

[7] W. Chen, K. Zhang, D. S. Goldbaum, M. Bhattacharya, and P. Meystre, Phys. Rev. A **80**, 011801 (2009).

[8] D. S. Goldbaum, K. Zhange, and P. Meystre, Arxiv:0911.3234 (2009).

[9] A. B. Bhattacherjee, Phys. Rev. A **80**, 043607 (2009).

[10] W. Chen, D. S. Goldbaum, M. Bhattacharya, and P. Meystre, Phys. Rev. A **81**, 053833 (2010).

[11] M. Bhattacharya and P. Meystre, Phys. Rev. A **78**, 041801(R) (2008).

[12] G. J. Milburn, J. Corney, E. M. Wright, and D. F. Walls, Phys Rev. A **55**, 4318 (1997).

APPENDIX B

QUANTIFYING QUANTUM MEASUREMENT BACK-ACTION ON A MACROSCOPIC OBJECT: BEC MAGNETOMETRY ON MECHANICAL OSCILLATORS

S. K. Steinke[1], S. Singh[1], M. E. Tasgin[1],P. Meystre[1],K. C. Schwab[2], M. Vengalattore[3]

[1]B2 Institute, Department of Physics and College of Optical Sciences The University of Arizona, Tucson, Arizona, 85721, [2]Applied Physics, California Institute of Technology, MC 128-95, Pasadena, California 91125, [3]Laboratory of Atomic and Solid State Physics, Cornell University, Ithaca, New York, 14853

To be submitted to Physical Review A

ABSTRACT

We study theoretically the dynamics of a a hybrid optomechanical system consisting of a macroscopic mechanical membrane magnetically coupled to a spinor Bose-Einstein condensate via a nanomagnet attached at the membrane center. We demonstrate that his coupling permits to indirectly monitor the center-of-mass position of the membrane via a non-destructive measurement of the Larmor precession frequency of the condensed atoms. This measurement induces a significant back-action on the membrane motion, which we quantify for the cases of thermal and coherent initial states of the membrane. We discuss the possibility of measuring that quantum back-action via repeated measurements, and show that it can be for

observable experimental parameters. We also investigate the potential to generate non-classical of the membrane, in particular Schrödinger cat states, via such repeated measurements.

B.1 Introduction

While the theoretical foundations of Quantum Measurement Theory were already laid down in the early days of quantum mechanics by Bohr, Schrödinger, Heisenberg, von Neumann and others, quantitative studies are a relatively recent development that is now driving significant advances in quantum information science and quantum metrology, with major progress originally driven both by the desire to test Bell's inequalities on the one hand, and by the quest for gravitational wave detection on the other. A common aspect of these and related studies is the need to quantify, control, and possibly exploit the quantum back-action of one or a series of measurements on a quantum mechanical system.

An important development in this context is the rapid progress witnessed by cavity optomechanics, which makes it increasingly realistic to consider the use of mechanical systems operating in the quantum regime to make precise and accurate measurements of feeble forces and fields. In many cases, these measurements amount to the detection of exceedingly small displacements. In this context, *hybrid systems* consisting of coupled atomic (or molecular) and nanomechanical systems may prove particularly useful. The robust and scalable infrastructure provided by NEMS/MEMS devices coupled with the high precision measurement capability of quantum gases [10, 11, 12] makes them an attractive combination for sensitive force measurements, as well as for a quantitative study of dissipation and decoherence processes at the quantum-classical interface. There are ongoing experimental [3, 4] and theoretical [5, 6, 7, 8, 9] efforts toward coupling mechanical systems to atomic ensembles.

The system that we consider consists of a mechanical membrane magnetically

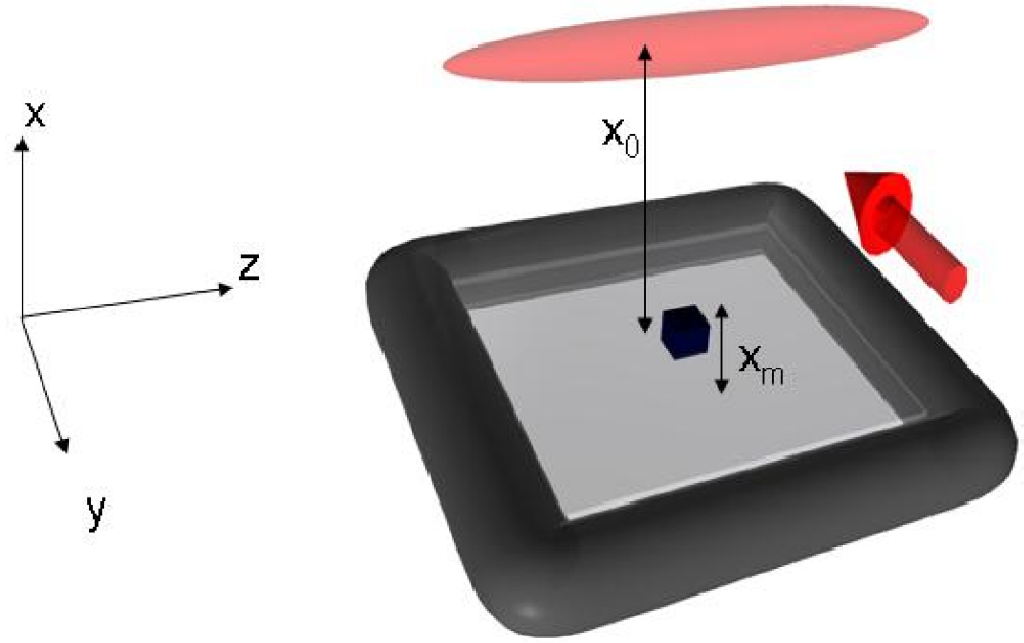

Figure B.1: Proposed experimental setup for back-action detection, involving a magnetic particle located at the center of a vibrating membrane and polarized along the z-axis. This setup produces a spatially inhomogeneous magnetic field that is detected by the BEC. The BEC's long axis is along the z-direction, the probe light (red arrow) is along y, and the membrane oscillations are along the x-axis.

coupled to a spinor Bose-Einstein condensate, an arrangement somewhat similar to a system previously considered in Refs. [5, 8]. The magnetic coupling, generated via a nano-magnet anchored on the membrane, allows for an indirect determination of the center-of-mass position of the membrane through a non-destructive measurement of the Larmor precession frequency of the condensed atoms. This in turn can be achieved via a phase contrast imaging technique, as described in Ref. [10]. Since the Larmor frequency is proportional to the local magnetic field – which is modulated by the motion of the magnetic domain attached to the oscillating membrane – it provides a measure of the membrane motion. This technique promises to be much more precise than a measurement of trap loss such as recently demonstrated in Ref. [4]. The measurement of the BEC spin induces in turn a back-action on the membrane, modifying in general both its position and its momentum. One main goal of this paper is to quantify this back-action and to determine the feasibility of measuring it directly, thereby providing a way to directly observe quantum back-action on a macroscopic object. So far such quantum effects have only been observed for measurements on a BEC [14]. We also discuss the possibility of exploiting this back-action to achieve the quantum control of the membrane position, for instance to prepare its center-of-mass in a squeezed state or a Schrödinger cat state.

This paper is organized as follows; Section II introduces the system under consideration and derives a model Hamiltonian that describes the magnetic coupling of the membrane to the condensate. Section III discusses the indirect measurement of the membrane center-of-mass position via the Larmor precession of the condensate, assuming that the membrane is initially in a thermal state. In particular, we present the post-measurement Wigner function of the membrane and interpret its main features in terms of a back-action parameter. Section IV then turns to the case of repeated measurements on this system, illustrating how a sequence of measurements provides a direct signature of the back-action. Section V discusses the possibility of producing highly non-classical states of the membrane, considering

specifically the case where it is initially in a coherent state. We show that repeated measurements typically leave the membrane in a non-classical state characterized by a non-positive Wigner distribution. Finally, Section V is a summary and outlook. Some technical details of the calculations are relegated to appendices.

B.2 Model

As already mentioned in the introduction, the hybrid system under consideration consists of a micromechanical membrane whose center-of-mass is oscillating, perhaps under the influence of a weak force. Our goal is to develop and analyze a quantum measurement scheme that permits us to characterize the center-of-mass motion of that membrane.

The scheme that we envisage involves integrating this membrane into a hybrid system whose other component is an elongated spinor Bose-Einstein condensate with long axis z, see Fig. 1. The condensate is subjected to a static magnetic field B_0 along the quantization axis z. The membrane is magnetically coupled to the condensate via a magnetic domain anchored at the center of the membrane. Since the resulting magnetic field at the location of the condensate depends on its distance from the dipole, a measurement of the changes in Larmor frequency of the spinor condensate – e.g. via a non-destructive phase contrast imaging technique – provides direct information on the membrane motion.

We assume for simplicity that the magnetic domain is a point dipole located at the origin and polarized along the z-axis, $\mu_{\mathbf{m}} = \mu_m \hat{\mathbf{z}}$. The magnetic field due to that dipole is

$$\mathbf{B}(\mathbf{r}) = \frac{\mu_0}{4\pi} \frac{1}{r^3} \left(3(\mu_{\mathbf{m}} \cdot \hat{\mathbf{r}})\hat{\mathbf{r}} - \mu_{\mathbf{m}}\right). \tag{B.1}$$

The small spatial variation of the resulting magnetic field along the long axis of the condensate results in a variation of its Larmor precession frequency. As we show in the following, this dependence permits us to characterize the expectation value of

center-of-mass mode of oscillation of the membrane.

The Zeeman interaction between the atoms in the condensate and the total magnetic field $\mathbf{B}_0 + \mathbf{B}(\mathbf{r})$ is described by the Hamiltonian

$$\begin{aligned} H &= -\mu_{\mathbf{a}} \cdot (\mathbf{B}_0 + \mathbf{B}(\mathbf{r})) \\ &= \mu_B g_F \left(F_x B_x + F_y B_y + F_z (B_0 + B_z)\right), \end{aligned} \tag{B.2}$$

where F_i is the i^{th} component of the spin-1 operator. As a result of the spatial dependence of the magnetic field, atoms at different positions along the long axis of the condensate precess at different frequencies and dephase over a period of time. It is this z-dependent phase difference that is picked up in phase contrast imaging.

We note that the transverse dependence of the magnetic field also results in an inhomogeneous broadening of the Larmor frequency. The effects of this broadening can be minimized, the more elongated along z and tightly confined in the transverse directions the condensate. In the following we consider for simplicity a condensate that is almost two-dimensional and confined to a region close to $y = 0$, so that $B_y \approx 0$ and $F_y B_y \simeq 0$. Furthermore, close to $z = 0$, i.e. for the fraction of the BEC directly above the dipole, the magnetic field $\mathbf{B}(\mathbf{r})$ is predominantly in the z- direction provided that x_0, the equilibrium distance between the BEC and the membrane, is much greater than the relevant coordinates y and z. In that case we can ignore the effects of B_x and B_y altogether.

As shown in detail in Appendix A, for small displacements x_m of the membrane compared to x_0 the magnetic coupling Hamiltonian (B.2) reduces then to

$$V = \mu_B g_F F_z \left[B_0 + \frac{\mu_0 \mu_m}{4\pi x_0^4} \left(-x_0 + 3x_m\right)\right]. \tag{B.3}$$

The first and the second term of this expression are independent of time, while the third term, proportional to x_m, varies sinusoidally in time. We exploit this property by rewriting the magnetic Hamiltonian as

$$V = \mu_B g_F F_z \left(B_c + B_v' x_m\right), \tag{B.4}$$

where

$$B'_v = \frac{3\mu_o\mu_m}{4\pi x_0^4}, \tag{B.5}$$

see Appendix A. From here on we drop the subscript in membrane displacement, $x_m \rightarrow x$ for compactness. The total system Hamiltonian of the hybrid BEC-membrane system is then

$$H = H_m + H'_{\mathrm{BEC}} + V. \tag{B.6}$$

Here

$$H_m = p^2/2m + m\omega_m^2 x^2/2$$

is the membrane Hamiltonian and

$$H'_{\mathrm{BEC}} = H_{0,\mathrm{BEC}} + \mu_B g_F F_z B_c,$$

where $H_{0,\mathrm{BEC}}$ is the spin-independent part of the atomic Hamiltonian. Describing the condensate as a collection of N non-interacting spin-1 atoms at zero temperature, and assuming that the atoms are experiencing a constant magnetic field over the detector area of interest, perhaps one or a few CCD camera pixels, we can then express the interaction Hamiltonian as

$$V = N\mu_B g_F F_z (B_c + B'_v x). \tag{B.7}$$

This simplifies the total Hamiltonian to

$$H = \frac{p^2}{2m} + \frac{1}{2} m\omega_m^2 \left(x + AF_z\right)^2 + \left\{\hbar\Omega_{L0} F_z - \hbar\delta\Omega F_z^2\right\} \tag{B.8}$$

where

$$A = \mu_B g_F N B'_v / m\omega^2, \tag{B.9}$$

which we call the *back-action parameter* in anticipation of the following sections, and

$$\delta\Omega = m\omega_m^2 A^2/2\hbar. \tag{B.10}$$

B.3 Spin measurement

The measurement proceeds in the following way: at time $t = 0$ a $\pi/2$ pulse is applied to the condensate, preparing all atoms in $|F_x = 1\rangle$ state. Following that preparation stage, the atomic spins precess about the z-axis until a later time t_1 when the atoms are brought in interaction with a σ_+ polarized optical field propagating along the y-axis, see Fig. 1. As a result of that interaction the optical field acquires a phase shift proportional to the y-component of the atomic spin [10], thereby measuring the Larmor precession resulting from the magnetic field $B_c + B'_v x$. Briefly, this frequency can be inferred from the accumulated phase shift resulting from the different (Clebsch-Gordon) coupling coefficients of the field to the three spin states under consideration. Additional measurements can be performed at later time intervals $t_i, i = 2, 3, \ldots$. A key point here is that the light field does not perturb the membrane, and realizes therefore a 'non-destructive' measurement of the BEC state in the F_y basis.

Equation (B.8) already gives a clear indication of the back-action of the measuring apparatus – the condensate – on the membrane. As a result of their coupling the membrane Hamiltonian is modified from being a harmonic oscillator centered at the origin to one that is shifted by the quantity AF_z, indicating that the back-action depends on the outcome of a specific measurement. Here, we give an explicit description of the measurement process by evaluating the pre– and post-measurement density operator of the membrane, and the corresponding Wigner function.

B.3.1 Density operator

We assume that the membrane and the condensate are initially uncorrelated,

$$\rho = \rho_m(0) \otimes \rho_{\mathrm{BEC}}(0)$$

and denote the initial density matrix elements of the BEC as $\rho^0_{\alpha,\beta}$, where $\rho_{\alpha,\beta} = \langle\alpha|\rho_{\mathrm{BEC}}|\beta\rangle$, and α, β are the various spin states, $\alpha, \beta = \{0, \pm 1\}$. We also assume for

now that the membrane center-of-mass is initially in a thermal state at temperature T. With

$$\eta = \hbar\omega_m/2k_BT,$$

its density matrix elements in position space are then

$$\begin{aligned}\rho_m(x_f, x_i, t=0) &= \langle x_f|\rho_m|x_i\rangle = \sqrt{\frac{m\omega_m}{\pi\hbar}\tanh\eta} \\ &\times \exp\left[-\frac{m\omega_m}{4\hbar}\left((x_f+x_i)^2\tanh\eta + (x_f-x_i)^2\coth\eta\right)\right] \quad \text{(B.11)}\end{aligned}$$

For $t > 0$ the spin components of the condensate undergo a Larmor precession about the z-axis. Since $[H_{\rm BEC}, H_m+V] = 0$, we can use the Baker-Hausdorff relation to re-express the propagator $U(t) = \exp(-iHt/\hbar)$ as

$$U(t) = e^{-itH_{\rm BEC}/\hbar}e^{-it(H_m+V)/\hbar}.$$

This allows to find the evolution of the system density matrix in a straightforward way. After an interaction time t_1, this evolution results in the matrix elements of the density operator of the membrane + condensate system to become

$$\begin{aligned}&\langle\alpha, x_f|\rho(t)|\beta, x_i\rangle = \rho^0_{\alpha\beta}\exp[-i\Omega_{L0}(\alpha-\beta)t_1 + i\delta\Omega_L(\alpha^2-\beta^2)t_1]\sqrt{\frac{m\omega_m}{\pi\hbar}\tanh\eta} \\ &\times\exp\left[-\frac{m\omega_m}{4\hbar}\left\{\left(x_f + x_i + (\alpha+\beta)A(1-\cos\omega_m t_1)\right)^2\tanh\eta\right.\right. \\ &+\left(x_f - x_i + (\alpha-\beta)A(1-\cos\omega_m t_1)\right)^2\coth\eta \\ &\left.\left.+4iA\sin\omega_m t_1(\alpha x_f - \beta x_i) + 2iA^2(\alpha^2-\beta^2)\sin\omega_m t_1(2-\cos\omega_m t_1)\right\}\right]. \quad \text{(B.12)}\end{aligned}$$

That is, the interaction of the membrane with the BEC displaces its center-of-mass motion in both position and momentum by amounts that depend explicitly on the spin components α and β, as well as on the back-action parameter A.

B.3.2 Single measurement

As already discussed, a measurement of F_y is carried out at time t_1 by propagating through the BEC a (classical) σ_+-polarized light beam sufficiently far detuned from

any atomic resonance that it does not destroy its state. The post-measurement density matrix of the membrane depends on the measurement outcome, and is given by

$$\langle x_f|\rho_m|x_i\rangle_{Fy,\gamma} = \frac{1}{P(F_{y,\gamma})}\sum_{\alpha,\beta} F^*_{(y,\gamma),\alpha}\rho_{\rm sys}F_{(y,\gamma),\beta}. \tag{B.13}$$

Here γ is the outcome of the F_y measurement, $\gamma = \{0, \pm 1\}$, $P(F_{y,\gamma})$ is the probability of that outcome, and $F_{(y,\gamma),\beta}$ is the β component of the $F_y = \gamma$ eigenstate.

B.3.3 Phase Space Representation

The effect of the measurement on the state of the membrane can be visualized particularly clearly in terms of its Wigner distribution function

$$W(x,p) = \frac{1}{2\pi\hbar}\int d\xi e^{-ip\xi/\hbar}\langle x+\xi/2|\rho|x-\xi/2\rangle \tag{B.14}$$

For a harmonic oscillator in a thermal state, we have

$$W(x,p,t=0) = \frac{1}{\pi\hbar}\tanh\eta\exp\left[-\frac{m\omega_m}{\hbar}\left(x^2+\left(\frac{p}{m\omega_m}\right)^2\right)\tanh\eta\right] \tag{B.15}$$

an expression that should be contrasted to the post-measurement Wigner function, which is found to be

$$\begin{aligned}
W(x,p,t_1) &= \frac{1}{\pi\hbar}\tanh\eta\frac{1}{P(F_{y,\gamma})}\sum_{\alpha,\beta}F^*_{y,\gamma\alpha}F_{y,\gamma\beta}\rho^0_{\alpha\beta} \qquad \text{(B.16)}\\
&\times\exp[-i\Omega_{L0}(\alpha-\beta)t_1 + i\delta\Omega_L(\alpha^2-\beta^2)t_1]\\
&\times\exp\left\{-\frac{m\omega_m}{\hbar}\left[\left(x+\frac{A}{2}(\alpha+\beta)(1-\cos(\omega_m t_1)\right)\right)^2\right.\\
&\left.+\left(\frac{p}{m\omega_m}+\frac{A}{2}(\alpha+\beta)\sin(\omega_m t_1)\right)^2\right]\tanh\eta\\
&+iA(\alpha-\beta)\left(x\sin(\omega_m t_1)-\frac{p}{m\omega_m}(1-\cos(\omega_m t_1))+\frac{A}{2}(\alpha+\beta)\sin(\omega_m t_1)\right)\Bigg\}.
\end{aligned}$$

At time t_1 the first line of Eq. (B.16) simply describes the imposition of a global phase in $W(x,p)$, with a value depending on the measurement outcome. More

interesting are the last two lines in that expression: The second line describes a shift and stretch of the initial gaussian distribution, with a value dependent on the temperature and back-action parameter A. When this is the dominant term, the measurement results in an oblate gaussian Wigner function moving around the phase space at the membrane frequency. The measurement dependent position shift is derived in the next subsection.

The third line in $W(x, p, t_1)$ results in oscillations of the Wigner function. These are due to the fact that the initial state of the BEC, $|F_x = 1\rangle$, is not an eigenstate of the interaction Hamiltonian (proportional to F_z). So, one can think of the condensate as experiencing three interaction Hamiltonians simultaneously, one for each of its spin components, and it is the interference between them that leads to the oscillations. We remark that the oscillations in the Wigner function can be seen as long as

$$\frac{A}{x_{zp}} \gtrsim \sqrt{\tanh \eta} \tag{B.17}$$

where $x_{zp} = \sqrt{\hbar/2m\omega_m}$.

B.3.4 Back-action

To illustrate the effect of backaction, we assume the following membrane parameters for the remainder of the paper (unless stated otherwise): $\omega_m = 2\pi 10^6$ rad/s, $m = 10^{-17}$ kg, $\mu_m = 10^{-12}\mathrm{A} \cdot \mathrm{m}^2$, and an initial temperature of 4K. The static external magnetic field is $B_0 = 0.1$ Gauss, and the condensate is $x_0 = 5 \times 10^{-6}$ m away from the membrane, resulting in a single-atom back-action parameter $A_{\mathrm{sa}} = 2.25 \times 10^{-18}$ m. We assume that $N = 10^4$ atoms experience the same magnetic field in the detection region, yielding then an effective back-action parameter of $A_0 = NA_{\mathrm{sa}} = 2.25 \times 10^{-14}$m (for comparison, $A_0 = 0.246 x_{zp}$). Fig. B.2 shows the resulting post-measurement Wigner Function for this A_0 (figure c), and for the backaction parameter being $0.1A_0$ (figure b), and $0.01A_0$ (figure a)., assuming that a measurement of F_y with result 1 was made after an interaction time of $t_1 = \pi/\omega_m$.

As alluded to by Eq. (B.17), in order to observe the oscillations in the post-measurement Wigner function, we can either increase the temperature or increase A. However, increasing the temperature leads to dissipation and decoherence losses that are ignored in the present analysis, but result of course in a fast thermalization and associated smoothing of $W(x, p.$ A more promising approach will be to increase A (Eq. (B.9)), either by increasing the number of atoms in the effective detection zone, or by increasing B_v' via a decrease of x_0. Since B_v' scales as $1/x_0^4$, this may be the easiest way to reach the regime of observable Wigner function oscillations. Note however that for decreasing x_0 the simplified interaction Hamiltonian (B.7) becomes less accurate as the components of the magnetic field along x and y become more important. Both decoherence effects and corrections to the Hamiltonian (B.7) will be discussed in future work.

An additional point of concern is that the BEC does not act as a good position sensor for high A, as can be seen in Fig B.2. The act of measurement on the BEC creates a significant change in the phase-space distribution of the membrane that would invalidate any information gained about the position. However, as we show in Section V, a high value of A is beneficial for preparing the membrane in highly non-classical states via repeated measurements. As with all schemes for state preparation involving repeated measurements, its not very efficient for highly excited initial states like the one considered in Fig. B.2 considering – at 4 K, and for the membrane parameters of this example, the mean phonon occupation number is 5.2×10^5.

The expectation value of the center-of-mass position $\langle x \rangle$ of a membrane in thermal equilibrium is zero, and its variance is

$$\sigma^2(x) = \langle x^2 \rangle - \langle x \rangle^2 = \langle x^2 \rangle = \frac{\hbar}{2m\omega_m} \coth \eta. \tag{B.18}$$

Immediately following the measurement, the membrane is no longer in thermal equilibrium, and $\langle x \rangle \neq 0$ in general. For large back-action parameters the oscillations

on $W(x,p)$ become quite significant, but on the other hand, these oscillations also indicate that in that regime the BEC is a poor position sensor, since its coupling to the membrane significantly perturbs the outcome of subsequent measurements. To investigate the efficiency of our setup as a position sensor, it is therefore appropriate to consider the limit of small A_0. Consider for concreteness the specific example where the outcome of the spin measurement is $F_y = 1$. Ignoring then terms of order A^2, and for $t_1 = \pi/\Omega_{L0}$, we find

$$\langle x \rangle = -\frac{A}{2} \sin \omega_m \pi/\Omega_{L0} \coth \eta, \tag{B.19}$$

with $\langle x^2 \rangle$ remaining constant to lowest order in A. We then have

$$\sigma^2(x)_{\rm pm} = \frac{\hbar}{2m\omega_m} \coth \eta - \frac{A^2}{4} \sin^2 (\omega_m \pi/\Omega_{L0}) \coth^2 \eta \tag{B.20}$$

where the subscript "pm" indicates post-measurement. The minimum back-action occurs for $\eta \to \infty$, or $T \to 0$. It also vanishes when the membrane frequency is an integer multiple of Larmor precession frequency,

$$\omega_m = n\Omega_{L0}, \tag{B.21}$$

where n in an integer, in which case it is possible to carry out stroboscopic QND measurements of the membrane position.

B.4 Successive Measurements

The previous discussion hints at the possibility of carrying out stroboscopic QND measurements of the membrane, but in general, successive measurements result in an accumulation of back-action effects. At the same time, they offer the potential for the coherent control of the center-of-mass motion of the membrane. To address such situations, we now consider the effect of a succession of measurements on the state of the membrane. The similarity between Eqs. (B.11) and (B.12) suggests that it should be possible to find a closed form for the density matrix of the composite

system after an arbitrary number of measurements on the BEC. Indeed, this is the case and such a form is presented below.

B.4.1 Analytical results

We first consider the situation where the membrane is initially in a thermal state, and assume that the interaction between the membrane and the BEC, (initially prepared in the $F_x = 1$ state, is turned on at time $t_0 = 0$. After time t_1, a first measurement is performed on the spin of the BEC. The light-BEC interaction time $t_{\rm meas}$ required to carry out that measurement is taken to be negligible compared to the other characteristic times of the system – in practice $t_{\rm meas}$ is about 10 percent of the Larmor period. The direct effect of the measurement is only on the BEC, and can be formally described by a Krauss operator $M^{(1)}$ that depends explicitly on the outcome of the measurement. Following that first measurement the system the system evolves unitarily for an additional time t_2, becoming re-entangled. A second measurement is then performed, acting on the BEC with an operator $M^{(2)}$, and this process is repeated n times.

Immediately following the nth measurement, the elements of the BEC-membrane system's density matrix are given by (see Appendix B)

$$\begin{aligned}
\langle \alpha, x_f|\rho(t)|\beta, x_i\rangle &= \sum_{\alpha_1,\ldots\alpha_n;\beta_1,\ldots\beta_n} M^{(n)}_{\alpha\ \alpha_n} M^{(n-1)}_{\alpha_n\alpha_{n-1}} \ldots M^{(1)}_{\alpha_2\alpha_1} \rho_{\alpha_1\beta_1} M^{(1)\dagger}_{\beta_1\beta_2} \ldots M^{(n-1)\dagger}_{\beta_{n-1}\beta_n} M^{(n)\dagger}_{\beta_n\beta} \\
\times\ & \exp\left[-i\sum_{i=1}^{n} t_i\{\Omega_{L0}(\alpha_i-\beta_i) - \delta\Omega_L(\alpha_i^2-\beta_i^2)\}\right] \sqrt{\frac{m\omega_m}{\pi\hbar}\tanh\eta} \\
\times\ & \exp\Big[-\frac{m\omega_m}{4\hbar}\big\{(x_f + X[\alpha]A + x_i + X[\beta]A)^2 \tanh\eta \\
+\ & (x_f + X[\alpha]A - x_i - X[\beta]A)^2 \coth\eta \\
+\ & 4iA(P[\alpha](x_f + X[\alpha]A) - P[\beta](x_i + X[\beta]A)) + 2iA^2(\phi[\alpha] - \phi[\beta])\big\}\Big] \quad \text{(B.22)}
\end{aligned}$$

where

$$M^{(i)}_{\sigma\tau} = \langle\sigma|M^{(i)}|\tau\rangle, \tag{B.23}$$

$$X[\sigma] = \sigma_n - \sum_{i=1}^{n} (\sigma_i - \sigma_{i-1}) \cos T_{i,n}, \tag{B.24}$$

$$P[\sigma] = \sum_{i=1}^{n} (\sigma_i - \sigma_{i-1}) \sin T_{i,n}, \tag{B.25}$$

$$\begin{aligned}\phi[\sigma] &= \sum_{i=1}^{n} (\sigma_i - \sigma_{i-1})^2 \sin T_{i,n} \cos T_{i,n} \\ &+ 2 \sum_{i=1}^{n-1} \sum_{j=i+1}^{n} (\sigma_i - \sigma_{i-1})(\sigma_j - \sigma_{j-1}) \sin T_{j,n} \cos T_{i,n},\end{aligned} \tag{B.26}$$

and

$$T_{i,j} = \omega_m \sum_{k=i}^{j} t_k \quad \text{if} \quad i \leq j \quad \text{and} \quad = 0 \quad \text{otherwise.} \tag{B.27}$$

The sums on α_i and β_i run over $\{-1, 0, +1\}$, and in Eqs. (B.24) – (B.26) we have $\alpha_0 = \beta_0 = 0$ wherever they appear. To be clear, in the equations above, the times t_i are the spacing between measurements rather than the times themselves. Also, care should be taken as X, P, and ϕ are functions of the spin indices and thus must be recomputed for each term in the sum. Note also that the density matrix (B.22) is unnormalized. Its trace is equal to the probability of the particular sequence of measurement outcomes described by the specific set of operators $\{M^{(i)}\}$ occurring in it.

A few remarks are in order before turning to a discussion of numerical results: First, the density matrix of the membrane can be obtained from Eq. (B.22) by a partial trace. It is the sum of many different contributions from various shifted (in position and momentum) thermal ensembles. A (numerical) computation problem does arise, though, as calculating the density matrix for n measurements requires summing over 9^n terms. In our numerics we will thus be restricted to few-measurement scenarios.

The timing of the measurements is also very important to the BEC functioning as a detector. In one extreme case, if the measurements are made exactly at the natural frequency of the membrane, the interaction will be completely masked, except for the tiny second-order effect of $\delta\Omega_L$. This again supports the claim that position is very nearly a stroboscopic QND variable.

The structures of Eqs. (B.22) and (B.24)-(B.26) also indicate that the results of the earliest measurements continue to be as important as those of later measurements. This is because in the absence of dissipation, there is no attenuation of the information gained nor of the back-action induced by the measurements. Including the effects of thermal dissipation reduces and eventually erases this memory effect.

The Wigner function (B.14) of the membrane after n measurements can be derived from (B.22) and is found to be

$$\begin{aligned} W(x,p) = & \frac{1}{\mathrm{tr}(\rho_{sys}(t))} \sum_{\gamma,\alpha_1,\ldots,\beta_n} M^{(n)}_{\gamma\ \alpha_n} M^{(n-1)}_{\alpha_n\alpha_{n-1}} \ldots M^{(1)}_{\alpha_2\alpha_1} \rho_{\alpha_1\beta_1} M^{(1)\dagger}_{\beta_1\beta_2} \ldots M^{(n-1)\dagger}_{\beta_{n-1}\beta_n} M^{(n)\dagger}_{\beta_n\gamma} \\ \times \quad & \exp\left(-i\sum_{i=1}^{n} t_i(\Omega_{L0}(\alpha_i-\beta_i) - \delta\Omega_L(\alpha_i^2-\beta_i^2))\right) \frac{1}{\pi\hbar}\tanh\eta \\ \times \quad & \exp\left[-\frac{m\omega_m}{\hbar}\left\{\left(\left(x+\frac{A}{2}(X[\alpha]+X[\beta])\right)^2\right.\right. \\ + \quad & \left.\left.\left(\frac{p}{m\omega_m}+\frac{A}{2}(P[\alpha]+P[\beta])\right)^2\right)\tanh\eta + iA(P[\alpha]-P[\beta]) \right. \\ \times \quad & \left.\left(x+\frac{A}{2}(X[\alpha]+X[\beta])\right) - iA(X[\alpha]-X[\beta])\frac{p}{m\omega_m} + i\frac{A^2}{2}(\phi[\alpha]-\phi[\beta])\right\}\Bigg], \end{aligned} \tag{B.28}$$

a form that clearly illustrates the shift in position and momentum of the various terms in the sum.

B.4.2 Numerical results

One simple way to detect the effect of quantum back-action on the state of the membrane is to consider a sequence of 2 measurements carried out in succession at

times t_1 and t_2, and to compare the outcome of the last measurement to the outcome of a measurement at that same time t_2, but skipping the first measurement at t_1. As a concrete example, we consider, for the parameters of the previous section, the following two scenarios:

1. F_y is measured once, at $t_2 = \pi/\omega_m$ (i.e., half the oscillator period);
2. F_y is measured first at $t_1 = \pi/2\omega_m$ and then at $t_2 = \pi/\omega_m$.

By simply calculating the trace of Eq. (B.22) for the 3 possible operators $M^{(1)}$'s in scenario 1 we obtain the probabilities

$$\begin{aligned} P(F_y = \pm 1) &= 0.375 \\ P(F_y = 0) &= 0.25 \end{aligned} \tag{B.29}$$

In the second scenario 9 traces need to be evaluated instead of just 3. Summing then the three terms corresponding to the same final value of F_y, so as to obtain the total probability of obtaining a particular value for the second measurement, we find

$$\begin{aligned} P(F_y = \pm 1) &= 0.344 \\ P(F_y = 0) &= 0.312 \end{aligned} \tag{B.30}$$

The simple example shows that back-action of the intermediate measurement should be readily observable, since it changes the probability for the three possible outcomes of the measurements at t_2 by a significant amount, of the order of several percent.

A slightly more complete look into the effects of intermediate measurements is provided by the Wigner functions shown in Figures B.2 and B.3. In Fig. B.2, we show a series of plots for the case of a single measurement at $t = \pi/\omega_m$, for different values of A ($0.01A_0, 0.1A_0$, and A_0, respectively). In Fig. B.3 we increase the number of measurements from 1 to 2. The time of the final measurement is the same as in Fig. B.2, π/ω_m, but an intermediate measurement is made at time

$t_1 = \pi/2\omega_m$. The outcome of the final spin measurement is again $F_y = 1$, but, for the sake of direct comparison with Fig. B.2, we average over all possible results of the intermediate measurement. This is equivalent to an experiment in which the outcomes of the intermediate measurement are discarded or ignored. As expected, the Wigner functions where an intermediate measurement are noticeably different than the one lacking an intermediate measurement, hinting at a simple way to characterize the impact of quantum back-action on the membrane dynamics.

B.5 Initial Coherent State

We now turn to the situation where the center-of-mass state of the membrane is a coherent state. an initial condition that can be prepared by driving the membrane with a classical force. The main result of this section is to demonstrate that after n measurements, the center-of-mass of membrane is split into a superposition of up to 3^n discrete coherent states, hinting at the possibility to generate a macrsocopic Schrödinger cat.

B.5.1 Evolution of the Coherent State

The assumption that the membrane is initially in a coherent state allows us to eschew the density matrix formalism for the moment, and the initial state of the composite system is given by

$$|\Psi(0)\rangle \quad = \quad D(a_0 + ib_0)|0_{\rm mem}\rangle \otimes \sum_\alpha c_\alpha |\alpha\rangle \tag{B.31}$$

where $\sum_\alpha |c_\alpha|^2 = 1$ and

$$D(u) = \exp(u\hat{a}^\dagger - u^*\hat{a})$$

is the displacement operator for the center-of-mass state of the membrane.

Following a procedure similar to that for the initially thermal membrane, we

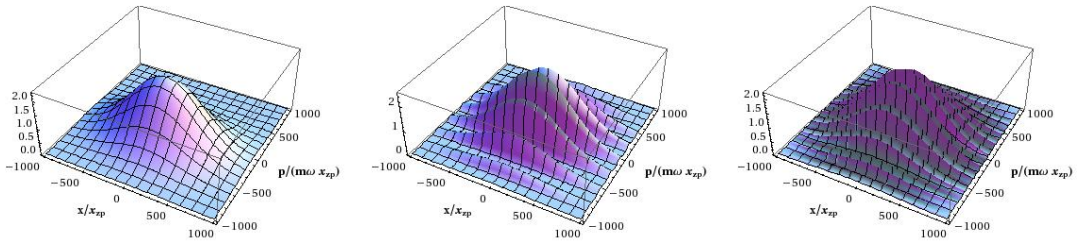

a. $A = 0.01A_0$ **b.** $A = 0.1A_0$ **c.** $A = A_0$

Figure B.2: Wigner distribution function of the membrane after one measurement giving the result $F_y = 1$, for several values of the back-action parameter: (a) $A = 0.01A_0$: (b) $A = 0.1A_0$ and (c) $A = A_0$, with $A_0 = 0.246\sqrt{\hbar/2m\omega_m}$. The evolution time is $t = \pi/\omega_m$ in all three cases. The Wigner function has been multiplied by 10^6 to make the axes legible.

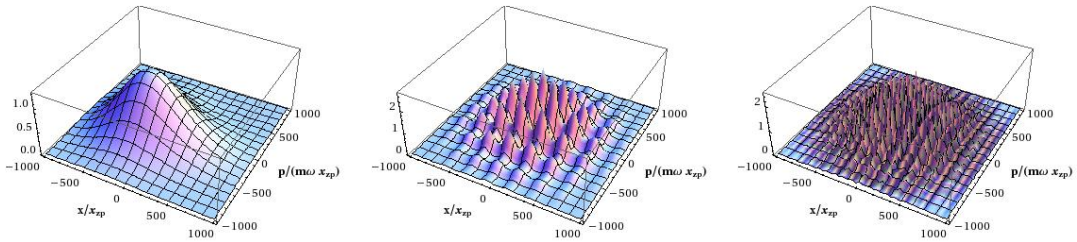

a. $A = 0.01A_0$ **b.** $A = 0.1A_0$ **c.** $A = A_0$

Figure B.3: Wigner distribution function of the membrane in the case of two measurements: the final spin measurement, at time π/ω_m, yields the outcome $F_y = 1$. As in Fig.(B.2), the three Wigner functions are plotted for increasing values of the back-action parameter, A, and the final Wigner functions are averaged over all possible outcomes of the intermediate measurement.

arrive at the final state for the hybrid membrane-BEC system

$$|\Psi(0)\rangle = \sum_{\alpha,\alpha_1,\ldots,\alpha_n} M^{(n)}_{\alpha\ \alpha_n} \ldots M^{(1)}_{\alpha_2\alpha_1} c_{\alpha_1} \exp\left(-i\sum_{i=1}^{n} t_i \left(\Omega_{L0}\alpha_i - \delta\Omega_L\alpha_i^2 + \frac{\omega_m}{2}\right) - i\frac{A\Theta[\alpha]}{2x_{zp}}\right) \times \quad D(a[\alpha] + ib[\alpha])|0_{mem}\rangle \otimes |\alpha\rangle \tag{B.32}$$

with

$$a[\sigma] = a_0 \cos T_{1,n} + b_0 \sin T_{1,n} - \frac{A}{2x_{zp}} X[\sigma], \tag{B.33}$$

$$b[\sigma] = b_0 \cos T_{1,n} - a_0 \sin T_{1,n} - \frac{A}{2x_{zp}} P[\sigma], \tag{B.34}$$

$$\Theta[\sigma] = \sum_{i=1}^{n} \sigma_i \big[a_0(\sin T_{1,i} - \sin T_{1,i-1}) - b_0(\cos T_{1,i} - \cos T_{1,i-1}) + \frac{A}{2x_{zp}} \sum_{j=1}^{i} (\sigma_j - \sigma_{j-1})(\sin T_{j,i} - \sin T_{j,i-1})\big], \tag{B.35}$$

and all other definitions are as before. This wave-function is not normalized; the probability of obtaining a particular sequence of measurement outcomes is given by $\langle\Psi(t)|\Psi(t)\rangle$.

Because the real part of the displacement is proportional to $\langle x\rangle$ and the imaginary part is proportional to $\langle p\rangle$, we have a very clear picture of the physics arising in this situation. The membrane's initial displacement oscillates back and forth semi-classically. However, each time the BEC's spin is measured, the membrane's wave function splits into three distinct components, each having received a different kick from its interaction with the different possible spin orientations of the BEC. This indicates that the membrane is indeed put into a cat state, except for the fact that the kick is proportional to A, which is typicallysomewhat less than the ordinary zero point oscillations x_{zp}. If, going forward, we can increase A in an experimentally realizable setting, this system may provide an excellent demonstration of a macroscopic object put into a highly non-classical state.

B.5.2 Wigner function

Following a sequence of measurements, the Wigner function of the initially coherent state of the membrane motion becomes

$$\begin{aligned} W(x,p) &= \frac{1}{\pi\hbar\langle\Psi(t)|\Psi(t)\rangle}\sum_{\gamma,\alpha_1,\ldots,\beta_n} M^{(n)}_{\gamma\ \alpha_n} M^{(n-1)}_{\alpha_n\alpha_{n-1}}\ldots M^{(1)}_{\alpha_2\alpha_1}\rho_{\alpha_1\beta_1} M^{(1)\dagger}_{\beta_1\beta_2}\ldots M^{(n-1)\dagger}_{\beta_{n-1}\beta_n} M^{(n)\dagger}_{\beta_n\gamma} \\ &\times \exp\left(-i\sum_{i=1}^{n} t_i(\Omega_{L0}(\alpha_i-\beta_i)-\delta\Omega_L(\alpha_i^2-\beta_i^2))\right) \\ &\times \exp\Big[-\frac{m\omega_m}{\hbar}\Big\{(x-x_{zp}(a[\alpha]+a[\beta]+i(b[\alpha]-b[\beta])))^2 \\ &+ \left(\frac{p}{m\omega_m}-x_{zp}(b[\alpha]+b[\beta]-i(a[\alpha]-a[\beta]))\right)^2\Big\}+i(a[\beta]b[\alpha]-a[\alpha]b[\beta]) \\ &- i\frac{A}{2x_{zp}}(\Theta[\alpha]-\Theta[\beta])-\frac{1}{2}(a[\alpha]-a[\beta])^2-\frac{1}{2}(b[\alpha]-b[\beta])^2\Big] \end{aligned} \tag{B.36}$$

Figure B.4 shows the post-measurement Wigner function after successive measurements. The key point here is that repeated measurements can lead to very non-classical states, as is evident from the resulting negative valued Wigner functions. As can be seen in Eqs. (B.32) and (B.36), each measurement introduces different phase factors to the initial coherent state, along with splitting it into different coherent states. It is the quantum interference between the different coherent states thus generated that gives rise to the non-classical Wigner functions. Relatively few measurements are required to generate such non-classical states.

In fact, it is possible to turn a coherent state into a non-classical state after only one measurement. Fig. B.4 shows one such case. Here, $a_0 = b_0 = 1$ and the result of the first measurement after a time interval of $t_1 = \pi/\omega_m$ is $F_y = 0$. Repeated measurements after equal time intervals lead to states that resemble displaced fock states to states that can be thought of as Schrödinger cat states.

If the initial displacement is small in magnitude (as in Fig. B.4 below), this behavior will be rather independent of the measurement timing. For this particular case, with the outcome $F_y = 0$, it is seen for t_1 in the range $0.6\pi/\omega_m - 1.8\pi/\omega_m$. On

the other hand if the initial displacement is large (for example, $a_0 = 50\sqrt{2}$,$b_0 = 0$), the effect is much harder to find, as it becomes very sensitive to the timing of the measurements – only from $t_1 \approx 0.77\pi/\omega_m - 0.79\pi/\omega_m$. Nevertheless, in either case, successive measurements can build up some very interesting non-classical states. It may be possible to obtain a high degree of probabilistic quantum state control of the membrane if the dissipative effects do not wash out the interference too quickly.

B.6 Conclusion

In conclusion, we have demonstrated that by coupling a magnetic membrane to a BEC, we can indirectly monitor the position of the membrane. This measurement induces significant back-action that can be measured for reasonable experimental parameters. We investigated the effect of this interaction for different initial membrane states, namely thermal and coherent states. We discussed the possibility to measure back-action of a quantum measurement on the membrane via repeated measurements and the potential to generate cat states of the oscillator via such repeated measurements in the case of an initial coherent state. A study of the effect of dissipation on this dynamics is the subject of future work. Future work will also include developing a theory for a general coupling to other spin components i.e. an interaction Hamiltonian of the form $F.r$, because at short distances the coupling to other spin components cannot be ignored. also, dissipation, and multiple modes of the membrane.

Acknowledgments – We thank David Brown for his help during the initial stages of these calculations. This work is supported by the US National Science Foundation, the DARPA ORCHID and QUASAR program, the US Army Research Office, and US Office of Naval Research. MET is supported by TUBITAK, The Scientific and Technological Research Council of Turkey.

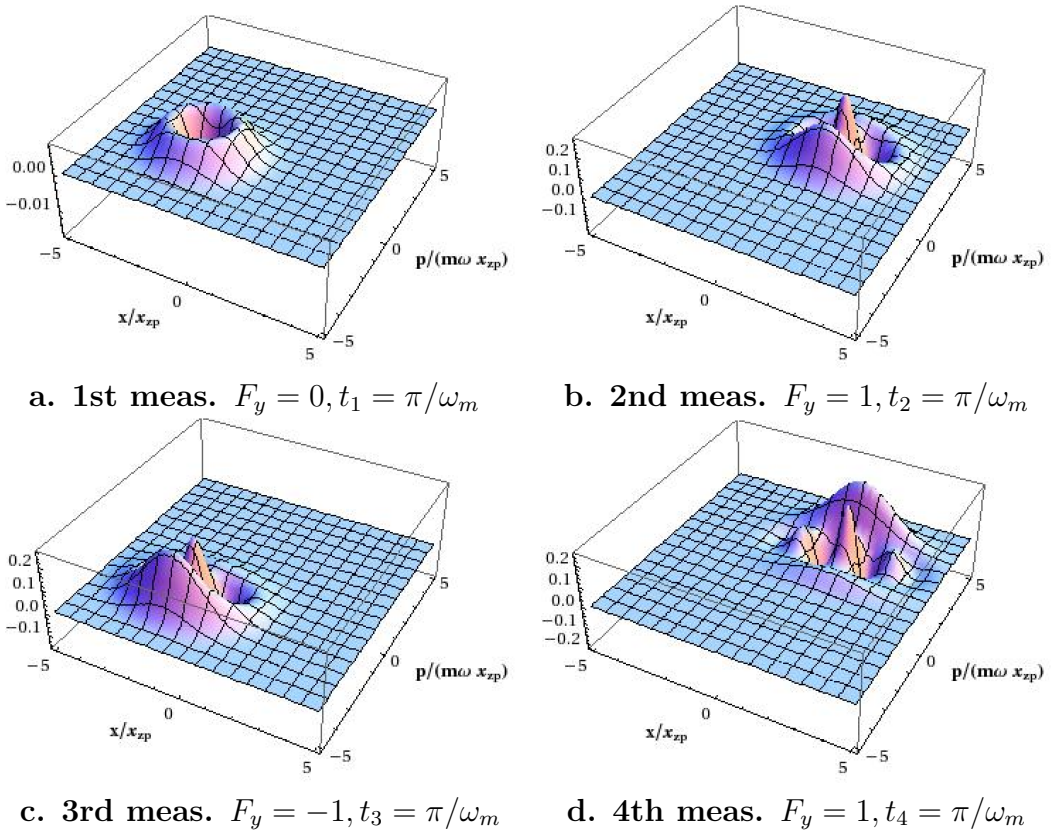

a. 1st meas. $F_y = 0, t_1 = \pi/\omega_m$ **b. 2nd meas.** $F_y = 1, t_2 = \pi/\omega_m$

c. 3rd meas. $F_y = -1, t_3 = \pi/\omega_m$ **d. 4th meas.** $F_y = 1, t_4 = \pi/\omega_m$

Figure B.4: Post-measurement Wigner distribution functions of the membrane, initially in a coherent state $\alpha = 1 + i1$. We notice that repeated measurements do indead lead to some interesting non-classical states. The measurement results and evolution time before measurement are given for each plot.

B.7 Mathematical Appendices

B.7.1 Derivation of interaction Hamiltonian

Our starting assumption is that the magnetic domain on the membrane is a point dipole located at the origin. The magnetic field due to that dipole is

$$\mathbf{B}(\mathbf{r}) = \frac{\mu_0}{4\pi}\frac{1}{r^3}\left(3(\mu_{\mathbf{m}}.\hat{\mathbf{r}})\hat{\mathbf{r}} - \mu_{\mathbf{m}}\right) \tag{B.37}$$

It is the small inhomogeneity of the resulting magnetic field along the long axis z of the condensate, and the resulting variation in Larmor precession frequency, that permits to characterize the center-of-mass mode of oscillation of the membrane.

For a dipole polarized along the z-axis ($\mu_{\mathbf{m}} = \mu_m\hat{\mathbf{z}}$), and distance $r = (x^2 + y^2 + z^2)^{1/2}$, the components of the magnetic field (B.37) are

$$B_x(x,y,z) = \frac{\mu_0}{4\pi}\frac{\mu_m}{r^3}\left[\frac{3xz}{r^2}\right] \tag{B.38}$$

$$B_y(x,y,z) = \frac{\mu_0}{4\pi}\frac{\mu_m}{r^3}\left[\frac{3yz}{r^2}\right] \tag{B.39}$$

$$B_z(x,y,z) = \frac{\mu_0}{4\pi}\frac{\mu_m}{r^3}\left[\frac{3z^2}{r^2} - 1\right] \tag{B.40}$$

With $x = x_0 + x_m$, where x_0 is the equilibrium value of x for a condensate atom, $x = 0$ is the equilibrium position of the membrane, and x_m its small sinusoidal displacement of the membrane around the origin. Expanding the expression for magnetic fields for small x_m (up to first order) we get

$$B_x \approx \frac{\mu_0\mu_m}{4\pi r_0^5}\left[3x_0 z - \frac{3z(4x_0^2 - y^2 - z^2)}{r_0^2}x_m\right] \tag{B.41}$$

$$B_y \approx \frac{\mu_0\mu_m}{4\pi r_0^5}\left[3yz - \frac{15x_0 yz}{r_0^2}x_m\right] \tag{B.42}$$

$$B_z \approx \frac{\mu_0\mu_m}{4\pi r_0^5}\left[(2z^2 - x_0^2 - y^2) + \frac{3x_0(x_0^2 + y^2 - 4z^2)}{r_0^2}x_m\right] \tag{B.43}$$

here, $r_0 = (x_0^2 + y^2 + z^2)^{1/2}$. Assuming a two-dimensional condensate (i.e. $y \approx 0$), we can set $B_y \to 0$. For theoretical simplicity, we assume that the measurements are made on the part of the condensate directly above the magnet, i.e. close to $z = 0$. Under these approximations, the magnetic field simplifies to just being in the z-direction,

$$B_z \approx \frac{\mu_0 \mu_m}{4\pi x_0^4} \left[-x_0 + 3x_m\right]. \tag{B.44}$$

Combining this with the quantization field B_0, we end up with the interaction Hamiltonian of the form

$$V = \mu_B g_F F_z \left[B_0 - \frac{\mu_0 \mu_m}{4\pi x_0^3} + \frac{3\mu_0 \mu_m}{4\pi x_0^4} x_m\right]. \tag{B.45}$$

We can break this total magnetic field into a constant part, B_c (sum of the first two terms), and a component that varies at the membrane frequency, $B_v' x_m$. Here, the gradient of the magnetic field,

$$B_v' = \frac{3\mu_0 \mu_m}{4\pi x_0^4}. \tag{B.46}$$

This is the form used in Equation (B.4).

B.7.2 Derivation of Successive Measurement Density Matrix

Here we outline the steps used in section IV to derive (B.22). We arrive at the result via induction. Suppose that $n-1$ measurements have been performed already. We denote the density matrix at this moment by $\rho^{(n-1)}$. After the next period of free evolution and the nth measurement, we have

$$\rho^{(n)} = M^{(n)} U(t_n) \rho^{(n-1)} U^\dagger(t_n) M^{(n)}. \tag{B.47}$$

To find the matrix elements, we insert completeness relationships:

$$\begin{aligned} \langle \alpha, x_f | \rho^{(n)} | \beta, x_i \rangle &= \sum_{\alpha_n} \sum_{\beta_n} \int dx \int dy \langle \alpha, x_f | M^{(n)} U(t_n) | \alpha_n, x \rangle \\ &\times \langle \alpha_n, x | \rho^{(n-1)} | \beta_n, y \rangle \langle \beta_n, y | U^\dagger(t_n) M^{(n)} | \beta, x_f \rangle. \end{aligned} \tag{B.48}$$

Now, the propagator can be derived from (B.11) by multiplying by the trace, substituting $\eta \to i\omega_m t/2$, and including the contributions of the F_z-dependent parts of the Hamiltonian. Using these techniques, we arrive at the needed matrix elements:

$$\begin{aligned}\langle \sigma, u|M^{(n)}U(t_n)|\tau, v\rangle &= M^{(n)}_{\sigma\ \tau}\sqrt{\frac{8m\omega_m}{i\pi\hbar\sin\omega_m t}}\exp\Big[-i\Big[t_n\Omega_{L0}\tau - t_n\delta\Omega\tau^2 \\ &+ \frac{m\omega}{4\hbar}\left((u+v+2A\tau)^2\tan\frac{\omega_m t_n}{2} - (u-v)^2\cot\frac{\omega_m t_n}{2}\right)\Big]\Big] \quad \text{(B.49)}\end{aligned}$$

The fact that (B.11) and the individual terms of (B.13) (i.e. terms of the form in (B.12) do not differ except for shifts in the coordinates and some complex phase shifts leads us to conjecture that additional evolution and measurements will not alter the underlying structure of the density matrix. Thus, we try a matrix of the form (B.22) for $\rho^{(n-1)}$, but with unknowns for $X^{(n-1)}$, etc. (superscript added for clarity) and see if evaluation of the integral (B.48) produces a similar output for $\rho^{(n)}$. Indeed it does, and it also gives us the recurrence relations used to derive (B.24-B.26). These are

$$\begin{aligned}X^{(n)}[\sigma] &= X^{(n-1)}[\sigma]\cos\omega_m t_n + P^{(n-1)}[\sigma]\sin\omega_m t_n + \sigma_n(1-\cos\omega_m t_n), \quad \text{(B.50)} \\ P^{(n)}[\sigma] &= P^{(n-1)}[\sigma]\cos\omega_m t_n - X^{(n-1)}[\sigma]\sin\omega_m t_n + \sigma_n\sin\omega_m t_n, \quad \text{(B.51)} \\ \phi^{(n)}[\sigma] &= \phi^{(n-1)}[\sigma] + (X^{(n)}[\sigma]^2 + X^{(n-1)}[\sigma]^2)\cot\omega_m t_n \\ &- 2X^{(n)}[\sigma]X^{(n-1)}[\sigma]\csc\omega_m t_n. \quad \text{(B.52)}\end{aligned}$$

The solutions to these recurrence relationships are the equations given above.

B.7.3 Derivation of Coherent State Evolution

We again will arrive at the result (B.32) by using induction and finding a set of recurrence relations as in Appendix B, but the steps involved are slightly different. We first split the Hamiltonian (B.8) into two parts $\tilde{H}_{\rm BEC}$ and $(\tilde{H}_m + \tilde{V})$. These commute, so the unitary evolution operator can simply be factorized into two operators, one acting only on the BEC and another acting as a shifted harmonic oscillator. We

also note that the unperturbed membrane Hamiltonian and $\tilde{H}_m + \tilde{V}$ are related by a simple unitary transformation, namely

$$\tilde{H}_m + \tilde{V} = D\left(-\frac{A}{2x_{zp}}F_z\right) H_m D\left(\frac{A}{2x_{zp}}F_z\right). \tag{B.53}$$

Using this fact and the well-known results

$$\exp[-iH_m t/\hbar]D(\zeta) = D(e^{-i\omega_m t}\zeta)\exp[-iH_m t/\hbar], \tag{B.54}$$

$$D(\zeta)D(\xi) = D(\zeta+\xi)e^{(\zeta\xi^* - \zeta^*\xi)/2}, \tag{B.55}$$

we can postulate that the system after $n-1$ measurements is specified by a superposition of states as in (B.32), apply an additional evolution and measurement,

$$|\Psi^{(n)}\rangle = M^{(n)}\tilde{U}_{\rm BEC}(t_n)\tilde{U}_m(t_n)|\Psi^{(n-1)}\rangle, \tag{B.56}$$

and then use the result to find the following recurrences:

$$a^{(n)}[\sigma] = a^{(n-1)}[\sigma]\cos\omega_m t_n + b^{(n-1)}[\sigma]\sin\omega_m t_n - \frac{\sigma_n A}{2x_{zp}}(1-\cos\omega_m t_n), \tag{B.57}$$

$$b^{(n)}[\sigma] = b^{(n-1)}[\sigma]\cos\omega_m t_n - a^{(n-1)}[\sigma]\sin\omega_m t_n - \frac{\sigma_n A}{2x_{zp}}\sin\omega_m t_n, \tag{B.58}$$

$$\Theta^{(n)} = \Theta^{(n-1)} + \alpha_n(b^{(n-1)} - b^{(n)}). \tag{B.59}$$

Note the strong resemblance between the first two of these equations and those from the previous appendix. This is to be expected, as the real and imaginary parts of the displacement are proportional to the expected position and momentum of the coherent state, respectively. The solutions to these equations are (B.33-B.35).

B.7.4 Simulation of measurement backaction

We outline here the utilitarian approach used to produce Kraus operators $M^{(i)}$ more appropriate to the dispersive phase contrast measurement, rather than using projectors onto F_y eigenstates. Since the spinor BEC has a coherence time of order nearly 1s, we assume that the measurement will leave the atoms in the condensate all

in the same spin state. We note the relationship B.60 below gives partial information about the average spin wavefunction of the condensate. Therefore, given a measured phase difference s we sum over projectors onto all states consistent with that value s and normalize to attain the $M^{(i)}$ for that particular measurement. Because the signal depends on the expactation values of F_y and F_y^2, we average the results of such a procedure over all atoms in the condensate and then apply a cumulative operator to the spin portion of the density matrix. Preliminary results using such a procedure are encouraging.

B.7.5 Experimental Implementation

Here, we provide details on the experimental detection of the quantum backaction on the micromechanical membrane. The membrane is composed of Silicon Nitride with a micron-scale magnetic domain deposited at its center. These structures are fabricated by coating silicon wafers with around 100 nm of high stress silicon nitride and then etching the silicon in a 50 μm $\times$ 50 μm region to reveal a free standing membrane.Quality factors exceeding 10^6 have been demonstrated with similar SiN membranes for resonance frequencies in the range of 500 kHz [16]. The magnetic domain is deposited on this membrane by a combination of photolithography and sputtering of a high permeability material like permalloy [15]. Peak surface fields on the order of 1 T at the surface of this magnetic domain should ensure field gradients around 10^3 T/m in the regions above the domain. The membrane is supported on a cryogenically cooled flange housed in a UHV chamber. Sputtered gold films deposited on the substrate in the regions surrounding the membrane serve as mirrors for trapping and imaging. Spinor Bose condensates of ^{87}Rb in the $F = 1$ hyperfine state will be optically confined about 5 μm above the membrane in a quasi-2D trap created by shallow angle interference of laser beams reflected off the gold surface [17]. This ensures a quasi-2D confinement of the condensates such that the spatial extent of the gas in the direction normal to the membrane is less than

the spin healing length $\xi = \sqrt{\hbar/2m|c_2 n|}$. Here, $c_2 = 4\pi\hbar^2(a_2 - a_0)/m$ is the spin dependent coupling strength of the spinor gas and $a_0(a_2)$ is the s-wave scattering length in the $F = 0(F = 2)$ channel. In this way, we can freeze out spin dynamics along this dimension [10].

The estimation of the membrane's position is based on detecting the Zeeman shift at the location of the condensate due to the micromotion of the membrane. This is achieved by magnetization-sensitive phase contrast imaging as demonstrated in [10]. To summarize this technique briefly, a sequence of non-destructive phase contrast images of the condensate are obtained with far off-resonant circular polarized light. Due to Larmor precession of the gas, the phase imprinted on the probe light is modulated at the Larmor frequency leading to a phase contrast signal given by

$$s = 1 + 2\tilde{n}\sigma_0(\gamma/2\Delta)[a_0 + a_1\langle F_y\rangle + a_2\langle F_y^2\rangle] \tag{B.60}$$

where $\tilde{n}$ is the column density of the gas, $\sigma_0 = 3\lambda^2/2\pi$ is the resonant cross section, Δ is the detuning of the probe light from resonance and γ is the natural linewidth. F_y is the projection of the local atomic spin along the imaging axis. The constants a_0, a_1 and a_2 depend on the detuning of the probe light and describe the isotropic polarization and optical activity of the condensate. By analyzing the sequence of phase contrast images on a pixel-by-pixel basis, we can estimate the local Larmor precession rate and hence, the local magnetic field. At the shot noise limit, we estimate a magnetic field sensitivity on the order of 15 fT/Hz$^{1/2}$ for a condensate of area 50 μm^2 in the plane of the membrane [18]. For the expected field gradient of 10^3 T/m at the location of the condensate, this field sensitivity translates to a position sensitivity of 15×10^{-18} m/Hz$^{1/2}$. This is much smaller than the zero point motion of the oscillator which has an amplitude on the order of 6×10^{-15} m.

REFERENCES

[1] V. B. Braginsky and F Ya. Khalili, "Quantum Measurement", Cambridge University Press (1992).

[2] T.J. Kippenberg and K.J. Vahala, Science **321**, 1172 (2008). F. Marquardt and S. M. Girvin, Physics **2**, 40 (2009).

[3] Ying-Ju Wang *et. al*, Phys. Rev. Lett. **97**, 227602 (2006).

[4] D. Hunger *et. al*, Phys. Rev. Lett. **104**, 143002 (2010).

[5] P. Treutlein *et. al*, Phys. Rev. Lett. **99**, 140403 (2007).

[6] C. Genes, D. Vitali and P. Tombesi, Phys. Rev. A **77**, 050307(R) (2008).

[7] K. Hammerer *et. al*, Phys. Rev. Lett. **103**, 063005 (2009).

[8] S. Singh and P. Meystre, Phys. Rev. A **81**, 041804(R) (2010).

[9] K. Hammerer *et. al*,Phys. Rev. A, **82**, 021803(R) (2010).

[10] M. Vengalatorre *et. al*, Phys. Rev. Lett. **98**, 200801 (2007).

[11] J. M. Obrecht *et. al*, Phys. Rev. Lett. **98**, 063201 (2007).

[12] T. van Zoest *et. al*, Science **328**, 1540 (2010)

[13] J. M. Higbie *et. al*, Phys. Rev. Lett. **95**, 050401 (2005).

[14] K. W. Murch *et. al*, Nature Physics **4**, 561 (2008)

[15] M. Vengalattore *et al*, J. Appl. Phys. **95**, 4404 (2004).

[16] B. M. Zwickl *et al*, Appl. Phys. Lett. **92**, 103125 (2008).

[17] D. Gallego *et al*, Opt. Lett. **34**, 3463 (2009).

[18] M. Vengalattore *et al*, (to be published).

APPENDIX C

QUANTUM COLLECTIVE QCD STRING DYNAMICS

S. Steinke and J. Rafelski

Published in Journal of Physics G, **32**, S455

ABSTRACT

The string breaking model of particle production is extended in order to help explain the transverse momentum distribution in elementary collisions. Inspired by an idea of Bialas, we treat the string using a collective coordinate approach. This leads to a chromo-electric field strength which fluctuates, and in turn implies that quarks are produced according to a thermal distribution.

C.1 Introduction

We study the production process of hadronic particles in elementary collisions based on the string breaking mechanism of QCD. The non-Abelian SU(3)-color gauge group leads to confinement of the color electromagnetic field lines at scales of roughly 1 fm and above. Thus, a $q\bar{q}$ pair produced in, say, an e^+e^- collision will have a chromo-electric flux tube connecting the quark and antiquark. The tube increases in length as the quarks separate, and eventually there is sufficient energy in the field to produce another $q\bar{q}$ pair. The rate of production is calculated via Schwinger's

formula [1], generalized to consider transverse particle momentum [2]. This is often referred to as the string breaking mechanism of particle production.

Despite its successes, one troublesome detail of the QCD-string model has not been fully explained. The predicted transverse momentum distribution of quarks is Gaussian [2], while the observed spectrum of final state particles is thermal, or very nearly so [3, 4, 5, 6]. Naïve averaging over constituent quark transverse momenta cannot make an exponential distribution out of a Gaussian one. Further, it is not natural to suppose that there is sufficient rescattering for thermalization in systems as small as those in e^+e^- and $p\bar{p}$ collisions. Hagedorn thus spoke before QCD was developed of 'pre-established thermal equilibrium' [3]. While the string model itself has been refined several times, nothing like a thermal $p_\perp$ spectrum has been predicted by any of these refinements until recently.

This discrepancy invites new ideas. Bialas showed that a random fluctuation of the string tension could produce particles in a thermal spectrum [7], if the appropriate initial distribution is used. He proposed that these fluctuations originate from the stochastic nature of the QCD vacuum. There has been further work on an extensions of this idea using dynamical fluctuations of the string in time [8]. This method seems like a promising way to proceed, and the purpose of this paper is to improve the justification for these fluctuations, as well as to propose a possible origin.

We separate the transverse and longitudinal dynamics of the string, introduce collective coordinates for the transverse dynamics of the string and quantize them. The reason that we will proceed this way is the following order of magnitude consideration: due to the very high momentum in the longitudinal direction (constituent quarks may have $p_L \approx 100 GeV$ or more, in a 1 TeV $p\bar{p}$ collision) it is reasonable to treat this part of the dynamics classically. However, the typical transverse momentum of a produced $q\bar{q}$ pair will be on the order of the temperature (which we are seeking to justify) $T \simeq 160\,\mathrm{MeV}$. The radius of the string is about $1\,\mathrm{fm}$, approxi-

mately the same magnitude as the DeBroglie wavelength of the produced particles.

Our approach is inspired by prior collective coordinate approaches in many-body quantum systems. One well-known example is the excitation spectrum of vibrations and rotations of large nuclei[9]. In the simplest liquid drop version of this model, Coulomb repulsion competes with nuclear surface tension. Quantization of the Hamiltonian resulting from these interactions leads to an excitation spectrum which can be verified experimentally.

In the string model, we once again have two competing energy considerations. The field lines will tend to spread in order to minimize their energy content. However, the vacuum confines color; this effect can be effectively reproduced by implementing in transverse direction the bag pressure and energy density dynamics. One might ask where the many-body quality arises in the string picture, since there is just a single $q\bar{q}$ pair anchoring the ends of the string. The answer is in the large number of virtual gluons which constitute the string QCD fields. We consider the string to be a collective excitation of this gluon sea.

In section C.2, we first look at the classical string picture, namely the energy balance and the Hamiltonian that results. Quantizing this Hamiltonian yields a harmonic oscillator-type wave equation for the transverse dimension of the string. We explore some of the properties of the solutions to this equation. Then, in section C.3, we fold the resulting probability distribution for the string tension with the Schwinger formula for pair production [1, 2]. This in fact generates an exponential $p_\perp$ spectrum.

C.2 Wave Equation

C.2.1 String Hamiltonian

In preparation for quantization, we will first write down a Hamiltonian, focusing here on the energy density per unit length. We combine the contributions to the

energy density from the chromo-electric field and the vacuum pressure to obtain the classical Hamiltonian density

$$\sigma = \tfrac{1}{2}E_L^2 A + BA. \tag{C.1}$$

The two terms are reminiscent of the usual kinetic and potential energies. Since the chromo-electric field is longitudinal, we will denote it by E_L to avoid confusion with energy.

Suppose the field lines are broken by a $q\bar{q}$ pair produced, each having color charge g. In the case where the field is longitudinal, we may simplify the non-Abelian Gauss' law down to its usual form:

$$\int \sum_a \vec{E}_a \lambda_a \cdot d\vec{A} = \tfrac{1}{2}g. \tag{C.2}$$

The factor $\frac{1}{2}$ arises comparing the elementary currents in QCD and QED:

$$j_a^\mu \equiv \frac{g}{2}\bar{\Psi}\gamma^\mu \lambda_a \Psi, \qquad j^\mu \equiv e\bar{\psi}\gamma^\mu\psi. \tag{C.3}$$

Note that we have taken E_L to be constant here. This is easily justified: under the constraint of a fixed flux, the total energy is minimized by a uniform field. Due to the presence of the constraint equation (C.2), one eliminates the dependence on, say, E_L, and obtains:

$$\sigma = \tfrac{g^2}{8A} + BA. \tag{C.4}$$

We can see the interplay between field and vacuum energy more clearly now. Minimizing σ with respect to A gives

$$A^{\text{classical}} = \tfrac{g}{2\sqrt{2B}}, \tag{C.5}$$

$$E_L^{\text{classical}} = \sqrt{2B}, \tag{C.6}$$

and thus a classical string tension of:

$$\sigma = \tfrac{g}{2}\sqrt{2B} = \tfrac{g}{2}E_L^{\text{classical}}. \tag{C.7}$$

C.2.2 Position-momentum collective dynamics

The string arises as a quasi particle state (presumably) in the full theory of QCD. Thus, its dynamics must be treated in an appropriate quantized way. However, as we noted earlier, the longitudinal evolution of the string should be safe to approximate classically, at least in our initial crude treatment. Furthermore, we assume the string is rigid. To be precise, there is no spatial bending of the string, nor spatial dependence in the field strength.

There are two reasons that we make this assumption. First, though the energy may fluctuate between bag and field energy, we suppose that the configuration of either is such that their separate energy contents are minimized. Second, treating the complexities of a "wavy" string is well beyond the scope of this paper. The chromo-electric field now contains only 1 degree of freedom, the longitudinal strength. Therefore, its conjugate coordinate, which will be the string cross section area or something related, will retain only 1 degree of freedom. Thus, it appears that the initially 2-dimensional transverse dynamics may in fact be successfully modeled by a 1-dimensional wave equation. Despite the simplifications, it will still be a problem with a constraint, equation (C.2) (Gauss' law), and an unusual looking Hamiltonian.

To deal with the transverse dynamics as a quantum problem in an expedient manner, we make the following further simplification. As is evident the problem arising should still be closely related to the original one, though, admittedly, there is no absolute guarantee of complete isomorphic relation. We take the constraint equation (C.2) and substitute it just once into the Hamiltonian, equation (C.1), yielding:

$$H_\sigma = \tfrac{1}{4} g E_L + BA. \tag{C.8}$$

We want to quantize this Hamiltonian in terms of Hermitian operators with the usual dimensions of distance and momentum. Since our degrees of freedom are A

and E_L, which dimensions are square of distance and momentum, we introduce

$$x = \sqrt{A} \tag{C.9}$$

$$p = \sqrt{\tfrac{g}{2} E_L}. \tag{C.10}$$

Here we have defined p to be the root of the classical energy density. Since the square root may take on positive or negative values, we will allow $x, p \in (-\infty, +\infty)$. We make x and p into canonically conjugate operators, and so they satisfy the commutation relation

$$[x, p] = ig \tag{C.11}$$

The justification for our choice of commutator will follow. Indeed, H_σ now looks like the Hamiltonian of a harmonic oscillator:

$$H_\sigma = \tfrac{1}{2} p^2 + Bx^2. \tag{C.12}$$

Working in the p-representation leads to the wave equation:

$$\left(\tfrac{1}{2} p^2 - Bg^2 \tfrac{\partial^2}{\partial p^2} \right) \psi_n = \sigma_n \psi_n. \tag{C.13}$$

This is a very familiar equation, and its eigenvalues are:

$$\sigma_n = \sqrt{2Bg^2} \left(n + \tfrac{1}{2} \right). \tag{C.14}$$

Note that if the dimension of the problem is in fact not 1 but d, the $\frac{1}{2}$ would have to be multiplied by d, and there would be additional n's.

As a matter of convenience, let us define

$$T_0 \equiv \sqrt{\tfrac{\sigma_n}{2\pi(2n+1)}} \tag{C.15}$$

Then we may express the eigensolutions of the problem as

$$\psi_n(p) = \tfrac{A_n}{\sqrt{T_0}} \mathcal{H}_n(\sqrt{p^2/4\pi T_0^2}) e^{-p^2/8\pi T_0^2}, \tag{C.16}$$

where $\mathcal{H}_n$ are Hermite polynomials, and A_n is a dimensionless normalization.

C.2.3 Properties of the quantized string

Let us now take stock of some of the features that have become evident in our model. First of all, we may calculate the expected cross sectional area and field strength; because

$$\langle \tfrac{1}{2}p^2 \rangle = \langle Bx^2 \rangle = \tfrac{1}{2}\sigma_n \tag{C.17}$$

we obtain

$$\langle E_L \rangle = \tfrac{2\sigma_n}{g} = \sqrt{2B}(2n+1), \tag{C.18}$$

$$\langle A \rangle = \tfrac{\sigma_n}{2B} = \tfrac{g}{\sqrt{8B}}(2n+1). \tag{C.19}$$

In both cases there is agreement between the ground state and the classical picture.

Now, we want to see if the constraint, as well, is satisfied. It is reasonable to look at the product of the expectation values and see if Gauss' Law results.

$$\langle E_L \rangle \langle A \rangle = \tfrac{g}{2}(2n+1)^2 \tag{C.20}$$

By using this combination of operators we see that the ground state at least satisfies (C.2). This also clarifies our choice of commutator in equation (C.11). Whether or not this excludes excited states of the string remains to be seen. For if we consider different combinations of expectation values that still appear to be related to the constraint, we attain different results. Consider, for example,

$$\langle xp \rangle \langle px \rangle = \tfrac{g}{2}. \tag{C.21}$$

This should be related to the constraint, and it indicates that all excited string states may satisfy equation (C.2). Finding the correct combination of operators to verify if the constraint equation (C.2) is satisfied remains a difficult problem. However, these preliminary results strongly suggest that at least one, if not more, string states are admissible solutions.

C.3 Thermal $p_\perp$ Spectrum

We are now ready to investigate the spectrum of particles produced from this string. First, let us look at the probability distribution $P(E_L)$. Taking the probability density ψ_n^2 and changing coordinates back to the field strength, we obtain

$$dP_n(E_L) = \frac{B_n}{T_0\sqrt{gE_L}}\mathcal{H}_n^2(\sqrt{gE_L/8\pi T_0^2})e^{-gE_L/8\pi T_0^2}dE_L. \tag{C.22}$$

B_n is again a dimensionless normalization. Note that the factor $(gE_L)^{-1/2}$ arises from the change in measure. The singularity arising for even n is not troubling; it is an artifact of the change in measure and never worse than $E_L^{-1/2}$.

Next, we review the traditional particle production spectrum. The probability per unit 4-volume of a quark pair of momentum $p_\perp$ being produced is given by the Schwinger mechanism, as expounded by Casher, Neuberger and Nussinov[2]:

$$dP(p_\perp) = \frac{gE_L}{8\pi^3}e^{-2\pi m_\perp^2/gE_L}d^2p_\perp. \tag{C.23}$$

This is in fact only the first term in an infinite sum, but the approximation is appropriate for our current level of precision. We consider each string breaking to be, essentially, a measurement of E_L. For now, let us suppose that the strings are formed in the ground state, with string tension σ_0. Thus, over several string breakings, the observed spectrum of produced quarks is obtained by folding equations (C.22) and (C.23) over E_L.

Performing this folding results in the quark transverse production probability per unit 4-volume,

$$dP_{\text{quark}}(p_\perp) = \frac{CT_0^2}{g}(1 + m_\perp/T_0)e^{-m_\perp/T_0}d^2p_\perp. \tag{C.24}$$

This agrees with previous results up to a linear prefactor[7, 8]. As a final step, consider the composite hadron spectrum. We will obtain this by first rewriting the distribution in terms of the transverse mass (fortunately, it is already more or less in

such a form), and then folding two distributions together, corresponding to quark-antiquark or quark-diquark pairings. The final hadron spectrum thus obtained is

$$\frac{dP_{\rm hadrons}(m_\perp)}{dm_\perp} \propto \left(2X_3 - \frac{6}{5}X_5 + X_\perp\left(-3X_2 + 2X_3 + 3X_4\right)\right.$$
$$\left. -X_\perp^2\left(3X_2 + 2X_3\right) + X_\perp^3 + X_\perp^4 + \frac{1}{5}X_\perp^5\right) e^{-X_\perp} \quad \text{(C.25)}$$

where

$$X_n \equiv \left(\frac{m_1}{T_0}\right)^n + \left(\frac{m_2}{T_0}\right)^n, \qquad X_\perp \equiv \frac{m_\perp}{T_0}$$

and m_1 and m_2 are the constituent quark/diquark/antiquark masses. Note that the largest root of the prefactor is $m_\perp = m_1 + m_2$, and thus the probability is always positive, as expected. This can be seen trivially in the case $m_1 = m_2 = 0$. The specific relationship (C.15) is the same as in the aforementioned works, though the pre-factor shifts slightly the fitted temperature. Making use of a fairly standard value for the string constant, $\sigma_0 \approx 0.9$ GeV/fm, gives $T_0 \approx 165$ MeV.

C.4 Conclusions

We have considered the string between a $q\bar{q}$ pair as a quasiparticle excitation of the gluon field. Thus, we justified introducing collective quantization of transverse dynamics. This implies that the internal chromo-electric field is not constant, but rather when the string breaks and the field is observed, it takes on values according to a quantum probability distribution. Folding this distribution with the traditional Schwinger-Casher-Neuberger-Nussinov result leads to an intrinsically thermal $p_\perp$ spectrum. The emerging phenomenology is quite satisfactory; e.g. it produces a thermal spectrum. However, a more complete theory will certainly lead to further insights including refinement of the temperature parameter.

Acknowledgments Work supported by a grant from: the U.S. Department of Energy DE-FG02-04ER41318. SKS thanks SQM2006 for local support.

REFERENCES

[1] J. S. Schwinger, Phys. Rev. **82**, 664 (1951)

[2] A. Casher, H. Neuberger, S. Nussinov *Phys. Rev. D* 20 179 (1979)

[3] R. Hagedorn and J. Ranft, Nuovo Cim. Suppl. **6**, 169 (1968)

[4] R. Hagedorn, Nuovo Cim. Suppl. **3**, 147 (1965)

[5] H. Grote, R. Hagedorn and J. Ranft, "Atlas of Particle Production Spectra", CERN-Black Book Report 1970.

[6] F. Becattini [hep-ph/9701275] (1997), "Universality of thermal hadron production in pp, $p\bar{p}$ and e^+e^- collisions" in'Proceedings of the XXXIII Eloisatron Workshop "Universality features in Multihadron production and the leading effect", October 19-25 1996, Erice (Italy) Report-no: DFF 263/12/1996.

[7] A. Bialas *Phys. Let. B* 466 301 (1999)

[8] W. Florkowski *Acta Phys. Pol. B* 35 799 (2004), and presentation to be published in proceedings of 46th Cracow School of Theoretical Physics (2006)

[9] see e.g. A.E.S. Green in *Nuclear Physics*, McGraw-Hill, New York (1955)